THE HONG KONG
POLYTECHNIC UNIVERSITY
香港理工大學
Pao Yue-kong Library
包玉剛圖書館

Copyright Undertaking

This thesis is protected by copyright, with all rights reserved.

By reading and using the thesis, the reader understands and agrees to the following terms:

1. The reader will abide by the rules and legal ordinances governing copyright regarding the use of the thesis.
2. The reader will use the thesis for the purpose of research or private study only and not for distribution or further reproduction or any other purpose.
3. The reader agrees to indemnify and hold the University harmless from and against any loss, damage, cost, liability or expenses arising from copyright infringement or unauthorized usage.

IMPORTANT

If you have reasons to believe that any materials in this thesis are deemed not suitable to be distributed in this form, or a copyright owner having difficulty with the material being included in our database, please contact lbsys@polyu.edu.hk providing details. The Library will look into your claim and consider taking remedial action upon receipt of the written requests.

Pao Yue-kong Library, The Hong Kong Polytechnic University, Hung Hom, Kowloon, Hong Kong

http://www.lib.polyu.edu.hk

QUALITY OF TRANSMISSION ESTIMATION AND PARAMETER MONITORING TECHNIQUES FOR NEXT-GENERATION OPTICAL NETWORKS

LU JIANING

PhD

The Hong Kong Polytechnic University

2021

The Hong Kong Polytechnic University

Department of Electronic and Information Engineering

Quality of Transmission Estimation and Parameter Monitoring Techniques for Next-Generation Optical Networks

Lu Jianing

A thesis submitted in partial fulfillment of the requirements for

the degree of Doctor of Philosophy

May 2021

CERTIFICATE OF ORIGINALITY

I hereby declare that this thesis is my own work and that, to the best of my knowledge and belief, it reproduces no material previously published or written, nor material that has been accepted for the award of any other degree or diploma, except where due acknowledgement has been made in the text.

… ……. (Signed)

……LU JIANING ……. (Name of student)

ABSTRACT

Fiber optical communication system is an essential component of our information society. Ever emerging applications and services have provided strong motivations for ultra-long transmission distance and ultra-high transmission capacity for the communication systems. As a result, high-spectral efficiency (SE) coherent fiber optical transmission together with powerful digital signal processing (DSP) technique has become the dominant technical approach by which the received signal can be efficiently processed in the digital domain. To further improve the utilization of the available system capacity, dynamic optical networking should be implemented. This requires accurate, efficient, and low-cost optical performance monitoring (OPM) techniques. One of the key functions of OPM is optical signal-to-noise ratio (OSNR) monitoring. Conventional OPM modules for OSNR monitoring assume the signal is only affected by amplified spontaneous emission (ASE) noise. However, high-speed optical signals suffer more severe impairments with the growing transmission distance and capacity. In particular, fiber nonlinearity becomes non-negligible, and conventional OPM methods must be improved to consider the effect of fiber nonlinearity. Moreover, in flexible optical networks, the optical parameters and impairments resulted from fast-varying and heterogeneous transmission links put forward more stringent requirements on the multi-functionality and affordable complexity of OPM modules. On the other hand, since next-generation optical networks are expected to be highly flexible elastic optical networks (EONs), it is

desirable for them to make full use of physical-layer and time resources to maximize network capacity. Key enablers for maximizing the capacity of EONs are dynamic lightpath provisioning, baud rate, modulation format, and shaping factor adaptation based on quality of transmission (QoT) estimation by which the SNR of each channel is predicted. Due to the lack of an efficient and reliable QoT estimator, current optical networks incorporate large operating margins, including unallocated, system, and design margins, in order to ensure that the planned demand capacity as well as the service level agreements (SLAs) are met. This results in network over-dimensioning for both green-field and brown-field scenarios. Therefore, accurate QoT estimation is the key enabler for low-margin optical networking. However, in wavelength-division-multiplexed (WDM) and heterogenous dynamic link environments, the parameter uncertainties and fiber nonlinear distortions render QoT estimations a nontrivial task: the SNR estimation of one channel depends not only on the linear accumulation of ASE noise from inline Erbium-doped fiber amplifiers (EDFAs), but also on the signal power and lightpath of all channels in a complicated manner, and all the parameters are subject to a certain level of uncertainty. How to implement a practical and accurate QoT estimator is a significant research challenge.

In view of the above key problems in next-generation optical transmission systems and networks, this thesis will focus on advanced multi-parameter monitoring techniques including the monitoring strategies of modulation format, timing and frequency offset (TO and FO), FO drift (FOD), linear noise and nonlinear noise. Meanwhile, efficient QoT estimators based on analytical model and machine learning (ML) model are investigated and compared in depth.

Firstly, assisted by sparse fast Fourier transform (S-FFT), high-accuracy and low-complexity multi-parameter monitoring techniques for flexible optical networks are proposed to monitor modulation format, TO, FO and FOD. Specifically, a blind and fast modulation format identification (MFI) scheme is proposed with high identification accuracy at low OSNR to identify quadrature phase shift keying (QPSK), 16, 32, and 64 quadrature amplitude modulation (QAM). Then, an accurate and low-complexity TO/FO synchronization scheme based on S-FFT is proposed. The proposed scheme consists of coarse timing/frequency synchronization, fine timing synchronization, and fine frequency synchronization. For the drift feature of FO, an S-FFT-based FOD monitoring scheme is further proposed, by which the optimum performance and the minimum hardware cost of FO estimation (FOE) are achieved simultaneously.

In addition, to handle OSNR monitoring accuracy degradation induced by fiber nonlinearity, a modulation-format-transparent and accurate joint linear and nonlinear noise monitoring scheme is proposed based on the calculation of correlation between two spectral components at the upper and lower sideband of the signal spectrum. Different characteristics of flat linear noise spectrum and non-flat nonlinear noise spectrum are used to distinguish the influences on the correlation value from the two noise sources. The performance of the proposed scheme is numerically and experimentally verified in up-to-7 channel WDM systems over a 915 km single mode fiber (SMF) link.

Finally, a comprehensive comparative study of QoT estimation for WDM systems using artificial neural network (ANN)-based ML models and Gaussian noise (GN)

model-based analytical models is conducted. To obtain the best performance for comparison, all the system parameters for GN-based models are optimized in a brute-force manner. For ML models, the number of neurons, activation function, and the number of layers are optimized. In simulation settings, GN-based analytical models generally outperform ANN models while in experimental settings, however, inaccurate knowledge of various link parameters degrades GN-based models, and ML generally estimates the QoT with better accuracy. However, ML models are temporally less stable and less generalizable to different link configurations. Potential network capacity gains resulting from improved QoT estimators and reduced operating margins are also briefly studied.

Publications

Journal:

1. **Jianing Lu**, Gai Zhou, Qirui Fan, Dengke Zeng, Changjian Guo, Linyue Lu, Jianqiang Li, Chongjin Xie, Chao Lu, Faisal Nadeem Khan, and Alan Pak Tao Lau, "Performance comparisons between machine learning and analytical models for QoT estimation in WDM systems (invited paper)," Journal of Optical Communications and Networking 13(4), B35-B44 (2021).
2. **Jianing Lu**, Gai Zhou, Jing Zhou, and Chao Lu, "Joint linear and nonlinear noise monitoring technique based on spectrum analysis," Opt. Express 28(24), 36953-36971 (2020).
3. **Jianing Lu**, Qiong Wu, Hexun Jiang, Songnian Fu, Ming Tang, and Chao Lu, "Efficient Timing/Frequency Synchronization Based on Sparse Fast Fourier Transform," J. Lightwave Technol. 37(20), 5299-5308 (2019).
4. **Jianing Lu** and Chao Lu, "Frequency offset drift monitoring: enabling simultaneously optimum performance and minimum cost of frequency offset estimation," Opt. Lett. 44(15), 3753-3756 (2019).
5. **Jianing Lu**, Zhongwei Tan, Alan Pak Tao Lau, Songnian Fu, Ming Tang, and Chao Lu, "Modulation format identification assisted by sparse-fast-Fourier-transform for hitless flexible coherent transceivers," Opt. Express 27(5), 7072-7086 (2019).

Conference paper:

1. **Jianing Lu**, Alan Pak Tao Lau and Chao Lu, "Enabling simultaneously optimum performance and minimum cost of frequency offset estimation with sparse-FFT-assisted monitoring scheme," 45th European Conference on Optical Communication (ECOC 2019), Dublin, Ireland, 2019, pp. 1-4.

2. **Jianing Lu**, Qiong Wu, Hexun Jiang, Songnian Fu, Ming Tang and Chao Lu, "Sparse-fast-Fourier-Transform Assisted Timing/Frequency Synchronization for Optical Coherent Receivers," 2019 24th OptoElectronics and Communications Conference (OECC) and 2019 International Conference on Photonics in Switching and Computing (PSC), Fukuoka, Japan, 2019, pp. 1-3.
3. Qirui Fan, **Jianing Lu**, Gai Zhou, Dengke Zeng, Changjian Guo, Linyue Lu, Jianqiang Li, Chongjin Xie, Chao Lu, Faisal Nadeem Khan, and Alan Pak Tao Lau, "Experimental Comparisons between Machine Learning and Analytical Models for QoT Estimations in WDM Systems," in Optical Fiber Communication Conference (OFC), San Diego, CA, 2020, paper M2J.2.
4. Faisal Nadeem Khan, Qirui Fan, **Jianing Lu**, Gai Zhou, Chao Lu, and Alan Pak Tao Lau, "Applications of machine learning in optical communications and networks," in Optical Fiber Communication Conference (OFC), San Diego, CA, 2020, paper M1G.5

Acknowledgements

In August 2018, after receiving my master's degree, I joined the Photonics Research Centre, the Hong Kong Polytechnic University to pursue the Ph.D. degree. In the past three years, I have gained a lot in life and scientific research. I feel very lucky with this choice three years ago. I would like to thank the Hong Kong Polytechnic University for providing me with such an excellent research platform and living environment and the Research Grant Council (RGC) of the Hong Kong SAR government for financial support with the Hong Kong Ph.D. fellowship .

First of all, I would like to express sincere gratitude to my supervisor, Professor Lu Chao. As early as I was a master student, I had heard of the excellent academic reputation of Prof. Lu and his optical communication research group in PolyU. With the recommendation of Prof. Fu Songnian, my supervisor during my master study, I applied for and successfully received the offer from Prof. Lu. I am really grateful to Prof. Lu for his support. During my study and scientific research in PolyU, Prof. Lu not only provided me a lot of valuable suggestions, but also gave me sufficient research freedom, and provided me with a very good experimental platform, so that I can make my own research achievements. Whenever there is progress or doubt in research, we will have an in-depth discussion. With his suggestion, I can always make further discoveries. Prof. Lu is careful in revising my paper, which has improved the presentation of my research work. With his busy schedule, he can still arrange everything in an orderly manner. This also urges me to work harder in order to make greater achievements in my future study and work. In addition, in my life, Prof. Lu also gave me a lot of care and help. It has been a pleasure to be a student of Prof. Lu.

I would also like to thank Prof. Alan Pak Tao Lau for his concern and help in my

study and life. We had a lot of valuable discussions during which my ability and knowledge have been greatly improved.

Secondly, I would like to thank my colleagues Fan Qirui, Zhou Gai, Faisal Khan and others who have worked together with me. They have provided me with a lot of important assistance in both theoretical analysis and experimental investigation.

I would also like to thank Dr. Zhao Zhiyong, Dr. Tan Zhongwei, Cui Jingxian, Wang Zhuo, Luo Huaijian, Dr. Huang Dongmei, Yan Yaxi, Qu Jiaqi, Wu Xiong, Yang Zongru, Chen Shuyan, and all other colleagues for their friendship and for making the period of my research work immensely enjoyable.

I would also like to take this opportunity to thank Prof. Yu Changyuan in our group for his help and guidance during my Ph.D. study; Dr. Li Jianqiang in Alibaba group for his help and guidance during my research cooperation and internship with Alibaba and Dr. Dong Zhenhua in Huawei Technologies for his help and guidance during my research cooperation work with Huawei.

I would like to thank my parents for their support and love always.

Special thank goes to my girlfriend for her support, love, and company.

April, 2021

Statement of Originality

The following contributions reported in this thesis are claimed to be original.

1. I propose and demonstrate a blind and efficient MFI scheme for hitless flexible coherent transceiver. Based on the 4^{th} power transform and partition of QPSK-like points, the proposed MFI shows high accuracy for QPSK and 16/32/64QAM. Moreover, the complexity is substantially reduced by S-FFT comparing with previously proposed schemes.
2. I propose and demonstrate an S-FFT assisted efficient and low-complexity TO/FO synchronization scheme with the optimized training symbols (TSs). For coherently detected signals, not only the FO effect on the TO synchronization is eliminated, but the FO value is also simultaneously obtained for subsequent FO compensation. By aliasing the received signal with a proper subsampling rate, highly accurate TO synchronization can be achieved even in the region of very low SNR, while the complexity is greatly reduced.
3. I propose and demonstrate a FOD monitoring scheme based on S-FFT, by which optimum performance and minimum cost of FOE are achieved simultaneously. A downsampling process is further proposed to reduce the complexity of subsequent FFT-FOE.
4. I propose and demonstrate a joint linear and nonlinear noise estimation scheme based on spectrum analysis. The proposed scheme is modulation format-transparent and without DSP-induced noise. High estimation accuracy over a wide launch power range for single channel and WDM transmission systems with

various parameter settings are verified by both simulations and experiments over a real long-reach optical path link.

5. I conduct a detailed simulation and experimental comparison study between optimized GN-model-based analytical models and the ANN-based ML models for QoT estimation in WDM systems in the presence of nonlinear distortions.

Contents

List of abbreviations

A

ACF	Amplitude correlation function
ADC	Analog-digital convertor
ANN	Artificial neural network
AOM	Acousto-optic modulator
ASE	Amplified spontaneous emission
ASK	Amplitude-shift keying
AWG	Arbitrary-waveform generator
AWGN	Additive white Gaussian noise

B

B2B	Back-to-back
BER	Bit error rate
BPD	Balanced photodetector
BPS	Blind phase search
BPSK	Binary phase-shift keying

C

CC	Computational complexity
CD	Chromatic dispersion
CDC	Chromatic dispersion compensation
CDR	Correct detection rate
CMA	Constant modulus algorithm
CMP	Correct monitoring probability
COI	Channel of interest
CPR	Carrier phase recovery

D

DA	Data-aided
DAC	Digital-analog convertor
DBP	Digital backpropagation

DC	Direct current
DCF	Dispersion compensation fiber
DD	Direct detection
DD-LMS	Decision directed-least mean square
DGD	Differential group delay
DSO	Digital oscilloscope
DSP	Digital signal processing
DWDM	Dense wavelength division multiplexing

E

ECL	External cavity lasers
EDFA	Erbium-doped fiber amplifier
EGN	Enhanced-Gaussian noise
EON	Elastic optical network
ESNR	Electrical signal-to-noise-ratio
EVM	Error vector magnitude

F

FEC	Forward error correction
FFT	Fast Fourier transform
FIR	Finite impulse response
FO	Frequency offset
FOD	Frequency offset drift
FOE	Frequency offset estimation
FWM	Four-wave-mixing

G

GN	Gaussian noise
GPS	Global positioning systems
GVD	Group-velocity dispersion

I

ICI	Inter-channel interference
IGN	Incoherent Gaussian noise
IM	Intensity modulation

I/O	Input/output
I/Q	In-phase/Quadrature
ISI	Inter-symbol interference

K

KNN	K-nearest neighbors

L

LO	Local oscillator
LP	Launch power
LWN	Local white noise

M

MCI	Multi-channel interference
MFI	Modulation format identification
MIMO	Multi-input-multi-output
ML	Machine learning
MMA	Multi-modulus algorithm
MPSK	Multi-phase shift keying
MSE	Mean square error
MZM	Mach-Zehnder modulator

N

NF	Noise figure
NLI	Nonlinear interference
NSE	Nonlinear Schrödinger equation

O

OA	Optical amplifier
OBPF	Optical bandpass filter
OPM	Optical performance monitoring
OSA	Optical spectrum analyzer
OSNR	Optical signal-to-noise ratio

P

PAPR	Peak-to-average power ratio
PBC	Polarizing beam combiner

PBS	Polarizing beam splitter
PC	Polarization controller
PD	Photodetector
PDM	Polarization division multiplexing
PMD	Polarization mode dispersion
PS	Probabilistic-shaped
PSD	Power spectrum density
PSK	Phase shift keying

Q

QAM	Quadrature amplitude modulation
QoT	Quality of transmission
QPSK	Quadrature phase shift keying

R

RDE	Radius-directed equalization
ROADM	Reconfigurable optical add-drop multiplexer
ROF	Roll-off factor
Rx	Receiver side

S

S&C	Schmidl & Cox
SCI	Self-channel interference
SE	Spectral efficiency
S-FFT	Sparse fast Fourier transform
SLA	Service level agreement
SOA	Semiconductor optical amplifier
SNR	Signal-to-noise ratio
SPM	Self-phase modulation
SSFM	Split-step Fourier method
SMF	Single mode fiber
SSMF	Standard single mode fiber
SVM	Support vector machine

T

TDM	Time division multiplexing
TO	Timing offset
TS	Training symbol
Tx	Transmitter side

V

VOA	Variable optical attenuator
VV	Viterbi-Viterbi

W

WDM	Wavelength division multiplexing
WSS	Wavelength selective switch

X

XCI	Cross-channel interference
XPM	Cross-phase modulation

List of Figures

List of Tables

Chapter 1

Introduction

In this Chapter, an introduction to fundamentals of digital coherent optical fiber communication systems including the architecture of digital coherent systems, impairments in optical fiber channel, and corresponding standard digital signal processing (DSP) flow are given first. Then, overviews of optical performance monitoring (OPM) techniques and quality of transmission (QoT) estimation will be provided. After the introduction of existing methods, new challenges for OPM and QoT estimation in next-generation optical transmission systems and networks are discussed. Finally, the research objectives and organization of the thesis are provided.

1.1 Fundamentals of Digital Coherent Optical Fiber Communication Systems

Since the beginning of the 21st century, the explosive growth of interactive information has spread to every corner of social life. The continuous upgrade of the Internet scale, the increase in the number of users, and the rapid development of high-capacity services such as social networking, cloud computing, data centers, online games, 5G, mobile clients, high-definition video streaming, and the concept of Internet of Things put forward higher requirements for transmission capacity of the backbone networks. According to the white paper published by Cisco, from 2017 to 2022, the annual compound growth rate of global communication network capacity will be as high as 26% [1]. By 2022, the global monthly IP traffic has reached 396 EB, larger than three times the amount in 2017, as shown in Fig. 1-1. Faced with such an urgent situation, it is imperative to build larger-scale and larger-capacity backbone transmission systems and networks. The current system with single channel transmission capacity of 400 Gb/s will gradually be upgraded to 800 Gb/s, 1 Tb/s, or even higher rate [2]. As a consensus of academia and industry, digital coherent optical fiber communication techniques will always play a vital role.

Fig. 1-1. Cisco VNI forecasts 396 EB per month of IP traffic by 2022. [1]

The most important element of a digital coherent optical fiber communication system is the digital coherent receiver and the digital signal processing algorithm associated with it. Firstly, at the receiver-side (Rx), coherent detection is used to detect the modulated optical signal. In coherent detection, the optical signal and the local oscillator (LO) light are mixed so that all the information of the amplitude, phase, and polarization state of the optical field can be recovered. Such detection strategy makes it possible to employ advanced modulation format with high spectral efficiency (SE) and polarization division multiplexing (PDM) technology [3]. Since the weak optical signal can be amplified by the LO, the receiving sensitivity of the coherent receiver is greatly improved. Secondly, after coherent detection and photoelectric conversion, the signal processing can be realized in the digital domain after sampling by high-speed analog-to-digital converter (ADC). Powerful digital signal processing (DSP) algorithms can be used to compensate and mitigate the transmission impairments suffered by the optical signal, so as to effectively improve the performance of the transmission systems [4]. Meanwhile, the optical performance monitoring (OPM) techniques operated in the digital domain have been developed to evaluate the quality and parameters of the optical signal, by which the link situation can be monitored, and the operators can grasp the current status of the communication systems [5].

The advantages of coherent detection have made it the predominant technique when implementing a digital optical fiber communication system. We have been witnessing the development and commercialization of 100G and 400G systems [6]. In the near future, the optical communication system with 800 Gbit/s and beyond 1 Tbit/s per channel will further improve the transmission capacity to a higher level [2]. Although

the developments of digital coherent techniques have greatly improved the transmission capacity, for the optical signal modulated by higher-level modulation format with higher symbol rate and longer transmission distance, the effect of transmission impairments will be more severe [7]. In addition, in order to meet the high-performance and resource-saving requirements of future optical fiber communication systems, optical networks are evolving from the traditional fixed grid and path-based structure to flexible elastic optical networks (EONs) [8]. Therefore, it is necessary to adaptively change the bandwidth and route of the optical signal according to the current capacity requirements and the condition of the optical fiber link. The currently employed DSP algorithms and OPM techniques are facing more stringent challenges from the perspective of both performance and complexity. Moreover, to further adapt to the requirements of low-margin and EONs, the quality of transmission (QoT) estimation plays a critical role to enable the full utilization of the link capacity [9]. Advanced OPM and QoT estimation techniques will be key modules for next-generation optical transmission systems and networks.

1.1.1 Architecture of Digital Coherent Systems

In order to realize a large-capacity, long-distance optical fiber communication transmission system, coherent detection combined with DSP at the Rx has become the consensus of industry and academia [3, 4]. Compared with the traditional intensity-modulation direct-detection (IM-DD) scheme, there are two advantages in the digital coherent optical fiber communication system: firstly, the amplitude, phase, frequency, and two orthogonal polarization states of the optical field are fully preserved in the detected signal, which makes it possible to employ the high-order modulation format.

Secondly, at the Rx, powerful DSP algorithms can be used to compensate the transmission impairments. As shown in Fig. 1-2, the structure of digital coherent optical fiber communication system can be divided into three parts: digital transmitter, optical fiber transmission link, and digital coherent receiver.

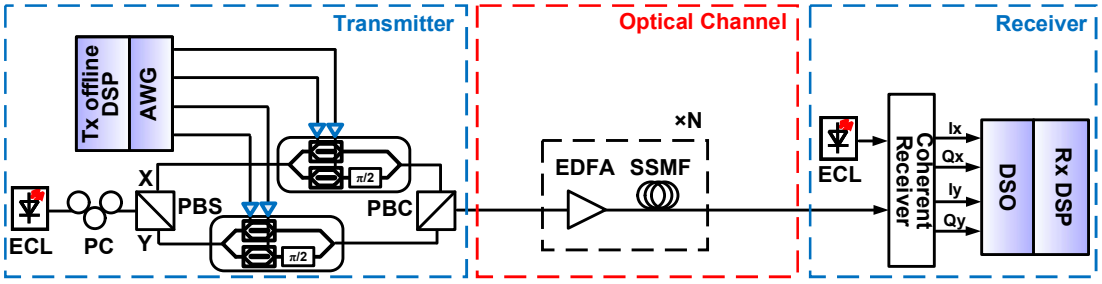

Fig. 1-2. The structure of digital coherent optical fiber communication system. ECL: external cavity laser. DSO: digital oscilloscope. EDFA: Erbium-doped fiber amplifier. SSMF: standard single mode fiber. DSP: digital signal processing. PC: polarization controller. PBS: polarization beam splitter. PBC: polarization beam combiner. AWG: arbitrary waveform generator.

1.1.1.1 I/Q Modulator-based Digital Transmitter

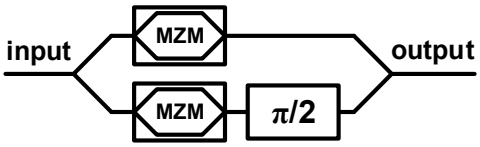

Fig. 1-3. Structure of I/Q modulator.

In digital coherent optical transmission systems, the electro-optical conversion is realized by In-phase/Quadrature (I/Q) modulator. As shown in Fig. 1-3, I/Q modulator consists of two dual-drive Mach-Zehnder modulators (MZM) and a 90° phase shifter. Assuming that the extinction ratio between two arms of MZM is large enough, the transfer function of MZM can be expressed as

$$\begin{aligned} h_{\mathrm{mod}} &= \frac{1}{2}\left(\exp(j\frac{V_1(t)\pi}{V_\pi}) + \exp(j\frac{V_2(t)\pi}{V_\pi}) \right) \\ &= \cos(\frac{V_1(t)-V_2(t)}{2V_\pi}\pi)\exp(j\frac{V_1(t)+V_2(t)}{2V_\pi}\pi) \end{aligned} \tag{1.1}$$

where $V_1(t)$ and $V_2(t)$ are driving voltage acting on two arms of MZM, respectively, and V_π is the half wave voltage. From Eq. (1.1), it can be found that both phase and amplitude modulations can be realized by MZM.

For I/Q modulator, after 90° phase shift, the output signal of one MZM is combined with the output signal from the other MZM. Then, the output signal of I/Q modulator can be expressed as

$$E_{out}(t) = E_{in}(t)\left(\cos(\frac{V_I(t)}{V_\pi}\pi) + j\cos(\frac{V_Q(t)}{V_\pi}\pi) \right) \tag{1.2}$$

where $V_{I/Q}(t)=V_1(t)=-V_2(t)$ in push-pull mode and $E_{\text{in}}(t)$ is the input optical field.

1.1.1.2 Optical Fiber Transmission Link

Long-reach optical fiber transmission link consists of several combinations of optical fiber and optical amplifier (OA). Conventionally, for a coherent optical fiber communication system, standard single mode fiber (SSMF) is employed with erbium-doped fiber amplifier (EDFA) which fully compensates the fiber loss. The impairments of SSMF and EDFA will be introduced in detail in Section 1.1.2.

1.1.1.3 Digital Coherent Receiver

The front-end of digital coherent receiver mainly consists of 90° hybrids and balanced photodetectors (BPDs) as shown in Fig. 1-4(a) [3]. Let's start from coherent detection for single-polarization optical signals. The optical fields of four outputs of the 90° hybrid are

$$\begin{bmatrix} E_{1x} \\ E_{2x} \\ E_{3x} \\ E_{4x} \end{bmatrix} = \frac{\sqrt{2}}{2} \begin{bmatrix} 1 & 1 \\ -1 & 1 \\ 1 & i \\ -1 & i \end{bmatrix} \begin{bmatrix} E_{Sx} + N_x \\ E_{LOx} \end{bmatrix} = \frac{\sqrt{2}}{2} \begin{bmatrix} (E_{Sx} + N_x) + E_{LOx} \\ -(E_{Sx} + N_x) + E_{LOx} \\ (E_{Sx} + N_x) + iE_{LOx} \\ -(E_{Sx} + N_x) + iE_{LOx} \end{bmatrix} \tag{1.3}$$

Four output mixing light is detected by two BPDs and the output electric currents are

$$S_{xi} = 2R\ \mathrm{Re}(E_{Sx}E_{LOx}^{*} + N_x E_{LOx}^{*}) \tag{1.4}$$

$$S_{xq} = 2R\ \mathrm{Im}(E_{Sx}E_{LOx}^{*} + N_x E_{LOx}^{*}) \tag{1.5}$$

where S_{xi} and S_{xq} are real and imaginary parts of the modulated signal. R is the responsivity of the PD. In practical PDM systems, polarization and phase diversities are required for the front-end of the coherent receiver, as shown in Fig. 1-4(b). Specifically, the signal light and the LO light are both split by a polarization beam splitter (PBS) before entering the 90° hybrids. XI, XQ, YI, YQ components can be obtained after photo-electrical conversion using BPDs.

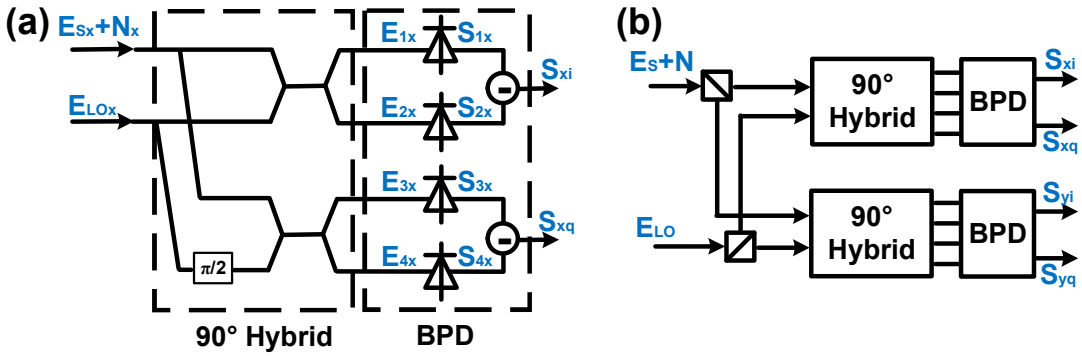

Fig. 1-4. (a) Front-end of single-polarization coherent receiver. (b) Front-end of dual-polarization coherent receiver.

1.1.2 Impairments in Optical Fiber Channel

In this Section, the impairments of SSMF and EDFA will be introduced, while the analysis of other fiber and OA types is omitted.

1.1.2.1 Optical Fiber Loss and Amplifier Noise

Due to the scattering and absorption phenomenon in optical fiber materials, the power of optical signal will decrease continuously in the process of transmission. Assuming that the initial optical power is P_{in} and the fiber length is L, the power of the optical signal after propagation can be expressed as

$$P_{out} = P_{in} e^{-\alpha L} \tag{1.6}$$

α is the attenuation coefficient of the optical fiber. Generally, we define the attenuation coefficient in dB/km scale and then α_{dB} is about 0.17 dB/km in the C-band communication window of the standard single mode fiber (SSMF). In order to increase the transmission distance of optical signal, optical amplifier (OA) must be used to compensate the signal attenuation in optical fiber link. Erbium-doped fiber amplifier (EDFA) and Raman amplifier are commonly employed OAs. However, while the optical signal is amplified by OA, amplified spontaneous emission (ASE) noise is introduced at the same time. Such kind of noise belongs to additive white Gaussian noise (AWGN), which will lead to the deterioration of the optical signal-to-noise ratio (OSNR) of the received signal, and thus seriously affect the signal quality.

Here, a basic analysis of ASE-induced OSNR degradation is provided. Signal attenuation in an optical fiber link will increase with the transmission distance. In order to maintain the power level of the optical signal, an OA needs to be employed to amplify the optical signal every 60-120 km [10]. EDFA is currently the dominant OA. EDFA will introduce ASE noise caused by amplification to the signal. In a long-distance optical fiber communication system, the longer the transmission distance, the more cascaded EDFAs are required in the link, and the larger the accumulated ASE

noise will be, reducing the OSNR. The ASE noise power introduced by a single EDFA in the bandwidth B_0 is [11]

$$P_{ASE}=2n_{sp}(G-1)hvB_0 \tag{1.7}$$

where n_{sp} is the particle number inversion parameter, which is related to the Erbium ion concentration, pump power, and input optical power of the EDFA. G is the EDFA gain. h is the Planck constant. v and B_0 are optical frequency and optical signal bandwidth respectively.

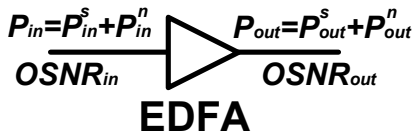

Fig. 1-5. Amplification model of single EDFA.

As shown in Fig. 1-5, the input signal of an EDFA includes optical signal power and noise power as $P_{in}=P_{in}^{s}+P_{in}^{n}$. Providing the gain G of EDFA and the OSNR of the input signal $OSNR_{in}=P_{in}^{s}/P_{in}^{n}$, the power of the signal and noise in the input signal are

$$P_{in}^{s}=P_{in}\frac{OSNR_{in}}{1+OSNR_{in}} \tag{1.8}$$

$$P_{in}^{n}=P_{in}\frac{1}{1+OSNR_{in}} \tag{1.9}$$

When the optical signal passes through EDFA, the output signal power is the input signal power amplified by G while the output noise power is the sum of the amplified power of the signal noise in the input signal and the ASE noise generated by the EDFA

$$P_{out}^{s}=GP_{in}^{s} \tag{1.10}$$

$$P_{out}^{n}=GP_{in}^{n}+P_{ASE} \tag{1.11}$$

The output signal $OSNR_{out}$ can be expressed as $OSNR_{out}=P_{out}^{s}/P_{out}^{n}$. Then we can obtain

$$\frac{1}{OSNR_{out}}=\frac{1}{OSNR_{in}}+\frac{2n_{sp}(G-1)hvB_0}{GP_{in}}(1+\frac{1}{OSNR_{in}}) \tag{1.12}$$

Generally, in order to ensure the quality of the received optical signals, the ASE noise power of EDFA is far less than the input optical power. With $P_{in}\gg 2n_{sp}(G-1)hvB_0$ and assuming the EDFA gain G is large enough $G\gg 1$, and $OSNR\gg 1$, the above formula can be further simplified to

$$\frac{1}{OSNR_{out}}-\frac{1}{OSNR_{in}}=\frac{2n_{sp}hvB_0}{P_{in}} \tag{1.13}$$

It can be concluded that every time passing through an EDFA, the accumulated ASE noise will increase and the OSNR will decrease. The reduced OSNR is related to the input power and gain of the EDFA. The right part of the above formula is defined as the OSNR cost caused by a single EDFA, expressed as

$$\delta_{EDFA}=\frac{2n_{sp}hvB_0}{P_{in}} \tag{1.14}$$

Among this formula, hvB_0 is a constant. Setting the bandwidth as 0.1 nm, there is $10\lg(hvB_0)=-58$, which is usually used to fast evaluate the OSNR of the link. In an optical fiber link, the fiber itself does not induce ASE noise and has no effect on OSNR. Assuming that the loss of each span in the link is fully compensated and the noise characteristics, gain, and input signal power of each EDFA keep the same, the OSNR after the N segments of fiber is:

$$OSNR_{out}^{N}=\frac{P_{in}}{2n_{sp}hvB_0N} \tag{1.15}$$

It can be seen that the output OSNR is proportional to the input power and inversely proportional to the number of EDFAs passed. The greater the input power, the larger the output OSNR, and the more EDFAs used, the smaller the output OSNR. Taking logarithm operation of Eq. (1.15), we have

$$OSNR_{out}^{N}(\text{dB})=P_{in}-F-10\lg N-10\lg(hvB_0) \tag{1.16}$$

where $F=10\lg(2n_{sp})$ is the noise figure (NF) of the EDFA.

1.1.2.2 Chromatic Dispersion

Chromatic dispersion (CD) refers to the different propagation speeds of different components of signal pulse in optical fiber [12], leading to pulse broadening which further results in inter-symbol interference (ISI). CD comes from the combined effect of material dispersion and waveguide dispersion. Material dispersion occurs due to that the refractive index of fiber material changes with wavelength, and the waveguide dispersion comes from the structure of the fiber waveguide. In general, the dispersion parameter D (in $ps/(km\cdot nm)$) is defined as

$$D=-\frac{2\pi c}{\lambda^2}\beta_2 \tag{1.17}$$

where β_2 is the group velocity dispersion coefficient. CD is a kind of linear impairment, which can be compensated in the optical domain by using dispersion compensation fiber (DCF). However, there are two drawbacks of DCF. Firstly, the dispersion of multi-wavelength signals can not be accurately matched, which leads to residual CD. Secondly, DCF will introduce higher fiber nonlinearity which will

severely deteriorate the quality of signal. Generally, for SSMF, D is about 15-20 $ps/(km \cdot nm)$ within the C-band window.

1.1.2.3 Polarization Mode Dispersion

SSMF can support two orthogonal polarization states. However, the imperfect symmetry caused by the manufacturing process will cause random birefringence in the optical fiber. The delay between signals in both polarizations is defined as differential group delay $\Delta\tau_{PMD}$ whose value is proportional to the square root of the fiber length

$$\Delta\tau_{PMD}=D_{PMD}\sqrt{L} \tag{1.18}$$

where D_{PMD} is the polarization mode dispersion (PMD) coefficient (in $ps/\sqrt{km}$) of the optical fiber, which is about 0.1 $ps/\sqrt{km}$ for SSMF. PMD is a major limiting factor in long-distance high-speed optical fiber communication systems.

1.1.2.4 Fiber Nonlinearity

The nonlinear effects in optical fibers generally include self-phase modulation (SPM), cross-phase modulation (XPM), four-wave-mixing (FWM), stimulated Raman scattering, and stimulated Brillouin scattering [13]. Nonlinearity is considered a fundamental limiting factor in optical fiber communication systems and is difficult to be fully compensated. For dispersion-unmanaged optical fiber communication systems, nonlinear noise behaves as AWGN, which can be hardly distinguished from ASE noise. At present, in the digital domain, digital backpropagation (DBP) and Volterra series filter have been proposed to partially compensate nonlinear effects at the Rx with high complexity. Theoretically, nonlinear effect can not be completely compensated and even the most powerful nonlinearity compensation algorithms are employed, the gain

in signal quality is unsatisfactory. A detailly analysis of fiber nonlinearity is provided in Chapter 4.

1.1.2.5 Frequency Offset

The digital coherent optical communication system generally adopts intradyne detection. The central wavelength of the lasers used as the transmitting carrier and the LO is unstable and the drift may vary from MHz to GHz. Therefore, there is normally a mismatch between the wavelength of the transmitting carrier and the LO. Frequency offset (FO) caused by such difference of central frequency will introduce a fast change of the signal phase and have a great influence on the signal quality. For the advanced modulation format where the phase plane is used to carry information, the FO estimation and corresponding compensation are necessary.

1.1.2.6 Phase Noise

For the digital coherent optical fiber communication system, since the linewidth of the semiconductor laser is not strictly 0 Hz, the phase noise will be introduced in the coherent detection process at the Rx. The phase noise can be modelled as a Wiener process [14]. The larger the linewidth of the laser, the faster the change of phase noise. The process of phase noise can be expressed as

$$\theta_p(t) = \int_{-\infty}^{t} \eta(t)dt \tag{1.19}$$

where $\theta_p(t)$ is the phase noise at time t, $\eta(t)$ is a Gaussian process with the mean value of 0 and variance of $2\pi\Delta f T_S$, and Δf is the combined linewidth of the two lasers. Phase noise will cause the received constellation to rotate which will result in wrong decision. Therefore, for the advanced modulation format with phase modulation, the

phase noise of the received signal must be further eliminated after FO compensation for correct demodulation of the signal.

1.1.3 Standard Digital Signal Processing Flow

After detecting by a coherent receiver, we obtain the electrical signals in X- and Y-polarizations, and then we process them in the digital domain to compensate the impairments suffered during the transmission process. In principle, all the linear distortions can be compensated using powerful DSP algorithms. In the last decade, DSP algorithms for coherent optical fiber communication systems have been extensively investigated and become mature. Here, a brief introduction of standard DSP flow for the single carrier system is provided, as shown in Fig. 1-6.

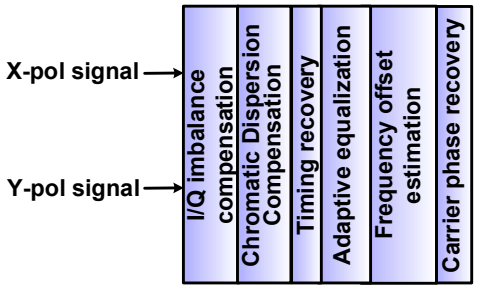

Fig. 1-6. Standard DSP flow.

1.1.3.1 I/Q Imbalance Compensation

While coherent detection is realized by the front-end of the coherent receiver, its nonideal characteristics will introduce power difference between I-component and Q-component of signals in two polarizations. Such a phenomenon is named I/Q imbalance. In order to guarantee the performance of the following DSP algorithms, I/Q imbalance needs to be compensated first. Generally, the Gram-Schmidt orthogonalization algorithm can be used for I/Q compensation [15].

1.1.3.2 Chromatic Dispersion Compensation

In principle, CD compensation can be operated in both time domain and frequency domain. If the CD value of the received signal is too large, the number of taps of the finite impulse response (FIR) filter required for time-domain CD compensation increase significantly, which greatly increases the complexity. Therefore, frequency domain-based CD compensation is preferred. If the CD value is unknown, it is necessary to estimate it before compensation. In general, we can use the best matching method [12] (that is, scanning within a large CD range to find the CD value which minimizes the error function) to get the estimated value of CD.

1.1.3.3 Timing Recovery

In practical systems, it is necessary to extract the clock information from the signal for sampling at the Rx. Generally, the Gardner algorithm [16] or digital square filtering algorithm [17] can be used to recover the clock carried by the signal.

1.1.3.4 Adaptive Equalization

The main function of the adaptive equalization module is to de-multiplex two mixed polarization signals to eliminate the effects of polarization rotation, PMD, and residual CD. Generally, adaptive equalization employs a 2×2 butterfly structure, which is composed of four FIR filters. For multi-phase shift keying (MPSK) modulation format with constant amplitude, the most commonly used adaptive equalization algorithm is the constant modulus algorithm (CMA) [4]. For 16QAM or higher-level modulation formats, it is necessary to adopt the multi-modulus algorithm (MMA) or decision-directed least mean square (DD-LMS) algorithm [4] for adaptive equalization.

1.1.3.5 Frequency Offset Estimation

Because the central wavelengths of the LO at the Rx and the transmitting laser at the Tx are not exactly the same, FO is introduced in coherent detection. The phase of the signal changes rapidly due to FO. After adaptive equalization, FO estimation (FOE) should be conducted to estimate FO, and then corresponding compensation can be operated. The most used FOE method is fast Fourier transform-based FOE (FFT-FOE), where the frequency which maximizes the peak in the spectrum of the signal after 4^{th} power calculation is identified as FO value [18].

1.1.3.6 Carrier Phase Recovery

The phase noise introduced by non-zero laser linewidth will cause the rotation of the signal constellation. In order to recover the signal, carrier phase recovery (CPR) is necessary to handle residual phase noise after FOE. Generally, phase noise is estimated based on window-averaging because of its slowly varying characteristic. The commonly used CPR methods are the Viterbi-Viterbi (VV) algorithm [19] and the blind phase search (BPS) algorithm [20].

1.2 Optical Performance Monitoring for Digital Coherent Systems

In principle, OPM can be considered to monitor any optical parameter e.g., OSNR, CD, PMD, FO, phase noise, symbol rate, modulation format, and so on. However, for many years, the OPM techniques have been referred to as “OSNR monitoring” because for old low-capacity optical networks, the nonlinear noise is neglected and we can only focus on the linear noise (generated by ASE noise from OA) imposed OSNR, which determines the signal quality as well as transmission performance. OSNR refers to the

ratio of the total optical signal power to noise power within a reference noise bandwidth. EDFAs are widely used in optical transmission systems to compensate fiber loss. However, the use of EDEA is often accompanied by adding ASE noise to useful optical signals. With the increase of transmission distance, optical signals also pass through more and more EDFAs, and ASE noise accumulates gradually with EDFAs, thereby degrading signal quality and affecting transmission performance. In practical applications, it is usually necessary to monitor the OSNR of a specific node in optical networks. The significance of OSNR monitoring is reflected in the following aspects: (1) OSNR can be used to predict the BER performance of the corresponding node. The higher the OSNR, the higher the signal transmission performance. The OSNR-BER curve is often measured and plotted in long-distance transmission experiments to reflect the system performance; (2) OSNR can be used to evaluate the overall performance of the network and provide reference information for flexible configuration, control, and optimization of optical link path; (3) Fault diagnosis can be realized by OSNR monitoring. Abnormal fluctuations of the OSNR in the optical network can help the network management system quickly locate and avoid risk links. Overall, OSNR monitoring technology is an indispensable part of future intelligent optical networks. However, for future high-capacity and dense WDM systems and flexible optical networks, the nonlinear noise gradually becomes a very significant impairment of the signal. Therefore, it is essential to develop an effective method to monitor both linear and nonlinear noise [5].

On the other hand, to accommodate increasingly heterogeneous traffic and better adapt transmissions to real-time link conditions such as environmental change, aging,

etc, current fixed optical networks are expected to evolve to future flexible and adaptive optical networks. For flexible optical networks, hitless flexible coherent transceiver is proposed to realize adaptive rate transmission through modulation format switching according to current link margin and traffic requirements without transmission interruption [21]. In this connection, conventional OPM structure which only takes relatively stable OSNR into account will be unable to meet the requirements. On the contrary, fast-varying optical parameters such as modulation format, FO, timing offset (TO), and FO drift (FOD), et. al. introduced by optical path switching need to be monitored in a real-time manner. Therefore, a high-accuracy and low-complexity multi-parameter monitoring scheme is worthy of further study. Here, a brief review of conventional OSNR monitoring techniques is provided.

1.2.1 Monitoring Techniques for ASE Noise Dominated OSNR

1.2.1.1 Out-of-Band OSNR Monitoring

The key to OSNR monitoring is how to separate optical signal power from noise power. Early OSNR monitoring was mainly done in the optical domain, the most classic of which is the out-of-band interpolation OSNR monitoring which uses linear interpolation technique with an optical spectrum analyzer (OSA) [22]. Its basic principle is shown in Fig. 1-7. In a traditional WDM system, since the guard interval between channels is greater than the channel bandwidth, the power distributed within the guard interval only contains noise, which directly reflects the noise level. For the linear interpolation technique, the out-of-band noise levels on both sides of the channel are used to estimate the in-band noise level. Then, the power of the signal and the noise can be easily calculated and separated to calculate the OSNR.

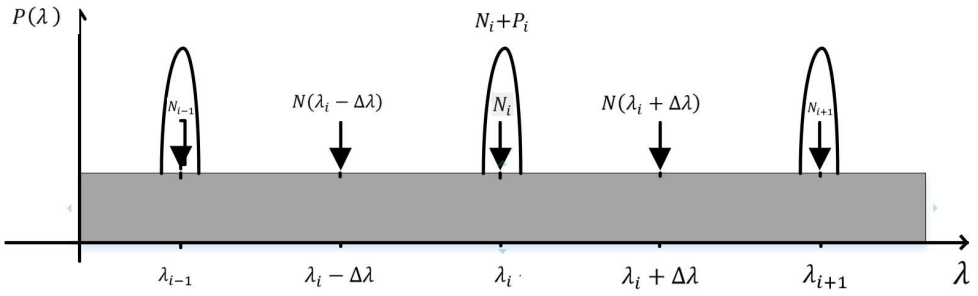

Fig.1-7. Out-of-band linear interpolation based OSNR monitoring.

The linear interpolation technique estimates the in-band noise power spectrum intensity as

$$N_i(\lambda_i) = \frac{N(\lambda_i - \Delta\lambda) + N(\lambda_i + \Delta\lambda)}{2} \tag{1.20}$$

where $N_i(\lambda_i)$ is the noise power intensity of the i[th] wavelength channel, $N(\lambda_i + \Delta\lambda)$ and $N(\lambda_i\text{-}\Delta\lambda)$ are the power intensity of the out-of-band noise on the right and left side of the i[th] wavelength channel. The noise power intensity in the band is obtained by taking the average of $N(\lambda_i + \Delta\lambda)$ and $N(\lambda_i\text{-}\Delta\lambda)$. Finally, the OSNR value of the system is estimated by the OSNR definition.

1.2.1.2 In-Band OSNR Monitoring

With the deployment of dense WDM technology, the channel spacing is getting smaller and smaller. Moreover, the EDFA gain and ASE noise experienced by signals at different wavelengths are different, as well as the in-band and out-of-band noise. As shown in Figure 1-8, in a dense WDM (DWDM) optical transmission system, adjacent channels are densely arranged and partially overlapped. In such a case, the out-of-band power intensity obviously can not represent the level of noise, making out-of-band OPM technology based on linear interpolation no longer applicable.

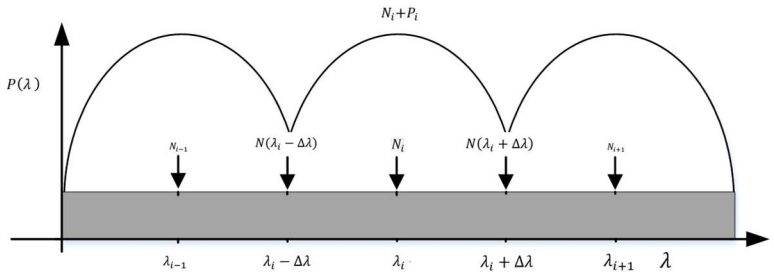

Fig.1-8. DWDM system with small channel spacing.

The introduction of optical filters can also cause a similar problem. For example, when performing wavelength routing and selection in the optical domain, the optical signals transmitted through different paths may pass through multiple reconfigurable optical add-drop multiplexers (ROADMs) [23] and undergo different optical filtering. As shown in Fig. 1-9, due to the effect of optical filtering, part of the out-of-band noise is filtered, but the in-band noise is not affected. Therefore, in this scenario, the noise power level cannot be obtained by the linear interpolation technique. The out-of-band OPM technology is no longer applicable. In short, the out-of-band OSNR monitoring technology is no longer applicable to current advanced optical fiber communication systems.

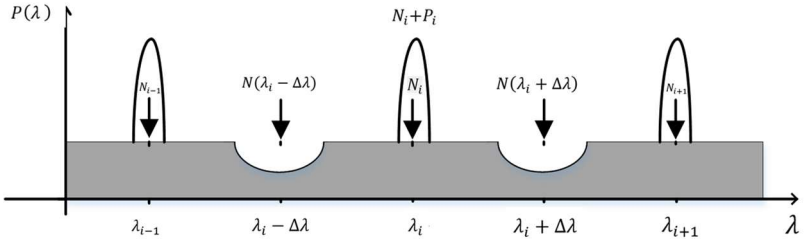

Fig.1-9. Due to the effect of additional out-of-band optical filtering, part of the out-of-band noise is filtered out.

1.2.1.3 In-band OSNR Monitoring

In order to overcome the drawbacks of the out-of-band OSNR monitoring techniques, the in-band OPM technology is proposed. The in-band monitoring method uses the

different characteristics of noise and signal to separate signal power from noise power. In single-polarization optical transmission systems, polarization nulling-based OSNR monitoring can be applied [24]. However, this method is not suitable for current polarization division multiplexing (PDM) systems. With the rapid development of DSP, OSNR monitoring can be realized in the digital domain. A popular method is based on received signal distributions and error vector magnitude (EVM) calculation [25]. For a PDM coherent system with M-QAM signal, after being processed using standard DSP algorithms, linear distortions such as CD, PMD, laser FO, and phase noise can be compensated. The m^{th} received symbol can be represented as

$$r_m = s_m + n_m \tag{1.21}$$

where s_m and n_m are the m^{th} modulated M-QAM signal and its suffered ASE noise, respectively. For the EVM-base method, the OSNR is calculated as

$$OSNR_{estimated} = \frac{P_{signal}}{P_{ASE}} = \frac{E(|\hat{s}_m|)}{E(|r_m - \hat{s}_m|)} \tag{1.22}$$

where P_{signal} and P_{ASE} accounts for the signal power and ASE noise power, respectively. $E(\cdot)$ is expectation operation and $\hat{\cdot}$ is the decision of the symbol. Besides the EVM-based method, statistical moment-based [26] and cyclostationary property-based method [27] can be used for OSNR monitoring in the digital domain without consideration of fiber nonlinearity.

1.2.2 OSNR Monitoring in the Presence of Fiber Nonlinearity

However, as analyzed above, traditional OSNR definition can only reflect the effect of ASE noise of the link and can not reflect the strength of the nonlinear influence. Nowadays, for coherent optical communication systems with large capacity, high

spectral-efficiency (SE), and dynamic reconfiguration, the effect of fiber nonlinearity is nonnegligible. In previous studies, researchers have shown that the statistical distribution of nonlinear noise can be approximated as Gaussian distribution, which indicates that the nonlinear noise has similar characteristics as that of ASE noise [28]. It seems difficult to distinguish the distribution of linear and nonlinear noise from the signal constellation after demodulation. One solution for OSNR monitoring in the presence of fiber nonlinearity is based on EVM and the correlation function of amplitude noise of the adjacent received signal [29]. The principle of this method is that due to the signal-correlated fiber nonlinearity, there is a certain correlation between the adjacent symbols. Then, a fitting aprocess can be used for OSNR calibration. In [30], amplitude correlation function (ACF) of adjacent symbols and polarizations after adaptive equalization is used for calibration.

1.3 Quality of Transmission Estimation for Digital Coherent Systems

The key features of EONs are dynamic lightpath provisioning, baud rate, and modulation format adaptation based on QoT when the SNR of each channel is estimated. Accurate QoT estimation is under intense investigations recently to enable low-margin networks for maximal network efficiency [31]. In a WDM environment, XPM induced nonlinear distortions affect the neighboring channels and thus the SNR of one channel actually depends on the signal power of all other channels in a complicated manner, rendering QoT estimations for WDM systems a non-trivial task. Over the past few years, several classes of approaches for QoT estimation in optical networks have been proposed. These approaches can be broadly classified into three main types: (1) Techniques based on simulation models, such as the split-step Fourier

method (SSFM) [32], that exploit the information about various physical layer impairments to predict the QoT of a given lightpath with good accuracy. These approaches typically involve high computational complexity (and hence require more computation time) thus limiting their application in large and dynamic optical networks. (2) Techniques based on faster analytical formulas, such as Gaussian noise (GN) models [28, 33], the accuracy of which increases with the model complexity, resulting in a trade-off between them. (3) Machine learning (ML)-based approaches [9, 34, 35] that learn the relationship between monitored field data and the QoT of already deployed lightpaths to predict the QoT of unestablished lightpaths.

1.3.1 Analytical Model based QoT Estimation

For linear noise, the traditional ASE noise accumulation model can be used for the calculation of ASE noise introduced by EDFAs. For nonlinear noise modeling, GN models have been intensely investigated and generally offer an acceptable, although not as accurate as simulation models, performance estimation with moderate computational complexity [28, 33]. Until now, the GN model based on numerical integration to obtain the nonlinear interference (NLI) has been the most commonly used version [33]. Meanwhile, closed-form approximations of the GN model which can complete QoT estimations in picoseconds, are proposed to reduce the complexity while the accuracy is somehow sacrificed [36]. Detailed analysis of the ASE noise accumulation model and the GN model is provided in Chapter 4.

1.3.2 Machine Learning Model base QoT Estimation

ML-based QoT estimation has gained significant attention recently due to the fact that ML algorithms can effectively learn and discover the hidden correlations in big data

typically encountered in large and dynamic optical networks. Several ML-based QoT estimation techniques have been proposed in the literature. In [34], four different ML algorithms including artificial neural network (ANN), support vector machine (SVM), *K*-nearest neighbors (KNN), and logistic regression are introduced for QoT prediction and their performances are compared. The features of the lightpath used for the training of four ML models include the number of spans, number of hops, average and maximum link lengths, modulation format type, and attenuation and CD of the links. The results demonstrate that all considered ML models could accurately predict the QoT of more than 90% lightpaths with ANN achieving the best accuracy of 99% as shown in Fig. 1-10. Similarly, in [34], KNN and random forest algorithms are applied to predict whether the bit-error rates BERs of candidate lightpaths meet the required system threshold by using the network parameters such as traffic volume, modulation format, the total length of the lightpath, length of the longest link, and the number of links in the lightpath as input features. It has been shown that the use of three specific features, i.e., the total length of the lightpath, traffic volume, and modulation format leads to the best QoT prediction accuracy. The above-mentioned QoT estimation methods mainly predict whether the QoT of the lightpath under investigation is above or below a certain threshold. However, for realizing low-margin network operations, ML-based QoT estimation techniques that can accurately quantify the QoT of lightpaths in terms of actual SNR, *Q*-factor, BER, etc. are required. This can enable the network operators to get accurate information about the residual margin (i.e., the difference from the acceptable threshold), and thus avoid network over-dimensioning.

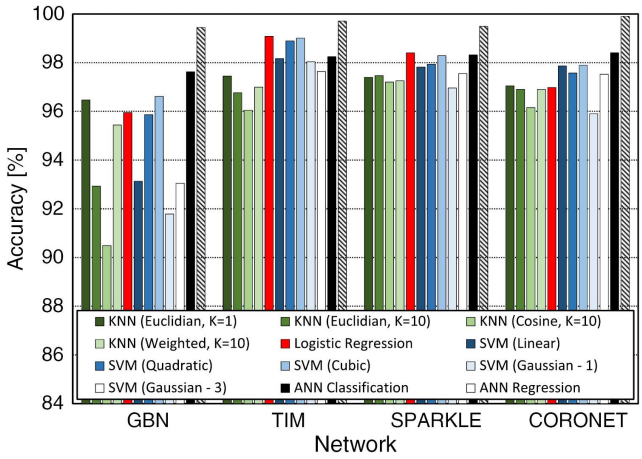

Fig. 1-10. QoT estimation accuracies using various ML algorithms for four different network topologies.

1.4 New Challenges for OPM and QoT estimation

For next-generation optical transmission systems and networks, more stringent requirements arise for both OPM and QoT estimation techniques. For OSNR monitoring, indeed, nowadays one can make full use of optical field information to perform analysis in the digital domain with the development of coherent detection and DSP. The calculation of electrical SNR (ESNR) can be realized by powerful and flexible DSP algorithms, which provides great convenience for engineers. Although a number of DSP-based OSNR monitoring methods have been proposed, e.g. the ESNR can be calculated based on EVM, Stokes-vector, cyclostationary property, and statistical moments or aided by training symbols, these methods do not take nonlinear noise into account. As analyzed and verified extensively in previous works, in a long-haul transmission link with sufficient accumulated CD and fiber nonlinearity, the nonlinear noise can be approximately modeled as additive Gaussian noise in the time domain. Therefore, it is difficult to distinguish ASE noise induced by EDFA and nonlinear noise. The presence of nonlinear noise not only leads to an underestimation of OSNR, but also makes it difficult to accurately evaluate the link condition. So far,

several schemes have been proposed to eliminate the OSNR estimation error induced by nonlinearity. For example, nonlinearity can be measured using inserted pilot signals [37, 38]. However, the SE and system flexibility are sacrificed. In [29], the EVM-based method is employed with the NLI fitting using amplitude noise correlation between neighboring symbols after CPR, while in [30], the statistical moments-based SNR estimation method is used with ACFs between two symbols of the signal to estimate the impact of NLI. It should be noted that such kind methods should be conducted with the aid of several DSP demodulation steps (after CPR [29] or after adaptive equalization [30]). From the perspective of the practical system, they not only exhibit relatively high power-consumption and unavoidable DSP-induced noise (e.g. the taps of adaptive equalizers do not converge perfectly) [4, 39], but also are not transparent to modulation formats and hence unsuitable for flexible optical networks where multiple possible formats can be employed for data transmission [8]. On the other hand, it remains highly desirable to distinguish and monitor the linear and nonlinear noise simultaneously (not only OSNR monitoring), enabling comprehensive system analysis for operators. ML-based methods have shown some potential, but it remains challenging to acquire a huge amount of high-quality training datasets in practical systems. A simpler and effective method to monitor both linear and nonlinear noise is still worthy of studying.

Secondly, efficient multi-parameter monitoring modules are required in EONs, where the optical parameters and impairments resulted from fast-varying and heterogeneous transmission links change rapidly. One of the key components in EONs is the adaptive/flexible receiver DSP units supporting multiple baud rates, bandwidths,

and modulation formats. Flexible transceivers capable of providing arbitrary SE and spectrum bandwidth according to traffic needs and link conditions will be required. Flexible receivers enable rapid recovery from network failures without the need for slower supervisory control layer coordination. Furthermore, autonomous receivers can be used for system performance monitoring, network diagnostic, and other surveillance applications [40]. Such dynamic networks put forward more stringent requirements on the multi-functionality and complexity of OPM modules. Conventional concepts of "DSP algorithms" are gradually evolving into dynamic parameter monitoring. All middle results in DSP are preferred to be "monitored" and then fed to the processing circuit. There are three main advantages to build such multi-parameter monitoring systems instead of conventional black-box DSP. Firstly, for any receiver in EONs, the signal source can be varied with fast optical path switching, many one-shot or quasi-one-shot DSP missions are required to be updated timely. For example, for a conventional fixed link, once the frame head is located, there is no need to operate timing synchronization twice. However, TO needs to be monitored due to burst mode path switching in EONs [41]. Other parameters that are required to be constantly monitored in EONs include modulation format, CD, FO, et. al. Secondly, by parameter monitoring rather than processing the signal in a black-box mode, the optical link path condition can be monitored and managed. For example, when the transmitter is switched to another source and abnormal parameter such as FO feature is monitored at Rx, we can timely prevent the occurrence of failure and feedback information to the control layer. Thirdly, by reconfigure the conventional DSP system to separate monitoring and processing modules, the efficiency, performance, and reconfigurability

can be improved since any suitable algorithm and processing method according to the requirement. The design principle of the DSP module for receivers in EONs is shown in Fig. 1-11. Such a principle is helpful to build a flexible and efficient receiver for EONs.

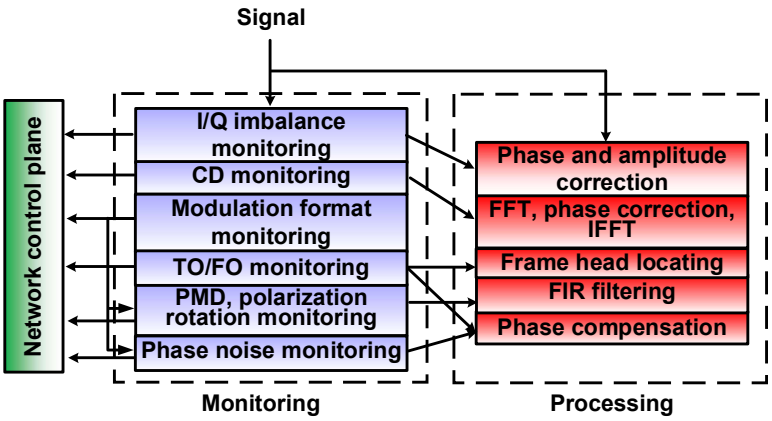

Fig. 1-11. White-box monitoring and processing based DSP structure for receivers in EONs.

In EONs, time-varying modulation format information, TO, FO and FOD need to be constantly monitored and updated for processing of the received signal which may come from any transmitter in the EONs. Among these parameters, efficient modulation format identification (MFI) is critical to reconfigure the DSP flow at the Rx [42, 43]. Generally, the existing proposed MFI schemes can be divided into three main categories. The first kind employs time-domain features of different standard QAM formats as the identification criteria [44-46]. The features include distributions or histograms of amplitude and phase etc. For PDM signals, the Stokes-space-based method and histogram of the amplitude-based method have been proposed to realized MFI. However, the complexity is high since a large number of symbols is required. Meanwhile, for high-order format under low OSNR, MFI performance degrades severely. The second type of MFI is data-aided (DA) scheme, which is realized with training symbols [47] or extra sub-carrier pilots [48]. It is more robust than the first

type and is capable of tracking fast format switching. However, the SE is sacrificed. Considering MFI for hitless flexible coherent transceiver, a blind, fast, and low-complexity MFI scheme with high accuracy even for high-order formats is worthy of further study. On the other hand, in conventional fixed coherent systems, TO and FO monitoring have been addressed well using DSP techniques. For the establishment of a communication link, TO monitoring (also known as frame synchronization) is compulsory to identify the correct temporal position of a data frame [17], which is a one-shot mission for the fixed link path. However, due to the highly dynamic feature, there are many possibilities in light path routing, burst mode communication, and channel switching for future flexible optical networks where low-latency and efficiency are of much significance [8]. Generally, existing TO monitoring methods can be divided into two categories. The first kind of TO monitoring inserts training symbols (TSs) at the Tx and calculates the timing metric based on the received signal according to the structure of TSs at the Rx. Then, the TO monitoring is realized by the identification of the maximum correlation value. For example, the classical Schmidl & Cox (S&C) algorithm sends two identical patterns consecutively and calculates the timing metric of the received signals [17]. However, due to its pulse-like timing metric, the obtained starting point may have a temporal offset of several symbols, leading to the use of more taps in the digital equalizer, for the purpose of residual TO compensation. Some research efforts have been made to modify the S&C algorithm. For example, for Minn's approach [49] and Park's approach [50], the TS structure and the corresponding timing metric are carefully designed to guarantee a sharp peak of the timing metric. It is obvious that these approaches are all operated with a sliding-

window manner in the time domain. For the S&C algorithm, the timing metric is updated using a calculation process that just removes one product of a pair of signals, and another product is added into the timing metric. Such a low-complexity updating process leads to the pulse-like timing metric. As for Minn's approach, sharp peak can be obtained but the calculation of the timing metric is more complex and its corresponding mean square error (MSE) is quite large under the condition of inter-symbol interference (ISI) channel [50]. Alternatively, in Park's approach and other proposed schemes [51, 52], the signs of time-variable are opposite during the calculation of the timing metric. Therefore, all pair products of signals need to be re-calculated for every sliding window, in order to update the timing metric. Such sliding window manner with complicated timing metric calculation results in huge complexity in practice especially for a received signal with a long length. Therefore, the research community is faced with a dilemma in high accuracy of TO monitoring and low implementation complexity. The second type of TO monitoring is operated by calculating the cross-correlation of the known TSs and the received symbols [53]. This method can be employed well in the DD system. The calculation complexity of such a method can be reduced by replacing the computation of sliding correlation in the time domain with the alternative in the frequency domain because convolution in the time domain is equivalent to multiplication in the frequency domain. Unfortunately, for digital coherent detection, such an approach can only be operated under the condition of the residual frequency offset (FO) of less than approximately 10 MHz [53]. FO occurs when independent lasers are used for the transmitter and the LO, respectively. Although one can first estimate the FO and compensate it before the timing

synchronization. However, the realization of blind FO estimation (FOE) is still challenging for various modulation formats. For example, the most popular FOE method based on FFT is not suitable for non-rectangular formats, if the FFT size is limited, such as 32QAM [54] and probabilistic-shaped (PS) constellations with high shaping factor [55]. FFT-FOE has an estimation range of [-symbol rate/8, +symbol rate /8] for M-ary QAM [54]. Since the commercially available lasers usually have a frequency accuracy within ±2.5 GHz over the lifetime, the FO in practical optical coherent receivers can be as high as [−5 GHz, +5 GHz] [14], which may exceed the estimation range of FFT-FOE with a symbol rate lower than 40 Gbaud. Meanwhile, the complexity of FFT-FOE is severely enhanced with respect to the FFT size. Since TSs for TO monitoring are compulsory for the digital communication system, FO monitoring is preferred to be realized simultaneously with the use of TSs. Overall, a low-complexity and accurate TO/FO monitoring scheme over a wide FO range is worthy of study, especially in future EONs. Another parameter that needs to be monitored in EON is FO drift (FOD) since there can be arbitrary combinations of LO and transmitter laser. For lasers used for coherent systems, the wavelength approximately stabilizes on a tuned value. Unfortunately, due to fast-switching optical path link as well as aging, variation of temperature and vibration, etc., the FO suffers fluctuations and drifting in practical systems especially in EONs [56]. Such frequency drift leads to time-varying FO [57], which is called FOD. Therefore, the value of FO should be timely updated to guarantee optimum system performance. Besides FFT-FOE, some low-complexity FOEs are proposed to reduce the complexity of a single estimation [58]. However, continuous operation of FOE still results in huge energy

consumption. There is no guidance on how often FFT-FOE should be operated. This problem should be addressed to enable performance optimization and complexity reduction of FOE. In EONs, FOD monitoring is even more important since the fluctuation of FO will be larger and sometimes changed in burst mode. An efficient FOD monitoring scheme is compulsory to guarantee performance and keep low complexity for receivers in EONs.

Finally, for QoT estimation in next-generation flexible optical networks, the most popular GN model based on numerical integration typically requires a computation time of a few minutes per WDM channel (tested on a personal computer with intel CORE i7-8550U CPU) [28, 33], accumulating to a few hours for full WDM systems consisting of several hundred channels. Incoherent GN (IGN) and local white noise (LWN) assumptions of the NLI are common approximations to reduce the computation efforts with a reasonable accuracy penalty. However, such time frames may still be too long for real-time network applications in EONs and closed-form approximations that can complete QoT estimations essentially in real-time are required [36]. Although some of the closed-form approximations offer comparable accuracy with numerical integration under some limitations, estimation accuracy for heterogenous links and WDM channels with nonrectangular spectral shape and Nyquist-WDM configurations still needs to be improved [36]. Another shortcoming of analytical model-based performance prediction is that the uncertainties of link parameters, e.g., inaccurate measurement of optical power, span length, loss and CD parameters, and particularly the NF of each EDFA and electrical nonidealities at the transmitter and receiver, might lead to further inaccuracies in QoT estimation [59–61]. ML-based QoT estimation

methods have the potential to overcome the limit of the analytical model by model training using a large dataset, whose costs are significant in practical optical networks. While both analytical model-based and ML-based QoT estimation tools are increasingly being considered in optical networks, there are a number of issues yet to be addressed: (a) The uncertainties of link parameters are common in deployed links and greatly affect the accuracy of analytical models. Simple and effective methods to mitigate such effects need to be developed; (b) It is not clear how the QoT estimation accuracy of ML-based methods compares with that of traditional well-established analytical model-based approach. To maximize the transmission capacity of optical networks, the reduction of operating margins is important, and it partially depends on the accuracy of the QoT estimation tool; (c) In principle, any ML-based QoT estimator is tailored for the link configuration where data is obtained and is not guaranteed to perform well in other links of a network, thus requiring time-consuming retraining and/or data recollection. Therefore, it remains to be seen how the ML models can flexibly adapt themselves to estimate QoT in practical heterogeneous networks with different transmission link scenarios with minimal efforts; (d) As QoT estimation needs to be constantly performed in practical optical networks, the stability of ML-based QoT estimation approach over long periods of time needs to be studied and compared with that of GN-model based approaches. A comprehensive comparison between both models is required before application in practice.

1.5 Research Objectives and Organization of the Thesis

Aimed at the above problems, the research objectives of this thesis are focused on: 1) A high-accuracy and low-complexity multi-parameter monitoring scheme for next-

generation flexible optical networks. 2) A joint linear and nonlinear noise monitoring technique for optical transmission systems with Kerr nonlinearities. 3) A comprehensive comparison of analytical model-based and ML model-based QoT estimation schemes for low-margin and dynamic optical networks.

In Chapter 1, an overview of the background and motivation of the thesis are provided. Firstly, the fundamental of coherent optical fiber communication systems including system architecture, impairments, and classical DSP modules are introduced briefly. Next, existing OPM and QoT estimation techniques are reviewed and their limitation for next-generation optical transmission systems and networks are discussed. The objectives and organizations of this thesis are summarized at last.

In Chapter 2, sparse fast Fourier transform (S-FFT) assisted high-accuracy and low-complexity multi-parameter monitoring techniques for flexible optical networks are discussed and demonstrated. They can be used to monitor modulation format, TO, FO and FOD. Specifically, a blind and fast MFI scheme is proposed with high identification accuracy at low OSNR by first raising the signal to the 4^{th} power and calculate the peak-to-average power ratio (PAPR) of the corresponding spectra to identify QPSK, 16, 32, and 64QAM. Then, an accurate and low-complexity TO/FO monitoring scheme based on S-FFT is discussed which consists of coarse timing/frequency synchronization, fine timing synchronization, and fine frequency synchronization. The total computation complexity is reduced by nearly 200 times in comparison with that using conventional sliding window correlation scheme. At last, an S-FFT-based FOD monitoring scheme is further discussed, by which the optimum performance and the minimum hardware cost of FOE are achieved simultaneously.

In Chapter 3, a modulation-format-transparent, accurate joint linear and nonlinear noise monitoring scheme based on the calculation of correlation between two spectral components at the upper and lower sideband of the signal spectrum is discussed and demonstrated. Different characteristics of flat linear noise spectrum and non-flat nonlinear noise spectrum are used to distinguish the influences on the correlation value from both noise sources. Both simulation and experiment are conducted to verify the performance of the proposed joint linear and nonlinear noise monitoring scheme.

In Chapter 4, a comprehensive comparative study of QoT estimation for WDM systems using ANN-based ML models and GN model-based analytical models is conducted. To obtain the best performance for comparison, all the system parameters for GN-based models in a brute-force manner are optimized. For ML models, the number of neurons, activation function, and the number of layers are optimized. The accuracies of both schemes in simulation and experiments are discussed and compared. Meanwhile, the stability and generalizability of the two schemes are compared for practical systems. Potential network capacity gains resulting from improved QoT estimators and reduced operating margins are also briefly studied.

In Chapter 5, the works presented in this thesis are summarized and future directions of research are discussed.

Chapter 2
High-Accuracy and Low-Complexity Multi-Parameter Monitoring Techniques for Flexible Optical Networks

In this Chapter, assisted by sparse fast Fourier transform (S-FFT), high-accuracy and low-complexity multi-parameter monitoring techniques for flexible optical networks are proposed to monitor modulation format, TO, FO and FOD. The monitoring principles of each parameter are explained in detail. Through simulation, the optimization processes of these monitoring schemes are shown and discussed. Experimental study is further conducted to verify the performance of the proposed schemes. Finally, a complexity analysis of the proposed schemes is provided.

2.1 Introduction

To accommodate increasingly heterogeneous traffic and better adapt transmissions to real-time link conditions such as environmental change, aging, etc, current fixed optical networks are expected to evolve to future flexible and adaptive optical networks. Such optical transmission systems and networks require large capacity, low latency, and high flexibility. High-accuracy and low-complexity multi-parameter monitoring technique plays an important role for the flexible transceivers which is expected to improve the total capacity and reduce energy consumption. Among the parameters, modulation format information of the received signal allows fast switching according to current link margin and traffic requirements without the transmission interruption [43]. Therefore, the modulation format information needs to be monitored constantly. In this connection, efficient modulation format identification (MFI) is critical to reconfigure the DSP flow at the Rx [40]. As analyzed in Chapter 1, existing MFI schemes do not have adequate performance at low OSNRs unless data-aided (DA) schemes are employed, which sacrifice the SE. TO monitoring is essential for the establishment of a communication link, identifying the correct temporal position of a data frame [17]. Since there are many possibilities in light path routing, burst mode communication, and channel switching for future flexible optical networks, efficient and low-latency TO monitoring is very important. However, as analyzed in Chapter 1, the research community is faced with the challenge of realizing highly accurate timing synchronization and low implementation complexity simultaneously. FO monitoring is required to compensate FO. However, the most popular FFT-FOE scheme is not only unsuitable for non-rectangular formats, but also with limited FOE range and high

complexity. Moreover, since for lasers used for coherent systems, although the wavelength approximately stabilizes on a tuned value, unfortunately, due to fast switching of optical path as well as aging, variation of temperature and vibration, etc., the frequencies of lasers suffer fluctuations in practical systems. Such FO drift (FOD) leads to time-varying FO. Therefore, the estimated value of FO should be timely updated to guarantee optimum system performance. However, continuous operation of FOE will result in huge energy consumption. There is no guidance on how often FFT-FOE should be operated. This problem should be addressed to enable performance optimization and complexity reduction of FOE.

Facing the above problems, high-accuracy and low-complexity multi-parameter monitoring techniques for flexible optical networks assisted by sparse fast Fourier transform (S-FFT) are proposed to monitor modulation format, TO, FO and FOD. Firstly, a blind and efficient MFI scheme that supports QPSK, 16QAM, 32QAM, and 64QAM formats and operates in the frequency domain is proposed. Different constellation partition schemes are applied to the received signals followed by 4^{th} power operation. The peak-to-average power ratio (PAPR) of the spectra is calculated to determine the occurrence of a peak, which is taken as the criteria to distinguish different formats. The process is repeated in a sequential manner to identify all the formats. After the FO pre-compensation, the spectra can be calculated using the S-FFT [62, 63], leading to a substantial reduction of the total complexity. Both simulations and experiments are carried out to investigate the performance of the proposed MFI in 28 Gbaud PDM back-to-back (B2B) and up to 1500 km SSMF transmission system. High identification accuracy for QPSK, 16/32/64QAM are obtained even when the

OSNR is lower than the value required for the 20% forward error correction (FEC) of $BER=2\times10^{-2}$ for each format. The impact of the sparsity in S-FFT is also studied. The proposed MFI shows better performance than the existing MFIs based on Stokes-space [44] and power distribution [46]. A hitless flexible coherent transceiver with fast format switching between 64QAM-32QAM and 32QAM-16QAM for B2B and over 900 km SSMF transmission are demonstrated, respectively. Assisted by the proposed MFI, the length of the switching-block is shortened to 1024 symbols. Finally, the analysis of computational complexity to realize the MFI is presented. Secondly, based on the idea of S-FFT, the full advantages of the sparse nature of TSs are explored and an efficient TO/FO monitoring scheme for fiber optical coherent transmission system is proposed. After sweeping the FO to the TSs and aliasing the received signal, S-FFT is used to calculate the correlation between them rather than conventional operation in the time domain. The total computational complexity can be substantially reduced. Then, benefited from the optimized structure of TSs, the fine timing synchronization and fine frequency synchronization are also implemented without too much additional complexity. High accuracy of timing synchronization is achieved even at very low SNR. Moreover, the complete FOE range of [-symbol rate/2, +symbol rate/2] can be realized. The effectiveness and feasibility of the proposed scheme are numerically and experimentally verified through 10 Gbaud PDM 16/32QAM signals fiber optical coherent transmission under scenarios of both B2B and SSMF transmission. Finally, an S-FFT-based robust and ultra-low-complexity FOD monitoring scheme is proposed to provide guidance to the DSP module about whether it needs to conduct FOE again or not, avoiding waste of hardware resources while ensuring system performance. A

down-sampling process is further proposed to reduce the complexity of subsequent FFT-FOE. The performance is experimentally verified with 28 Gbaud coherent systems.

2.2 Sparse-FFT-Assisted Multi-Parameter Monitoring Techniques Design

S-FFT-assisted multi-parameter monitoring techniques are designed to monitor modulation format, TO, FO, and FOD for the received signal for next-generation optical transmission systems and networks. The monitoring schemes can be divided into three parts 1) Modulation format identification. 2) Timing/frequency offset synchronization. 3) Frequency offset drift monitoring. For clarity, the design principle and performance of these three parts will be introduced individually.

2.2.1 Modulation Formats Identification

2.2.1.1 Modulation format identification by spectra peak search

In the Rx DSP flow of a hitless flexible coherent transceiver, the proposed MFI is implemented after format-transparent constant modulus algorithm (CMA) based equalization. Assuming ideal clock recovery, and equalization, the received signal $r(n)$ can be expressed as [54]

$$r(n) = m(n)\exp(j(\Delta\omega nT + \theta(n))) + v(n), n = 0,1,2,\ldots \quad (2.1)$$

where $m(n)$ represents the n^{th} modulated data symbol, T is the symbol period, $\Delta\omega = 2\pi\Delta f$ is the angular FO where Δf is the FO. $\theta(n)$ is the laser phase noise, which is induced by the linewidth of the transmitter/ LO lasers and $v(n)$ is AWGN. In order

to estimate and compensate the FO, the FFT-FOE method is generally employed. For square QAM, the estimated frequency value $\Delta\hat{f}$ based on FFT-FOE is given by

$$\Delta\hat{f} = \frac{1}{4}\cdot\frac{1}{TN}\arg\max_{k,|k|\le N/2}\left|R_4(f)\right| = \frac{1}{4}\cdot\frac{1}{TN}\arg\max_{k,|k|\le N/2}\left|\sum_{n=0}^{N-1} r^4(n)e^{-j\frac{2\pi nk}{N}}\right| \tag{2.2}$$

where $R_4(f)$ is the spectrum of $r^4(n)$. N is the length of the signal. Eq. (2.2) leads to a process to search the intensity peak in the periodogram of $r^4(n)$, which can be implemented by FFT [54]. For QPSK signal, as shown in Fig. 2-1(a), the phases are $\left[-3\pi/4, -\pi/4, +\pi/4, +3\pi/4\right]$. By the 4th power transformation, the phase of $m(n)$ can be removed and the FO value can be obtained by locating the peak in the spectrum of $r^4(n)$. As for 16QAM or 64QAM signal, there are 2 and 4 rings of constellation points whose phases resemble the QPSK constellation (red points in Figs. 2-1(b) and 2-1(d)) and can be removed by the 4th power transformation. These points are referred as QPSK-like points for the rest of the Chapter. Among these points, four points at each corner are of the maximum amplitude. As shown in Eq. (2.2), these points make the most contribution to the peak intensity. On the other hand, the distribution of residual points is symmetrical with respect to the diagonal line with a slope equal to +1 or -1, eliminating the disturbance to the intensity peak. Therefore, FFT-FOE is still effective even though $m^4(n)$ is not constant [54].

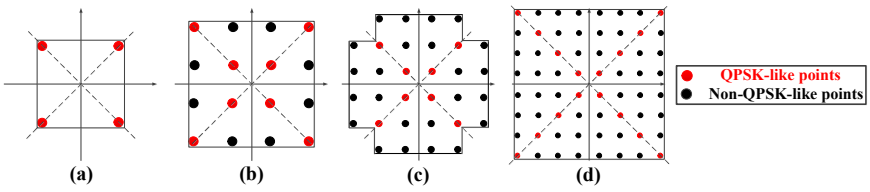

Fig. 2-1. Constellations of (a) QPSK, (b) 16QAM, (c) 32QAM, (d) 64QAM.

However, FFT-FOE is not suitable for 32QAM with a limited FFT size due to the

non-rectangular distribution of constellation points. As shown in Fig. 2-1(c), without the important contributions from QPSK-like points of maximum amplitude at four corners, the peak in the spectrum suffers from severe distortions.

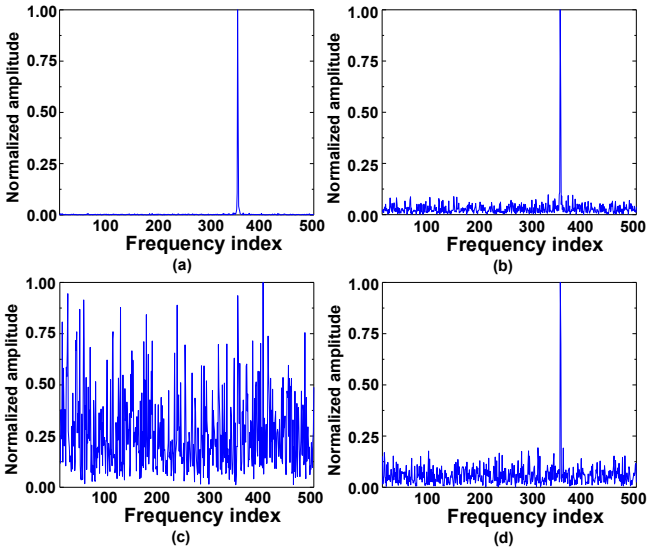

Fig. 2-2. 4th power spectra of (a) QPSK, (b) 16QAM (c) 32QAM and (d) 64QAM. OSNR is 19.3 dB with the 0.1 nm resolution. The symbol rate is 28 Gbuad. The FO is 1.4 GHz.

Figures 2-2(a)-2-2(d) show the 4th power spectra of 28 Gbaud QPSK, 16QAM, 32QAM, and 64QAM with an FFT size of 512, respectively. It is observed that there are many interference peaks in the 4th power spectrum of 32QAM, while the peak is obvious for the other three formats. Therefore, this feature can be used to distinguish 32QAM among these four formats. To realize an effective MFI scheme for a wide OSNR range in flexible optical networks, a proper criterion should be used to decide whether there is a peak or not in the spectrum. A slightly modified PAPR of $R_4(f)$ is calculated as

$$PAPR=\frac{\max\limits_{k}\left|R_4(f)\right|}{\left(\sum\limits_{k=0}^{N-1}\left|R_4(f)\right|-\max\limits_{k}\left|R_4(f)\right|\right)\Big/\left(N-1\right)} \tag{2.3}$$

Here, the peak value for the denominator is removed to avoid error induced by different FFT-size. Then the calculated PAPR is more appropriate for the decision in MFI. Figure 2-3(a) shows the PAPR for four formats within the OSNR from 5-30 dB. The PAPR of 32QAM is lower than that of other formats when the OSNR is larger than 10 dB, indicating that the peak searching by PAPR calculation can be used as the identification criteria. The PAPR threshold is set to decide whether there is a peak or not. The optimization of the threshold is presented in Section 3.1.

Next, it is necessary to distinguish between QPSK, 16QAM, and 64QAM, which all have peaks in the 4^{th} power spectrum. Inspired by the analysis above, two constellation partition schemes after CMA equalization and the power normalization are suggested. The partition scheme I is used to distinguish 64QAM from QPSK and 16QAM while the partition scheme II distinguishes 16QAM from QPSK. For the 64QAM constellation, there are 9 rings with corresponding amplitude of 0.2180, 0.4874, 0.6539, 0.7859, 0.8987, 1.0899, 1.1738, 1.3259 and 1.5258 after the power normalization. Among these rings, the 1^{st}, 3^{rd}, 6^{th}, and 9^{th} rings consist of QPSK-like points. Considering that QPSK-like points have important contributions to the FO peak, partition scheme I selects these points according to their amplitudes and sets them to zero in the calculation of the spectrum. For this step, the FFT size is decreased to 256 to enhance the impact of lost QPSK-like points. The PAPR of the corresponding spectra as a function of OSNR are shown in Fig. 2-3(b). With the help of the partition scheme I, the PAPR of the 64QAM spectrum decreases rapidly. The insets of Fig. 2-3(b) show the corresponding 4^{th} power spectra. The OSNR is 21.9 dB to reach the BER of 2×10^{-2} for 64QAM. It is observed that the spectrum of 64QAM suffers from severe

interference. On the other hand, the impact of partition scheme I on spectra of QPSK and 16QAM is minimal.

After the identification for 32QAM and 64QAM, the partition scheme II is employed to further distinguish 16QAM from QPSK. Similar to the partition scheme I, the QPSK-like points, which are located at the 1st ring and the 3rd ring in 16QAM after CMA, are selected and set to zero. Figure 2-3(c) shows the PAPR curves of the corresponding spectrum for QPSK and 16QAM with the partition scheme II. The insets of Fig. 2-3(c) show the 4th power spectra of QPSK and 16QAM when the OSNR is 16.2 dB to reach the BER of 2×10^{-2} for 16QAM and the FFT size is 512. Therefore, QPSK and 16QAM can be distinguished.

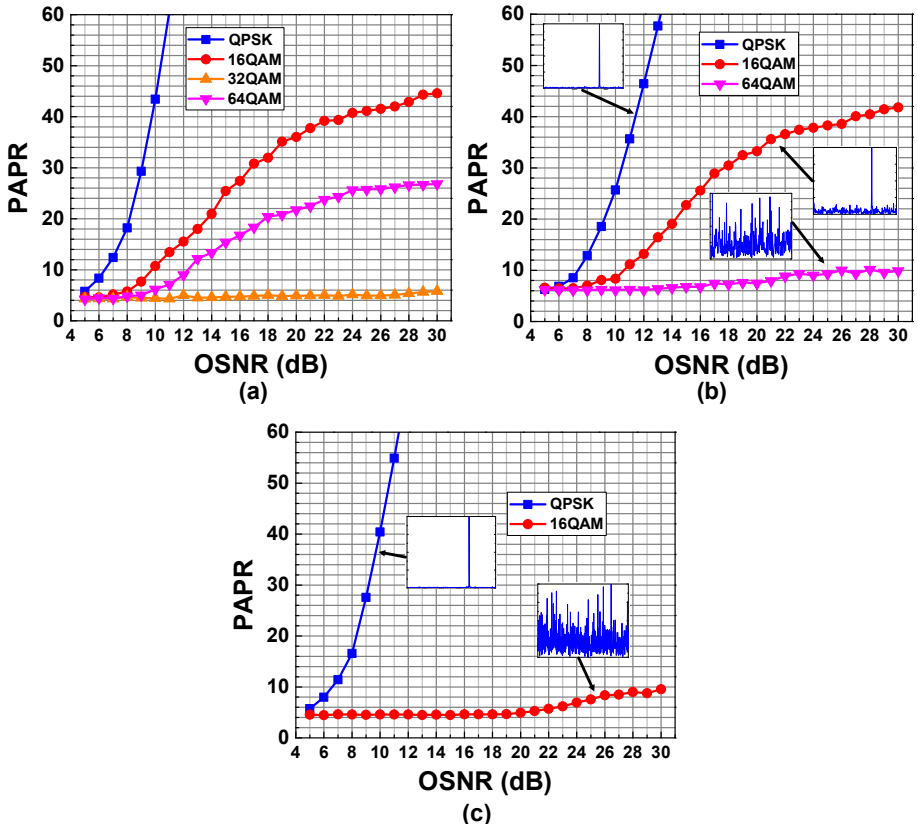

Fig. 2-3. (a) PAPR of the 4th power spectra for QPSK, 16, 32 and 64QAM. The FFT size is 512. (b) PAPR of 4th power spectra for QPSK, 16 and 64QAM, with the partition scheme I. The inserted figures are the 4th power spectra with OSNR of 21.9 dB. The FFT size is 256. (c) PAPR of the 4th

power spectra for QPSK and 16QAM, with the partition scheme II. The inserted figures are the 4th power spectra with OSNR of 16.2 dB. The FFT size is 512.

Overall, by calculating the PAPR of the 4th power spectrum with/without the partition scheme I and the partition scheme II, MFI among QPSK, 16QAM, 32QAM, and 64QAM can be realized. The decision flow chart of the proposed MFI is shown in Fig. 2-4. As it shows, the 32QAM signal can be firstly identified at step 1 without partition schemes, while the MFI for the 64QAM signal can be conducted before the partition scheme II. If a signal is 16QAM or QPSK signal, it can be recognized at the last step. It is noted that if there are more possible formats required to be identified, corresponding partition schemes should be further designed. To achieve good MFI accuracy over a wide OSNR range, the PAPR threshold of each step (Th1, Th2, Th3) should be carefully optimized. After CMA equalization, the influence of PMD is mitigated. Therefore, signals from both polarizations can be used to calculate the PAPR, enhancing the robustness of the MFI. In this Chapter, MFI for a block length of 1024 symbols from both polarizations is realized. Under the condition of no partition and partition scheme II, totally four spectrums with a length of 512 are summed up for the PAPR calculation, while for the partition scheme I, eight spectrums with a length of 256 are used.

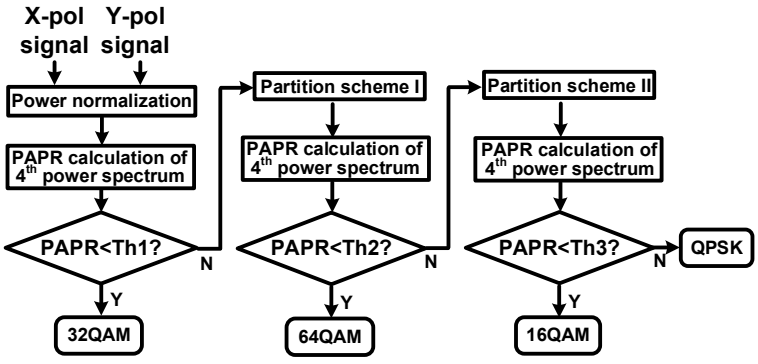

Fig. 2-4. Decision flow chart of the proposed MFI.

2.2.1.2 Low complexity spectrum and PAPR calculation assisted by S-FFT

Sparse-FFT aims to estimate the k largest (in magnitude) coefficients of the FFT of a vector x with a length of n. Consequently, the high complexity of FFT can be reduced, and a coarse spectrum can be obtained [62]. Considering that the FO spectrum has only one peak, a simple type S-FFT is employed to reduce the total complexity of MFI [63]. Firstly, a basic property of Fourier transform is introduced, which is well-known in signal processing: Aliasing a signal in the time domain is equivalent to subsampling it in the frequency domain, and vice versa. Figure 2-5 illustrates this property for the signal length of 8.

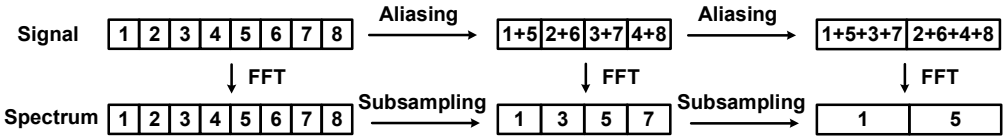

Fig. 2-5. Schematic of time domain aliasing and frequency domain subsampling.

Taking Fig. 2-5 as an example, for a signal length of $2n\times 2$ (n is an integer), the frequency components at the index of odd numbers are retained after once signal aliasing, while the even components are lost. For the retained components, their indexes in the subsampled spectrum is (i_p+1)/2, where i_p is the previous index in the spectrum before subsampling.

Based on the above analysis, it can be concluded that for the signal length of 2^n, the frequency component whose index is $2^{n-1}+1$ will never lose no matter how many times aliasing and subsampling are performed (e.g. the 5$^{\text{th}}$ frequency component in Fig. 2-5). On the other hand, for a direct current (DC) or no-FO signal with a length of 2^n, the only peak in the spectrum is right located at $2^{n-1}+1$. By taking advantage of this characteristic, the complexity of spectrum calculation can be reduced. For the proposed

MFI, three times calculations of spectrum are required for the with/without the partition scheme I and II. For the first step, it is the same as FFT-FOE and FO compensation (FOC) of the 4th power signal is performed using the estimated FO value. Then, the FO peak of the spectrum with the partition scheme I and II is located at $2^{n-1}+1$, and will always exist in the subsampled spectrum. In practice, the phase noise induced by lasers can also change the phase or even the FO of signals. Fortunately, when FFT-FOE is used to estimate the FO of the signal, the impact of phase noise has been included in the estimated FO value. Therefore, the proposed MFI scheme is insensitive to the effect of laser linewidth. Figure 2-6(a) shows the 4th power spectrum of QPSK without partition and Fig. 2-6(b) shows the 4th power spectrum of the same signal as in Fig. 2-6(a) with the FOC and partition scheme II. Figures 2-6(c)-2-6(f) depict spectra obtained by S-FFT with the subsampling rate p of 4, 16, 64, and 256, respectively, and the peak is located at 65, 17, 5, 2, respectively, which accords with the iteration relationship of (index$_p$+1)/2. Therefore, full-point FFT can be avoided in the last two steps with the partition scheme I and II. S-FFT can be used to calculate the spectrum with shorter FFT size after the signal aliasing. With this kind of S-FFT, the DC-frequency component and non-DC frequency components can be simultaneously obtained to calculate PAPR efficiently. The subsampling rate p of S-FFT should be optimized taken both the complexity and MFI performance into account.

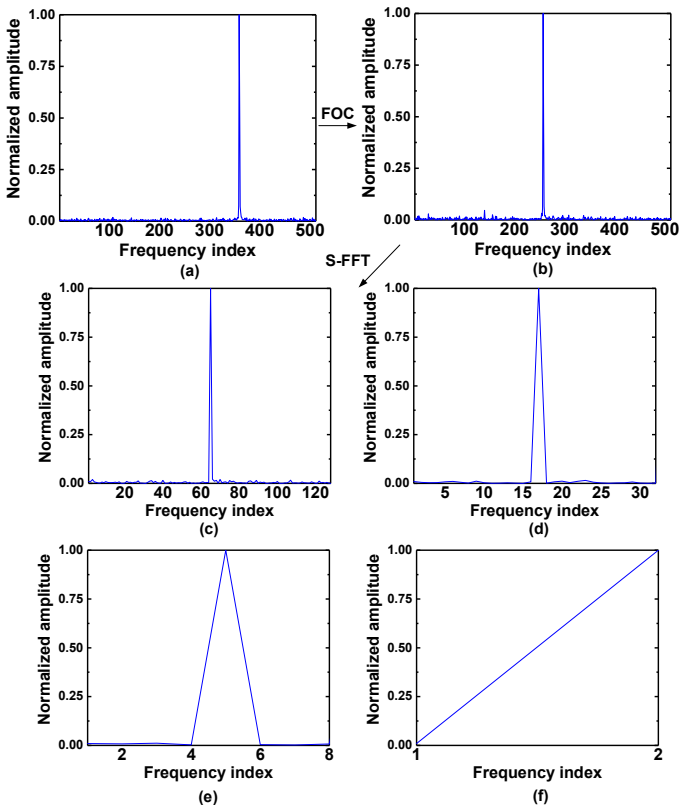

Fig. 2-6. (a) Spectra for 4th power of QPSK signals without partition, (b) Spectra of the signal in (a) with FO compensation and partition scheme II. Spectra obtained by S-FFT with the subsampling rate p of (c) 4, (d) 16, (e) 64, (f) 256. FFT size is 512. OSNR is 16.2 dB.

2.2.2 Timing and Frequency Offset Synchronization

2.2.2.1 Synchronization in the frequency domain

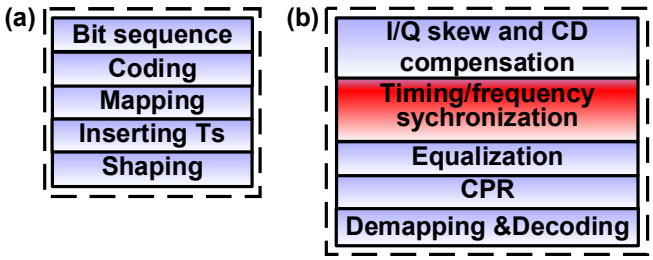

Fig. 2-7. A typical (a) Tx and (b) Rx DSP flow for coherent fiber optical single carrier transmission system.

Figures 2-7(a)-2-7(b) depict the typical DSP flows at Tx and Rx for a single-carrier fiber optical coherent transmission system, respectively. At the Tx DSP, the TSs for the time/frequency synchronization are inserted into the signal to be transmitted before

the electronic-to-optical conversion. The Rx DSP includes the compensation of I/Q skew and CD, the timing/frequency synchronization, digital equalization, CPR, and de-mapping/decoding process. If the timing synchronization is realized by calculating the cross-correlation of the known TSs and the received symbols, it can be operated in the frequency domain by FFT to reduce the computational complexity. It is well-known that time-domain convolution is equivalent to multiplication in the frequency domain. Therefore, the correlation between the received signal $r(n) = r(1), r(2), ..., r(N)$ and TSs $Ts(n) = Ts(1), Ts(2), ..., Ts(N)$ can be expressed as

$$Ts^*_{-n} \otimes r = F^{-1}\{F\{Ts\} \cdot F\{r\}\} \tag{2.4}$$

where F and F^{-1} are FFT and IFFT, respectively. $\otimes$ represents circular convolution, and Ts^*_{-n} is the time-reversed conjugated TSs.

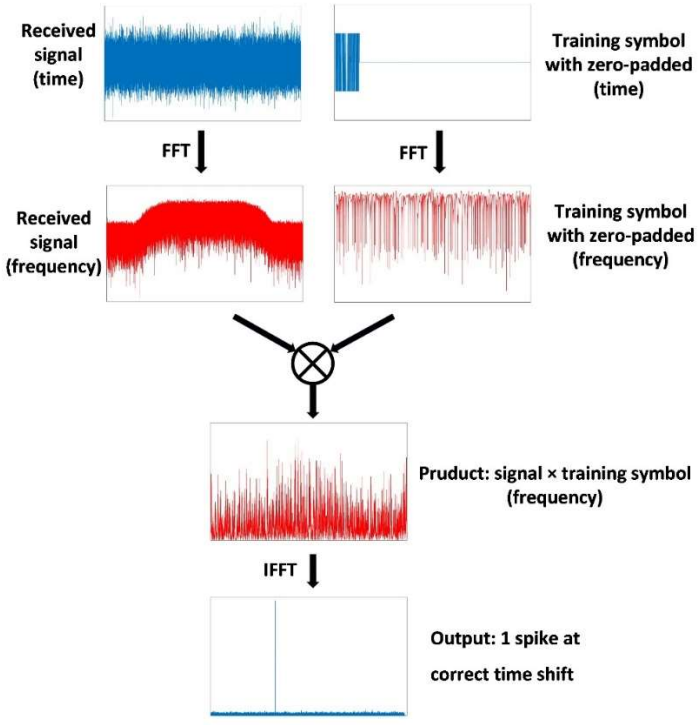

Fig. 2-8. Flow chart of timing synchronization realized in frequency domain.

Therefore, the realization of timing synchronization in the frequency domain is expressed as the following three steps, as schematically shown in Fig. 2-8. First, the FFT of the received signal and the TSs is calculated, which is zero-padded to the same length as the received signal, because the frequency domain multiplication requires two vectors having the same length. Next, the FFT results are multiplied. Finally, IFFT is performed at the output. The three-step process is mathematically equivalent to computing the sliding correlation between the received signal and the TSs in the time domain. Thus, the output of the three-step process has its maximum value at the correct time shift. With the help of FFT, the complexity of the timing synchronization can be reduced from O(N^2) to O($Nlog_2(N)$). Unfortunately, for the coherently detected signals, the correlation peak at the correct time shift will be severely degraded by the FO, because the FO can destroy the correlation between a pair of symbols by disturbing their phases. Figure 2-9 shows the FO effect on the PAPR of correlation peak at the correct time shift. The data symbols as well as TSs are both set as QPSK format, the length of TSs is 256, and the SNR is set to 15 dB. It can be observed that the PAPR can achieve about 200 or higher value when FO is smaller than 2×symbol rate/1024, indicating that the correlation peak can be easily identified for the purpose of correct timing synchronization. However, when the FO increases to 3×symbol rate/1024, the PAPR decreases rapidly, making it difficult to recognize the correlation peak. Therefore, if the timing synchronization is realized by calculating the cross-correlation of TSs and received signal for a coherent detection system, the effect of FO must be well addressed at the same time.

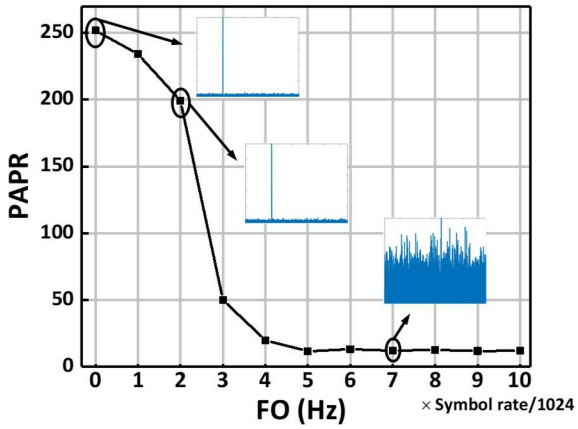

Fig. 2-9. Relationship between FO and PAPR of correlation calculation.

2.2.2.2 Operation principle of the proposed method

The schematic of the proposed S-FFT-based time/frequency synchronization scheme is shown in Fig. 2-10, mainly including coarse time/frequency synchronization, fine time synchronization, and fine frequency synchronization.

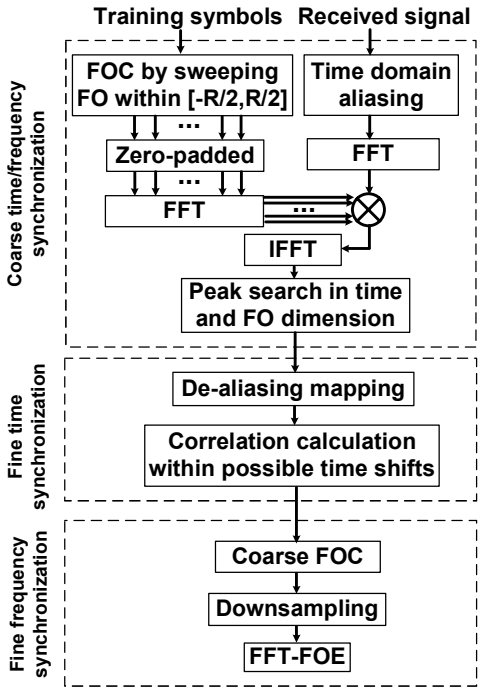

Fig. 2-10. Schematic of the propose time/frequency synchronization scheme.

A. Coarse timing/frequency synchronization

The coarse timing/frequency synchronization is realized by S-FFT. The principle of S-FFT has been introduced in Section 2.2.1.2. Here, S-FFT is used to realize the coarse timing/frequency synchronization, by making full use of the sparsity arising in the sliding correlation between the received signal and TSs. Then, the full-point FFT can be avoided with a significant reduction of total complexity during the coarse timing/frequency synchronization process. Here, the S-FFT is implemented by adding a subsampling process before the FFT-based synchronization. As shown in Fig. 2-11, aliasing a signal in the time domain is equivalent to subsampling it in the frequency domain, and vice versa. Figure 2-11 illustrates this property for a signal length of 8. Time-domain samples with the same interval are summed together into one sample. And the right part is the equivalent subsampling process in the frequency domain [63].

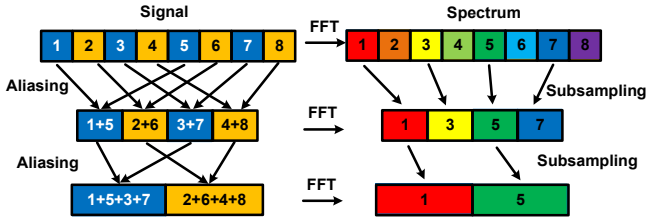

Fig. 2-11. Schematic of time domain aliasing and frequency domain subsampling.

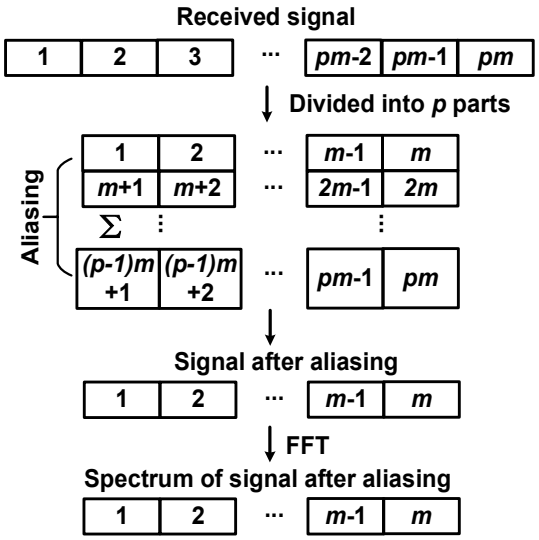

Fig. 2-12. Signal aliasing of a typical time series with length *pm*.

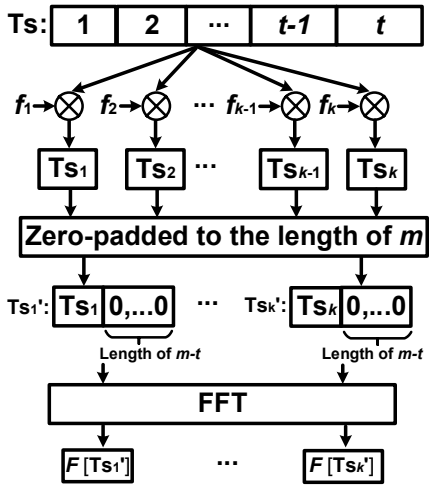

Fig. 2-13. FO sweeping and zero-padding process of training symbols.

Based on such property, the received signal is divided into p parts with each length of m and then aliased in the time domain, in order to reduce the FFT size, as shown in Fig. 2-12. p elements of each column are added into the one-time grid to generate a new time series with a length of m. The subsampling rate is denoted as p. Meanwhile, as mentioned earlier, FO will influence the timing synchronization. Therefore, in coarse timing/frequency synchronization, before the frequency domain multiplication with the received signal, the TSs with a length of t is pre-swept by an equal frequency spacing of $R/256$, over a range of $[-R/2, +R/2]$ as shown in Fig. 2-13,

$$Ts_h(i) = Ts(i) \cdot \exp(j \cdot f_h \cdot i) \qquad h = 1, 2...k, i = 1, 2...t \tag{2.5}$$

$Ts(i)$ is the i^{th} TS symbol. f_h stands for h^{th} FO within $[-R/2, +R/2]$ with equal spacing. $Ts_h(i)$ is the TSs swept by f_h. Here, we choose the FO resolution of $R/256$ because such resolution is accurate enough to realize coarse timing synchronization correctly as shown in Fig. 2-9. Meanwhile, the length of TSs is set to 256, which enables accurate FO estimation of the fine frequency synchronization. Therefore, t and k are both 256. After the FO sweeping, all Ts_h are zero-padded to the same length of an aliased signal,

because the following multiplication requires two FFT outputs having the same length. Then, after FFT, multiplication, and IFFT operation, a 2-D sweeping of correlation values on the joint time and frequency coordinate is located. Figure 2-14 shows a typical coarse timing/frequency synchronization result with an SNR of 15 dB and the subsampling rate *p* of 8. The length of the received signal is 32768 symbols. Due to the aliasing process, the time-axis is reduced to the scale of 32768/8=4096. As it can be clearly observed that, only a single correlation peak on the joint time and frequency coordinate stands for the coarse timing and frequency synchronization result. For other combinations of time-frequency, the correlation values are much smaller than the peak value due to incorrect time aligning and FO sweeping.

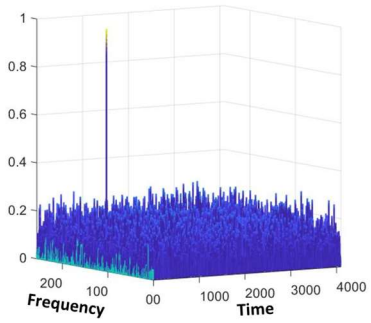

Fig. 2-14. Typical searching result of coarse time/frequency synchronization algorithm with subsampling rate of 8 at SNR of 15 dB.

B. Fine timing synchronization

After coarse synchronization, fine timing synchronization is performed to precisely determined the frame head as well as the location of TSs, which is necessary for the following fine frequency synchronization. During the coarse timing synchronization, the coarse time shift, which is actually aliased by the accurate time shift and other time shifts, is obtained. Therefore, the correlations of these possible time shifts are checked (the number is equal to the subsampling rate *p* during the aliasing process) by mapping

the coarse time shift to the de-aliasing received signal and find the maximum one, in order to determine the fine time shift. The most straightforward method is to calculate the correlation between the TSs and the segments of the received signal starting from *p* possible time shifts. Here, the structure of the TSs is optimized with two conjugated symmetric QPSK sequence, which is shown as $Ts = [\boldsymbol{A}_L \ \boldsymbol{B}_L^*]$ with a length of $2\times L=256$. $\boldsymbol{A_L}$ is a QPSK sequence with zero auto-correlation property and a length of L, $\boldsymbol{B_L}$ is symmetric with respect to $\boldsymbol{A_L}$, and $\boldsymbol{B_L}$* is the conjugated $\boldsymbol{B_L}$. Benefited from this structure, instead of calculating the correction between TSs and received signal, the timing metric between two half sequences at *p* possible time shifts for the received signal $r(n)$ is calculated

$$M(d) = \left|P(d)\right|^2 / W_1(d) * W_2(d), \quad d = 1, 2, \ldots p \tag{2.6}$$

$$P(d)=\sum_{s=0}^{L-1} r\{[co+(d-1)m]+s\} \cdot r\{[co+(d-1)m]+2L-s-1]\} \tag{2.7}$$

$W_1(d)$ and $W_2(d)$ are used to normalize the power of $\left|P(d)\right|^2$.

$$W_1(d)=\sum_{s=0}^{L-1} r\{[co+(d-1)m]+s\} \cdot r^*\{[co+(d-1)m]+s\} \tag{2.8}$$

$$W_2(d)=\sum_{s=0}^{L-1} r\{[co+(d-1)m]+2L-s-1\} \cdot r^*\{[co+(d-1)m]+2L-s-1\} \tag{2.9}$$

Here, *co* is the coarse time shift obtained from the coarse timing synchronization. Due to the conjugated symmetric design, not only a sharp peak can be ensured, but also $M(d)$ is insensitive to FO. Assuming that the suffered FO is Δf, for each $r\{[co+(d-1)m]+s)\} \cdot r\{[co+(d-1)m]+2L-s-1]\}$ in Eq. (2.7), there is a common phase factor of $\exp(2\pi \cdot (2L-1) \cdot \Delta f)$. After the absolute operation, the FO effect can

be removed. Therefore, for the fine time synchronization, pre-FO compensation is not required. Due to the use of optimized TS structure, the complexity of fine time synchronization is reduced by half, as the correlation calculation within the received signal has a complex multiplications length of L (128), while that of correlation calculation between TSs and the received signal requires a length of $2L$ (256). A typical fine time synchronization result is shown in Fig. 2-15, under the condition of p=8 and SNR=15 dB. After the combination of coarse and fine timing synchronization, the specific and accurate time shift of the TSs can be obtained.

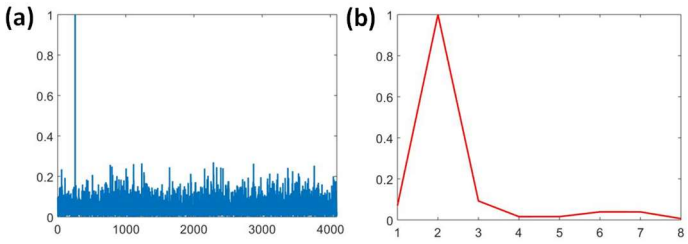

Fig. 2-15. Typical searching result of fine time synchronization algorithm with subsampling rate of 8 at SNR of 15 dB.

C. Fine frequency synchronization

While the first-stage coarse synchronization provides a coarse possible FO range, fine frequency synchronization determines the overall FOE accuracy of the proposed scheme. After the fine timing synchronization, the accurate temporal location of TSs is identified. Then, the TSs are extracted from the received signal and implement the coarse FO compensation (FOC) based on the coarse FO value obtained previously. The coarse FOC limits the possible FO range to [-R/512, +R/512]. Here, traditional FFT-FOE is used to achieve a fine resolution. For the QPSK signal, the FOE value $\Delta\hat{f}$ based on FFT-FOE is given by

$$\Delta\hat{f} = \frac{1}{4}\cdot\frac{1}{TN}\arg\max_{k,|k|\le N/2}\left|F_4(f)\right| = \frac{1}{4}\cdot\frac{1}{TN}\arg\max_{k,|k|\le N/2}\left|\sum_{n=0}^{N-1} r^4(n)e^{-j\frac{2\pi nk}{N}}\right| \tag{2.10}$$

where $F_4(f)$ is the spectrum of $r^4(n)$. N is the length of the signal. Eq. (2.10) is used to search the intensity peak in the periodogram of $r^4(n)$, which can be implemented by FFT [54]. Due to the 4th power transformation, the FOE range of FFT-FOE is [-R/8, +R/8] and the resolution is R/(4N). Generally, more FFT points are helpful to realize a fine FOE resolution. However, since the possible FO range is limited to [-R/512, +R/512], a down-sampling process is applied for the reduction of the FFT size. The down-sampling process is equivalent to the reduction of the FOE range of FFT-FOE, while the resolution remains unchanged because of the simultaneous reduction of FFT size and FOE range. If a signal is down-sampled with a down-sampling rate of q, the FOE range is reduced from [-R/8, +R/8] to [-R/(8q), +R/(8q)]. Please note that the down-sampling rate q should satisfy the relationship of $R/(8q) > R/512$, because the FOE range needs to be large enough in order to satisfy the resolution during the coarse frequency synchronization. Then, q is set to 32, and the FFT size of FFT-FOE is reduced from 256 to 8, leading to ultra-low computation complexity of the fine frequency synchronization. Meanwhile, the FOE resolution is maintained as R/(256×4), which is the resolution of conventional FFT-FOE with an FFT size of 256.

2.2.3 Frequency Offset Drifting Monitoring

Before application of the proposed FOD monitoring scheme, a relatively accurate FOE value is needed which can be obtained by any FOE scheme, e.g. FFT-FOE, or phase increment-based scheme. The obtained FOE value is used to compensate the FO of the

received signal. For square QAM, the estimated FO value $\Delta\hat{f}$ based on FFT-FOE is given by

$$\Delta\hat{f} = \frac{1}{4}\cdot\frac{1}{TN}\arg\max_{k,|k|\le N/2}\left|\sum_{m=0}^{N-1} r^4(m)e^{-j\frac{2\pi mk}{N}}\right| \tag{2.11}$$

where $r(m)$ is the received signal with a length of N. T is the symbol duration. Eq. (2.11) leads to a process to search the intensity peak in the spectrum of $r^4(m)$, which can be implemented by FFT. Figure 2-16(a) shows the 4th power spectrum of 28 Gbaud QPSK signal with FO of 1.4 GHz and Fig. 2-16(b) shows the 4th power spectrum of the same signal as in Fig. 2-16(a) with FOC. As observed, after FOC, the FO peak moves to the center of the spectrum. According to the definition of FFT, for a signal with a length of 2^n, the central component is at the location with the index of $2^{n-1}+1$. However, when FO drifts and exceeds half of the resolution of FFT-FOE, the location of FO peak in the spectrum of the signal after FOC will be off-center if the previously estimated FO value is still used. Using this property, S-FFT is employed to realize FOD monitoring. For a vector, S-FFT aims to estimate several largest (in magnitude) coefficients of its frequency components [62]. Consequently, the high complexity of FFT can be avoided, and a coarse spectrum is obtained. Considering that the spectrum has only one FO peak, a simple type of S-FFT [63] can be used here whose principle has been introduced in Section 2.2.1.2. By taking advantage of the characteristic that aliasing a signal in the time domain is equivalent to subsampling it in the frequency domain, and vice versa., an efficient FOD monitoring scheme can be realized by aliasing the 4th power of signal after FOC to only two points and FFT operation. If the value of FOD does not exceed half of the resolution of FFT-FOE, in the 2-point spectrum, the peak is retained and located at the second index.

Otherwise, the peak will be lost. Therefore, the monitoring resolution of FOD can be calculated as $[R/(4N)]/2$.

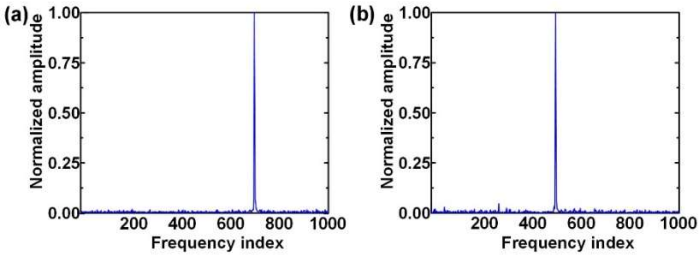

Fig. 2-16. (a) Spectrum of 4th power of QPSK signals with FO of 1.4 GHz, (b) Spectrum of the signal in (a) with FO compensation. The FFT size is 1024. SNR is 16 dB. Symbol rate is 28 Gbaud.

Setting the block size for FOD monitoring to 256 and R to 28 GHz, Figure 2-17(a) shows the full-point and sparse (2-point) spectrum in the condition that the FOD value is less than half of the resolution of 28 GHz/(4*256*2)=13.7 MHz, while the condition in which FOD value exceeds 13.7 MHz (set to 27.4 MHz) is shown in Fig. 2-17(b). The red dotted line is the centerline. Once the absolute FOD value exceeds 13.7 MHz, the FO peak is lost in the sparse spectrum. For the non-peak component at the index of 1, the amplitude is random white noise-like and is much smaller than that of the FO peak. Therefore, the ratio between amplitude at index of 2 and 1 ($R_{21}=A_2/A_1$, where A_2 and A_1 are the amplitude at the index of 2 and 1 in the sparse spectrum) can be used to decide whether there is a peak or not with a threshold (TH), and it can judge whether the FO drift exceeds the monitoring resolution. The relationship between R_{21} and SNR for QPSK, 16, and 64QAM in the condition of complete and incomplete FOC is shown in Fig. 2-18. The structure of FOD monitoring-assisted FFT-FOE is shown in Fig. 2-19. Assisted by FOD monitoring, FFT-FOE does not need to be operated for each received block of the signal. In contrast, the FO is re-estimated only if it is triggered by the FOD monitoring, substantially reducing power consumption.

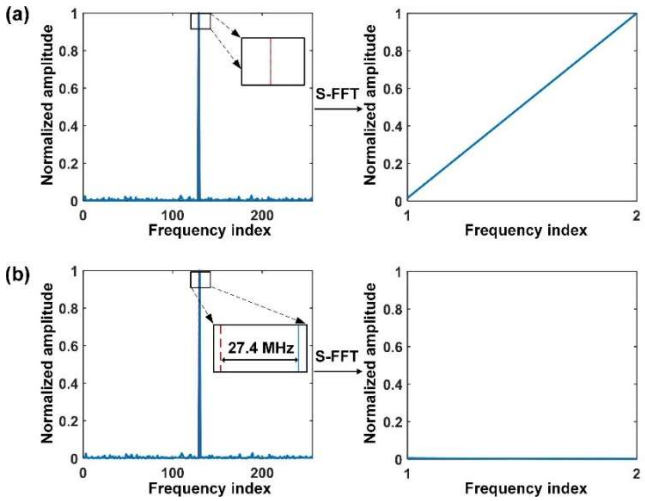

Fig. 2-17. Full-point and sparse spectrum (2-point) of 4th power of QPSK signals with (a) complete FOC and (b) FOD value of 27.4 MHz. The FFT size is 256. SNR is 16 dB. Symbol rate is 28 Gbaud.

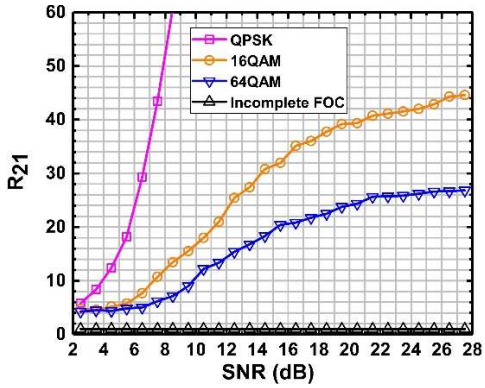

Fig. 2-18. The relationship between R21 and SNR for QPSK, 16QAM, 64QAM with complete FOC and the incomplete FOC condition.

The proposed FOD monitoring scheme is of high flexibility from two perspectives. Firstly, as analyzed above, the monitoring resolution can be adjusted by the block size N used for aliasing before 2-point FFT. The longer the N is, the more accurate the monitoring is, while it adds more operation of 4^{th} power operation and aliasing. But these required hardware resources are much less than FFT. The required resolution is determined by the format and the performance of following CPR. The higher order the format is, the lower resistance to the phase error resulted from FOD is. Meanwhile, if the algorithm in CPR is very powerful, the resolution can be reduced as CPR can correct some residual FO [64]. The second advantage of the proposed scheme on flexibility is that it can be realized in both blind and data-aided ways. For

the square QAM, i.e. QPSK, 16, and 64QAM, the signal itself can be used for FOD monitoring. Therefore, the monitoring resolution can be arbitrarily adjusted. Also, the FOD monitoring can be operated in intervals and the time interval can be set according to the frequency stability of the laser. For non-rectangular QAM, such as 32QAM, if the FFT size is limited, the FFT-FOE as well as FOD monitoring cannot work well in a blind way due to the lack of points at four corners in the constellation [64]. Instead, QPSK symbols can be inserted into the signal as assistance. Although the spectrum efficiency (SE) is sacrificed, it supports arbitrary formats.

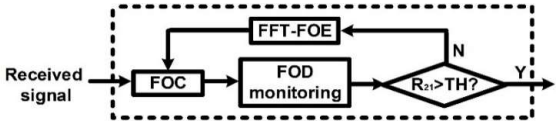

Fig. 2-19. Schematic of FOD monitoring assisted FOE scheme.

Every time an alarm is provided by FOD monitoring, the FO is re-estimated by FFT-FOE, in which the FOE range is [-R/8, +R/8] and the resolution is R/(4N). More FFT points are helpful to realize a finer FOE resolution. Initially, to obtain an accurate FO value, FFT-FOE using a signal with a long length is compulsory. However, in the condition of an alarm occurring, since the FO of the signal has been compensated using the previous FOE value, the possible residual FO range of this signal is limited. Here, the down-sampling based FFT-FOE can be applied to reduce the complexity as introduced in Section 2.2.2.2 *C*. If the down-sampling rate of q is used, the FOE range is reduced from [-R/8, +R/8] to [-R/(8q), +R/(8q)]. The down-sampling rate q shouldn't be too large because a sufficient FOE range needs to be covered. Specifically, q must at least satisfy the relationship of R/(8q)> maximum possible absolute value of residual FO. For a general laser, it is safe to set q such that the FO range of ±2×FOD monitoring resolution can be covered. Figures 2-20(a) and 2-20(b) show an example of the full point 4th power spectrum of 4096 QPSK symbols and that of signals after down-

sampling, assuming the FOD monitoring resolution is 13.7 MHz. Here, q is set to 64, and FFT size is reduced from 4096 to 64, leading to ultra-low complexity. Meanwhile, the FOE resolution is maintained as $R/(4096\times4)$, which is the resolution of conventional FFT-FOE with an FFT size of 4096. It can be seen in Fig. 2-20(b) that enough margin is still provided after down-sampling. As long as the FO doesn't suddenly drift for more than 54.7 MHz, which is the general case unless the laser is of bad quality or is severely disturbed [65], the q of 64 is pretty safe. Even if the drift speed of the laser is abnormally fast, FOD monitoring can guarantee the FO in a controllable range in combination with full-point FFT-FOE.

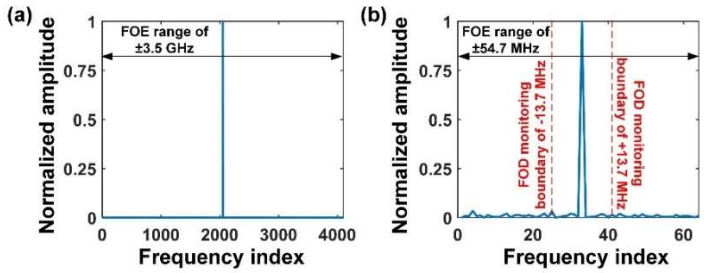

Fig. 2-20. (a) Spectrum for 4th power of 4096 QPSK symbols with no FO, (b) Spectrum of the signal in (a) after down-sampling with q of 64. SNR is 16 dB. Symbol rate is 28 Gbaud.

2.3 Simulation Study and Optimizations

Simulations are conducted to study and optimize the proposed multi-parameter monitoring techniques. The simulation results for MFI and TO/FO monitoring will be introduced individually. Since the FOD phenomenon is better to be tested in practical conditions, simulation result for FOD monitoring is not provided.

2.3.1 Simulation and optimization for S-FFT assisted MFI

2.3.1.1 The impact of threshold setting

The impact of threshold setting on the MFI accuracy is studied. The combined laser linewidth is set to 200 kHz. For the first step, threshold (Th1) should be optimized to maximize the correct identification probability of 32QAM and minimize the false alarm probability of the other three formats. Probability for one OSNR value is obtained by 2000 independent simulations. Figures 2-21(a)-2-21(d) show the correct identification probability of PDM-32QAM and the false alarm probability of PDM-QPSK/16QAM/64QAM, respectively, with the PAPR threshold setting from 7 to 12. The theoretical OSNR limit to reach $\mathrm{BER}=2\times10^{-2}$ is also plotted as a reference. As shown in Fig. 2-21(a), if the PAPR threshold is lower than 9, the correct identification probability degrades at high OSNRs because the PAPR of the 4^{th} power spectrum increases. On the other hand, we can see from Figs. 2-21(b)-2-21(d) that the false alarm events are more likely to happen when the PAPR threshold is set higher for PDM-QPSK/16QAM/64QAM. Taking this trade-off into account, 9 is chosen as the Th1 for the MFI without the use of partition scheme.

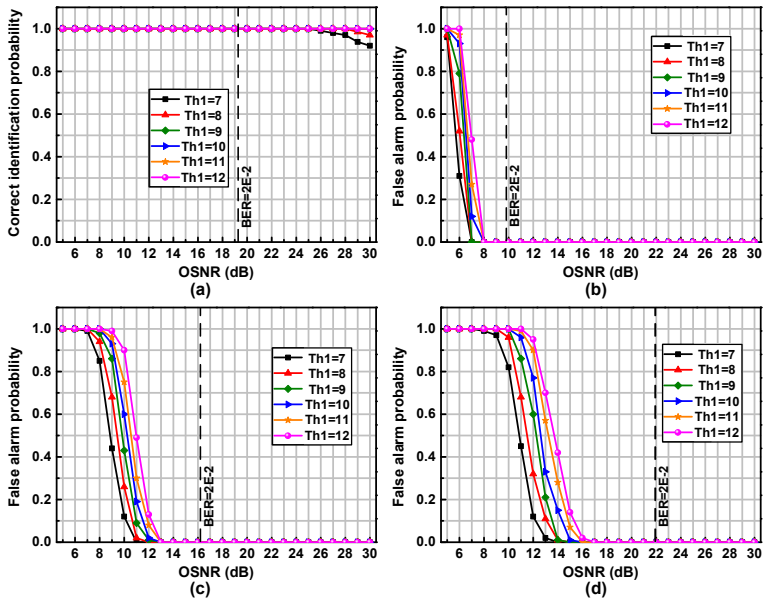

Fig. 2-21. (a) Correct identification probability of PDM-32QAM, (b)-(d) the false alarm probability of PDM-QPSK, PDM-16QAM, and PDM-64QAM, respectively, without partition scheme.

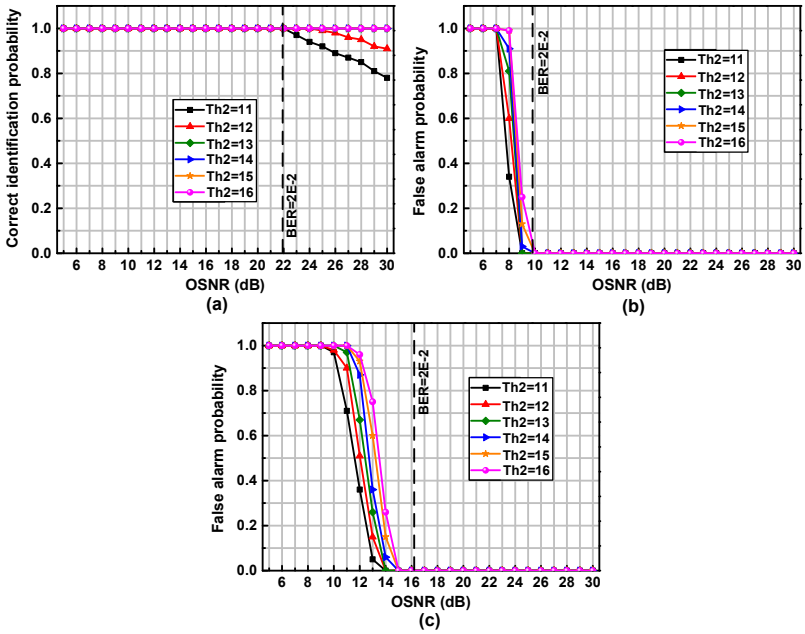

Fig. 2-22. (a) Correct identification probability of PDM-64QAM, (b)-(c) the false alarm probability of PDM-QPSK, and PDM-16QAM, respectively, with the partition scheme I.

Then, for the second step with the partition scheme I, threshold (Th2) should be optimized according to the correct identification probability of PDM-64QAM and the false alarm probability of PDM-QPSK/16QAM, as plotted in Fig. 2-22(a)-2-22(c), respectively. The principle of optimization is the same as that in the first step. The

optimal choice of the Th2 is 13. Finally, the PAPR threshold is optimized for the third (Th3) step using the partition scheme II. Figures 2-23(a)-2-23(b) show the correct identification probability of PDM-16QAM and the false alarm probability of PDM-QPSK, respectively. Similarly, 14 is chosen as the threshold for the third step. Overall, the PAPR thresholds Th1, Th2, and Th3 for 3 steps are set to 9, 13, and 14, respectively.

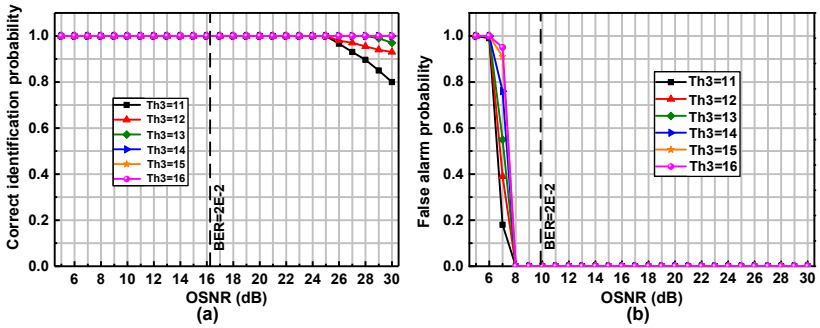

Fig. 2-23. (a) Correct identification probability of PDM-16QAM, (b) the false alarm probability of PDM-QPSK, with the partition scheme II.

2.3.1.2 The impact of subsampling rate

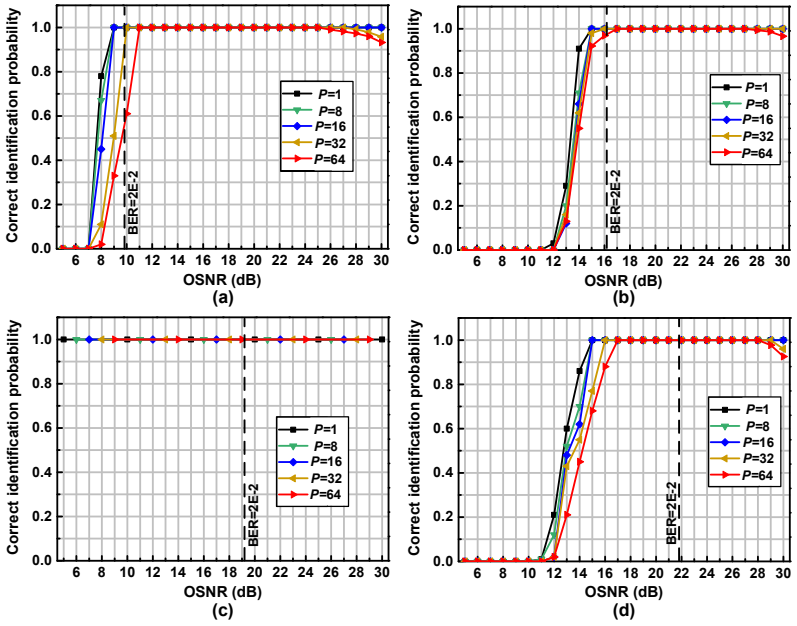

Fig. 2-24. Correct identification probability of (a) PDM-QPSK, (b) PDM-16QAM, (c) PDM-32QAM, and (d) PDM-64QAM, with different subsampling rate *p*.

As analyzed above, the spectra in step 2 and step 3 can be calculated using S-FFT. The subsampling rate p should be optimized to reduce the complexity as much as possible while maintaining the MFI accuracy. If p is high, the correction identification probability will be affected because after S-FFT, the PAPR is calculated in a smaller-size spectrum, resulting in more variance of $\left(\sum_{k=0}^{N-1}\left|R_4(f)\right|-\max_k\left|R_4(f)\right|\right)\Big/\left(N-1\right)$ in Eq. (2.3), although the peak value is unaffected. Here, with the optimal PAPR thresholds setting, Figs. 2-24(a)-2-24(d) show the correct identification probability versus OSNR for PDM-QPSK/16QAM/32QAM/64QAM with different subsampling rates. The proposed MFI can provide 100% accuracy for four formats at the OSNR lower than that required for the corresponding theoretical 20% FEC limit of $\mathrm{BER}=2\times10^{-2}$, with the p of 1 (full-point FFT). The accuracy of PDM-32QAM is not affected by the subsampling rate because it is identified at the first step where full-point FFT is necessary. When the p is 16 or lower, there is no obvious performance degradation for the other three formats. Therefore, the subsampling rate p of 16 is chosen to realize S-FFT for low-complexity MFI.

2.3.2 Simulation and optimization for S-FFT assisted TO/FO synchronization

The synchronization accuracy is numerically investigated, its dependence on the signal SNR, and the effect of the sub-sampling rate p under the condition of a single carrier 10 Gbaud PDM-QPSK transmission system. The data frame consists of TSs and normal QPSK symbols. The length of TSs is 256. ASE noise loading is used to adjust the corresponding SNR.

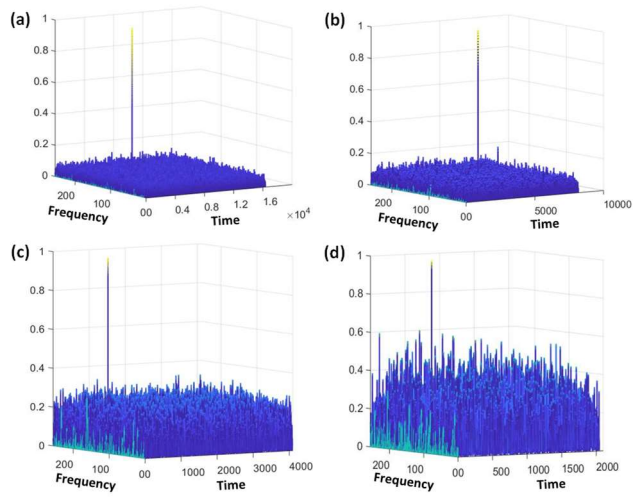

Fig. 2-25. coarse timing/frequency synchronization results with SNR of 10 dB and subsampling rate of (a) 2, (b) 4, (c) 8, and (d) 16.

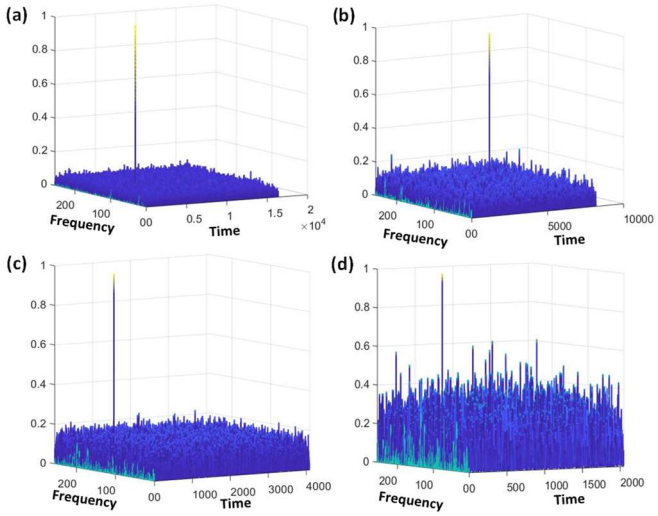

Fig. 2-26. coarse timing/frequency synchronization results with SNR of 20 dB and subsampling rate of (a) 2, (b) 4, (c) 8, and (d) 16.

Figures 2-25(a)-2-25(d) show the coarse timing/frequency synchronization results, under the condition of SNR=10 dB, with various sub-sampling rates of 2, 4, 8, and 16. Meanwhile, Figures 2-26(a)-2-26(d) show the coarse timing/frequency synchronization results, under the condition of SNR=20 dB, with various sub-sampling rates of 2, 4, 8, and 16. The side lobes rise as the subsampling rate increases, indicating degradation of synchronization performance. Thus, there still occurs a trade-off

between computation complexity and synchronization performance. Fortunately, the sharp peak is obvious, when the subsampling rate is as high as 16, leaving us enough space to reduce the complexity while ensuring the synchronization performance. To assess the timing synchronization performance, the correct detection rate (CDR) of the starting time shift of TSs where the estimated frame initial exactly coincides with the true one is counted.

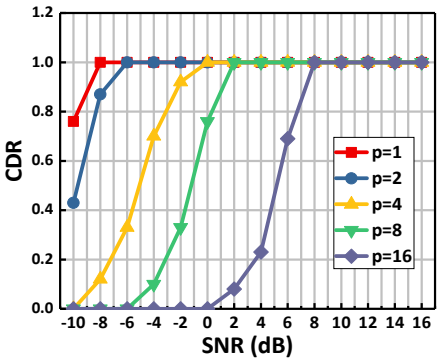

Fig. 2-27. Correct detection rate versus SNR with subsampling rates p of 1, 2, 4, 8, and 16.

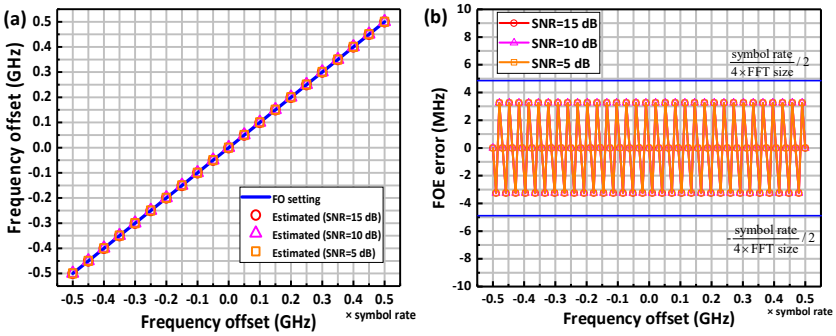

Fig. 2-28. (a) FOE Performance using the proposed scheme under various SNRs. (b) FOE error under various SNRs.

Figure 2-27 shows the relationship between the CDR and SNR under various down-sampling rates. When the SNR is high enough, CDR can reach 100% where the detection of the beginning of the frame is always correct. It is observed that the time synchronization is robust to ASE noise with the increase of p, while the complexity is low. It is found that, under the condition of p=8, CDR can achieve 100% at a very low

SNR of 2 dB. Therefore, p=8 is an optimal choice for the proposed synchronization scheme, and its value is fixed in the following discussions. The FOE performance of the proposed scheme with respect to various FOs is investigated with respect to the SNRs of 15 dB, 10 dB, and 5 dB, as shown in Fig. 2-28(a). It is clearly shown that the proposed frequency synchronization is unbiased within the range of [-R/2, +R/2], indicating that the proposed scheme is highly desirable for flexible optical networks with rapid FO variations. Figure 2-28(b) shows the FOE error under various SNRs. The proposed scheme is a kind of scanning method with a resolution the same as all FFT-based algorithms [66]. Therefore, the FOE error is cyclical with respect to the FO changes.

2.4 Experimental Verifications

Experiments are conducted to investigate the performances of the proposed multi-parameter monitoring techniques. The experimental results for MFI, TO/FO, and FOD monitoring will be introduced individually.

2.4.1 Experimental results for the S-FFT assisted MFI

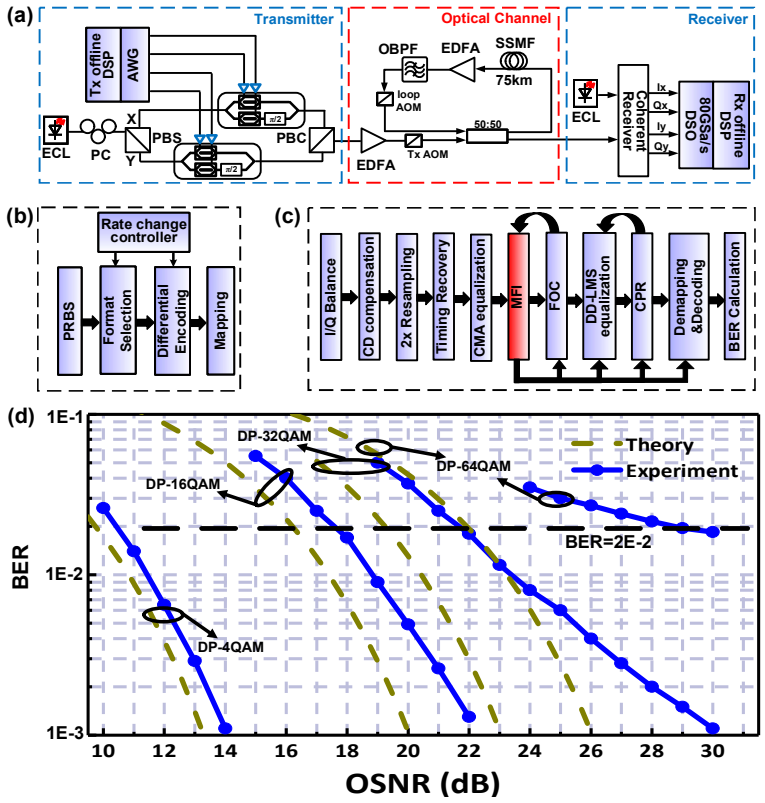

Fig. 2-29. (a) Experimental setup of hitless coherent transceiver, the offline DSP at the (b) Tx and (c) Rx. (d) measured B2B performance. (AOM: acousto-optic modulator, PBC: polarization beam combiner, PBS: polarization beam splitter, PC: polarization controller.)

To further verify the performance of the proposed MFI, experiments are conducted for a 28 Gbaud hitless flexible coherent transceiver. The setup as well as Tx/Rx DSP are shown in Fig. 2-29(a)-2-29(c). For DSP at the Tx, the hitless rate change is realized by format switching. The 28 Gbaud electrical signal is generated by an arbitrary waveform generator (AWG, Keysight M9502A) and sent to the I/Q modulator. At both Tx and Rx, 100-kHz external cavity lasers (ECLs) are used as the optical carrier and the LO, respectively. After being amplified by an EDFA, the optical signal is launched into a re-circulating fiber loop consisting of 75-km SSMF and an EDFA. An optical spectrum analyzer (OSA, YOKOGAWA AQ6370C) is employed to monitor the OSNR. At the Rx, after the coherent detection, the signal is captured and digitized by 80 GSa/s digital

sampling oscilloscope (Lecroy, Labmaster10-36Zi-A). The Rx DSP is shown in Fig. 2-29(c). After the CD compensation, downsampling, timing recovery, and CMA pre-equalization, the MFI is performed with FOC simultaneously. Please note that for 32QAM, the method in [54] is used for FOC. The obtained information is used to adjust the following DSP modules, including decision directed-least mean square (DD-LMS) based equalization bundled with blind phase search (BPS) based carrier phase recovery (CPR), and de-mapping/coding. The BER of B2B transmission is measured as a reference for performance evaluation, as shown in Fig. 2-29(d). The measured required OSNRs to reach $\mathrm{BER}=2\times10^{-2}$ are 10.4 dB, 17.5 dB, 21.7 dB, and 28.8 dB for PDM-QPSK/16QAM/32QAM/64QAM, respectively.

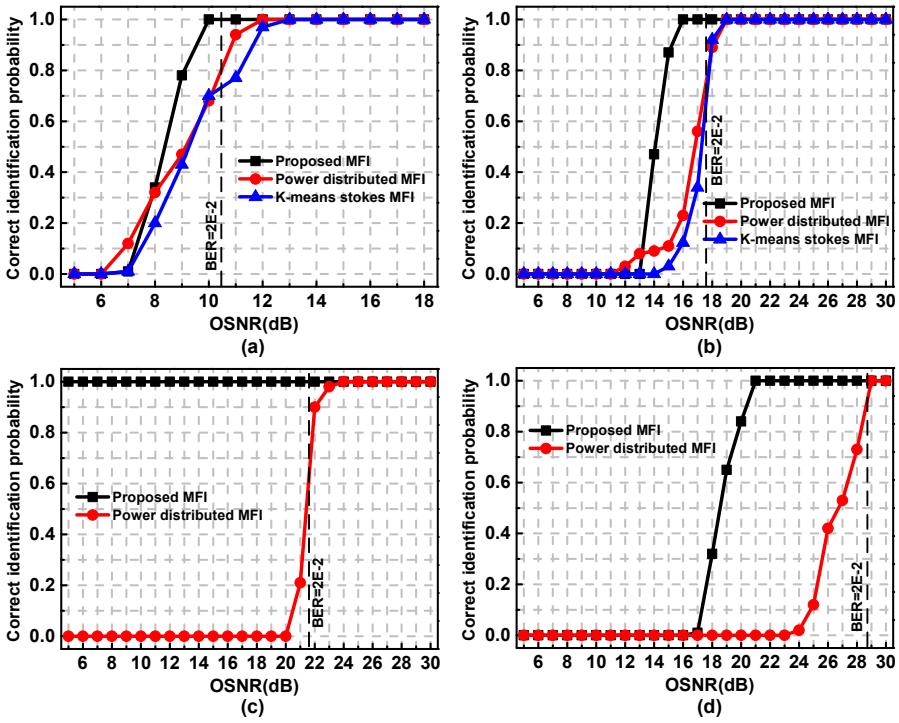

Fig. 2-30. Correct probability of MFIs versus OSNR under the scenario of B2B transmission. (a) PDM-QPSK, (b) PDM-16QAM, (c) PDM-32QAM, and (d) PDM-64QAM.

The correct identification probability of the proposed MFI is evaluated. For comparison, the performances of the k-means clustering-based Stokes MFI [44] and

the power distributed-based MFI [46] are also provided. For the proposed MFI, 1024 symbols from both polarizations are used for one identification, while for k-means clustering-based Stokes MFI, 4000 pairs of symbols are used. For the power distributed based-MFI, it requires 10000 symbols [46]. Please note that for 32/64QAM, k-means clustering-based Stokes MFI is not employed due to huge iteration times. For each case, 2000 times independent MFI are carried out to calculate the correct identification probability. As shown in Fig. 2-30, the accuracy of our proposed MFI is better than that of the other two MFIs. Specifically, 100% MFI accuracy can be achieved even though the OSNR is lower than that required to reach $\mathrm{BER}=2\times10^{-2}$ for each format using the proposed MFI. The proposed MFI outperforms the power distributed-based MFI, especially for 32 and 64QAM. The performances of the power distributed-based MFI degrade rapidly for high-order QAM, which is more easily to be disturbed by the noise. The performance of MFI after SSMF transmission is also evaluated, as shown in Fig. 2-31. The proposed MFI still remarkably outperforms other MFIs. For QPSK, three MFIs can all support over 1500 km SSMF. However, for the other three formats, the accuracies of the other two MFIs decrease dramatically, while the proposed MFI can still maintain 100% accuracy over 1500 km, 1500 km, and 825 km SSMF for 16QAM, 32QAM, and 64QAM.

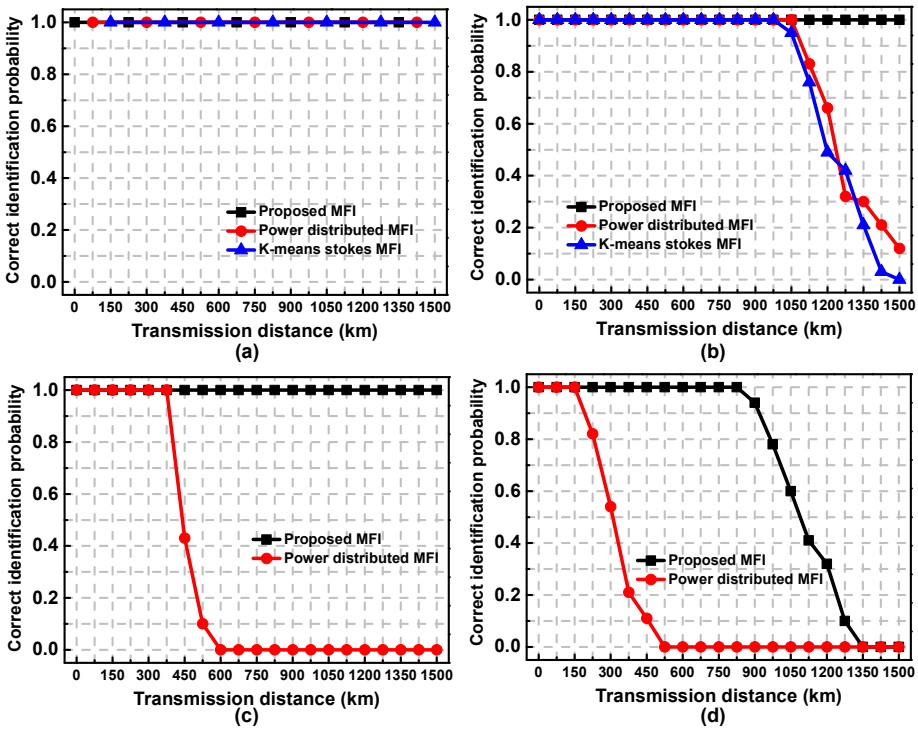

Fig. 2-31. Correct probability of MFIs versus SSMF transmission length. (a) PDM-QPSK, (b) PDM-16QAM, (c) PDM-32QAM, and (d) PDM-64QAM.

Finally, a hitless flexible coherent transceiver enabled by the proposed MFI is demonstrated with fast block-by-block format switching. Interleaved blocks are switched between PDM-16QAM and PDM-32QAM after the 900 km SSMF transmission or between PDM-32QAM and PDM-64QAM under the B2B scenario. Each block contains 2048 symbols (1024 symbols from both polarizations). As shown in Fig. 2-32, for the same format, the corresponding BERs and SNRs are stable, indicating hitless rate change can be realized by the proposed MFI. A little SNR fluctuation occurs mainly due to the limited number of symbols during the measurement.

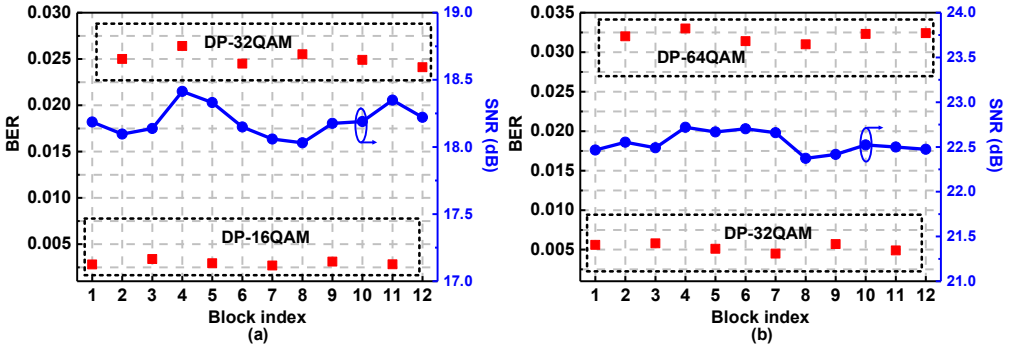

Fig. 2-32. BER and SNR versus block index for interleaved (a) PDM-16QAM and PDM-32QAM over 900 km SSMF transmission, (b) PDM-32QAM and PDM-64QAM under B2B transmission.

2.4.2 Experimental results for the S-FFT assisted TO/FO synchronization

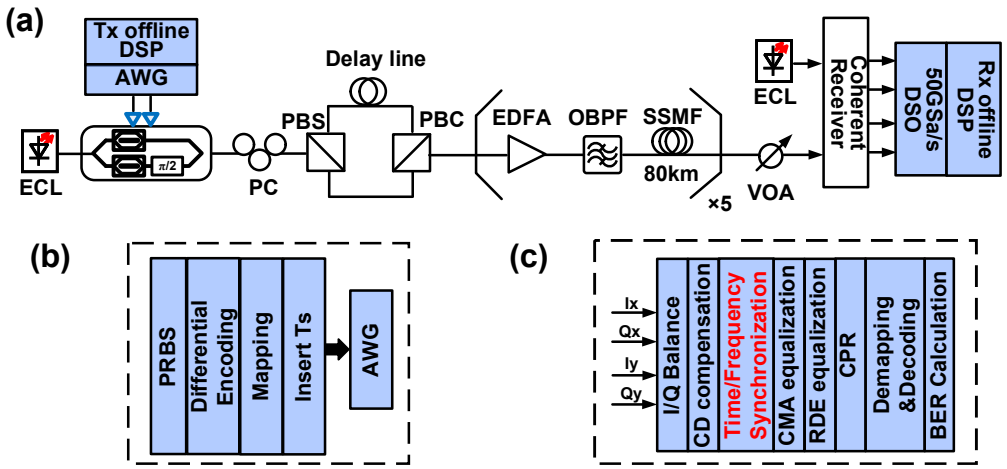

Fig. 2-33. (a) Experimental setup. (b) Tx DSP flow. (c) Rx DSP flow. (AWG: arbitrary waveform generator, EDFA: erbium doped fiber amplifier, ECL: external cavity laser, OBPF: optical band-width pass filter, PC: polarization controller, PBS: polarization beam splitter, PBC: polarization beam combiner, VOA: variable optical attenuator, DSO: digital oscilloscope.)

Experimental verification is carried out to further investigate the performance of our proposed timing/frequency synchronization scheme for 10 Gbaud PDM-16/32QAM coherent fiber optical transmission. Figure 2-33 shows the experimental setup. An ECL with ~100-kHz linewidth is used as the transmitter laser source. The AWG provides a 10 Gbaud electrical signal for both in-phase and quadrature arms of the modulator. Then, the signal is polarization division multiplexed with a 140 ns optical delay between two polarization tributaries. Then, the signal is launched into a 5 × 80 km

SSMF link with EDFA and optical bandpass filter (OBPF). The variable optical attenuator (VOA) and EDFA are deployed to adjust the OSNR of the received signal. At the Rx, ECL with ~100 kHz linewidth is used as the LO, in order to realize the coherent detection. Various FOs can be set by adjusting the central wavelength of the ECL at the Rx. The signal OSNR is monitored by OSA with a resolution of 0.1nm. Finally, the detected electrical signals are digitized and captured by a 50 GSa/s digital oscilloscope (Tektronix, DPO73304D) for subsequent offline processing. The Tx and Rx DSP flows are shown in Fig. 2-33. At the Rx, firstly, the received samples are processed with orthogonalization for I/Q imbalance compensation [15]. After the CD compensation, the proposed synchronization scheme is conducted. Then, four 15-taps fractionally-spaced (Ts/2) finite impulse response (FIR) filters arranged in butterfly structure are employed to achieve polarization division de-multiplexing and differential group delay (DGD) mitigation. These FIR filters are first adapted by the standard constant modulus algorithm (CMA) for pre-convergence. Then, the equalization is realized by switching CMA to the radius-directed equalization (RDE) algorithm. CPR based on blind phase searching is implemented before the de-mapping and decoding. BER counting is finally obtained for performance evaluation.

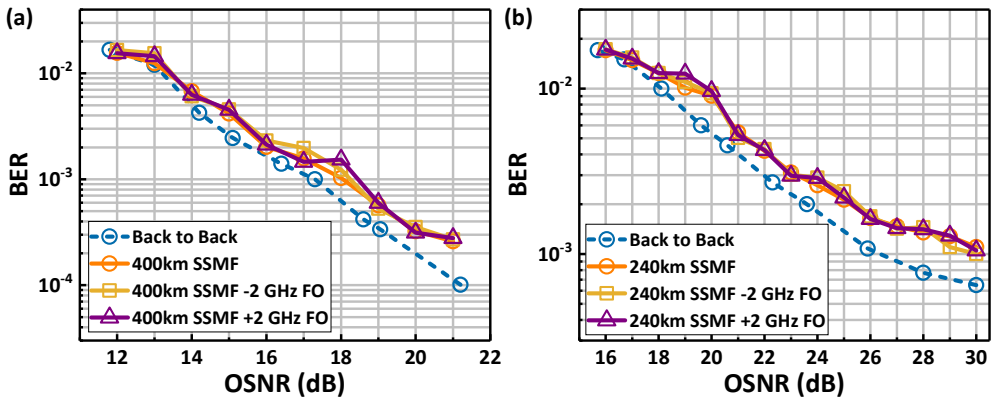

Fig. 2-34. (a) BER of PDM-16QAM with respect to the OSNR variation. (b) BER of PDM-32QAM with respect to the OSNR variation.

Figures 2-34(a)-2-34(b) show the BER performance of PDM-16/32QAM over a FO range from -2GHz to +2GHz under the B2B scenario and 400km/240km SSMF transmission. Almost the same BER performance can be observed, which means that the frequency synchronization is correctly realized. Our proposed scheme performs well even under poor OSNR values. The performance between the proposed synchronization scheme with a combination of conventional timing synchronization scheme using Park's approach [50] and FFT-FOE with an FFT size of 256 is compared.

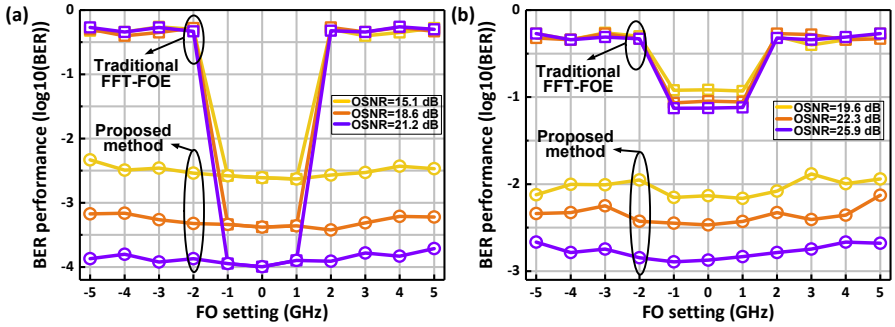

Fig. 2-35. BER vs. OSNR for (a) PDM-16QAM and (b) PDM-32QAM over a FO range from -5GHz to +5GHz.

Figures 2-35(a) and 2-35(b) show the BER performance over a FO range of [-5 GHz, + 5 GHz] for PDM-16/32QAM, respectively. The OSNRs are set to 15.1 dB, 18.6 dB and 21.2 dB for PDM-16QAM, and 19.6 dB, 22.3 dB and 25.9 dB for PDM-32QAM, respectively. It can be concluded that our proposed timing/frequency synchronization functions well under all FO conditions, due to its complete FOE range of [-*R*/2, +*R*/2]. However, for FFT-FOE, the signal is totally distorted and the BER reaches 0.5 out of the FO range of [-2 GHz, + 2 GHz]. This is mainly because its FOE range is limited to [-*R*/8, +*R*/8], which is [-1.25 GHz, 1.25 GHz] by considering the symbol rate of 10 Gbaud. Experimental results confirm that the proposed synchronization scheme has a

complete estimation range of [-5 GHz, +5 GHz], satisfying all practical application requirements. Please note that when the absolute FO value is less than 2 GHz, the performance based on FFT-FOE is terrible for PDM-32QAM signals, as shown in Fig. 2-35(b). This phenomenon is due to the non-rectangular constellation of 32QAM and many errors occur if the FFT size is limited [54]. If traditional FFT-FOE is employed in 32QAM transmission systems, the required FFT size would be too large, resulting in intolerant complexity [54]. In contrast, the TSs assisted frequency synchronization is a universal solution for arbitrary modulation formats.

2.4.3 Experimental results for S-FFT assisted FOD monitoring

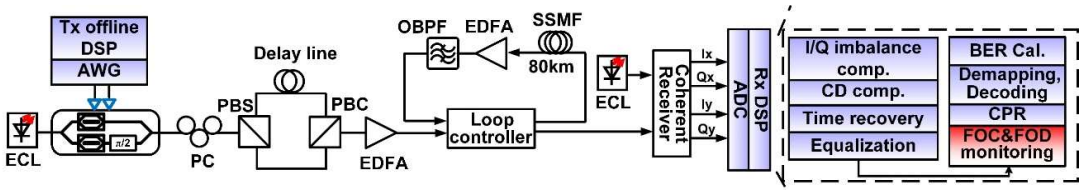

Fig. 2-36. Experimental setup. (OBPF: optical band-width pass filter, PC: polarization controller, PBS/PBC: polarization beam splitter/combiner.)

Due to the lack of accurate knowledge of the modeling of FOD phenomenon, we choose experimental verification rather than simulation. The performance of the proposed FOD monitoring scheme is experimentally studied through a 28 Gbaud coherent optical transmission system as shown in Fig. 2-36. The electrical signals are generated by an AWG and sent to the I/Q modulator. Two 100-kHz ECLs are used as the carrier and the LO, respectively. After being polarization division multiplexed and amplified by an EDFA, the optical signal is launched into a re-circulating fiber loop consisting of 80-km SSMF and an EDFA. The launch power is appropriately optimized according to transmission performance. To better illustrate the FOD phenomenon, in a single shot, a long sequence containing $4\times2.04\times10^6$ (XI, XQ, YI, YQ) samples is

sampled, which corresponds to 255.1 μs and $4\times7.1429\times10^6$ symbols, with the sampling rate of 80 GSa/s. In the Rx DSP, FFT-FOE is operated combined with the proposed FOD monitoring scheme. Here, the *N* of 256 is set for QPSK and 16QAM for FOD monitoring, resulting in the resolution of 13.7 MHz, while *N* is 512 for 64QAM for a finer resolution of 6.9 MHz. For CPR, Viterbi-Viterbi (VV) algorithm and its modified version [67] are used for QPSK and 16QAM, respectively. Bit error ratio (BER) is calculated for performance evaluation.

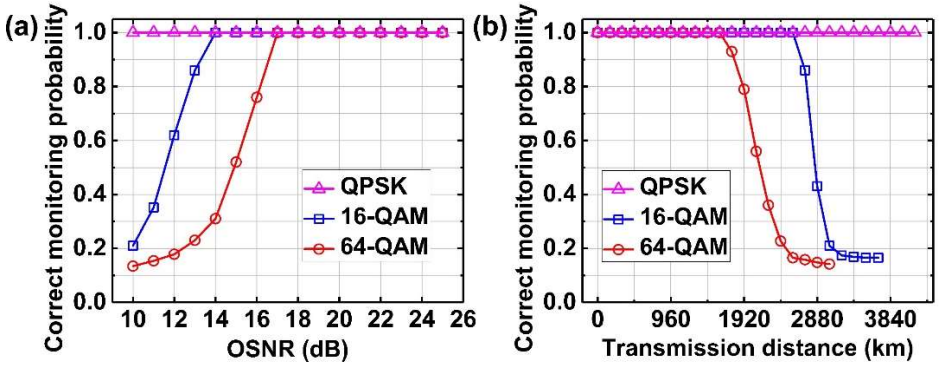

Fig. 2-37. Experimental correct monitoring probability versus (a) OSNR in back-to-back scenario and (b) transmission distance.

Figures 2-37(a)-2-37(b) show correct monitoring probability (CMP) versus OSNR in a back-to-back scenario and transmission distance, respectively. The TH should be optimized to minimize the required OSNR value to achieve 100% CMP. If TH is too large, the require OSNR value increases, while if TH is too small, in the low OSNR range, the false monitoring probability, which means that the FOD monitoring scheme mistakenly detects a FOD while there is no FOD in fact, will increase. In our experiments, TH is optimized to be 10.6. True FO value distribution over the whole signal is obtained by continuous FFT-FOE. In experiments, no wrong monitoring case is observed for QPSK, and CMP achieves 100% for 16 and 64QAM when OSNR is higher than 14 dB and 17 dB, respectively, indicating its robustness against ASE noise,

as the required OSNR for BER of 2×10^{-2} is 16.2 dB and 21.9 dB for 16 and 64QAM, respectively [68]. Meanwhile, the proposed scheme supports perfect monitoring for 16 and 64QAM transmitted over SSMF of 2560 km and 1600 km, respectively, indicating it can function well in real optical fiber transmission systems.

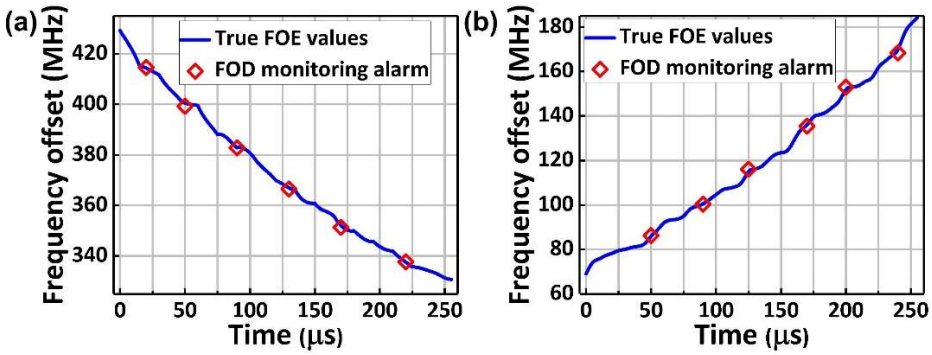

Fig. 2-38. True FO and FOD monitoring alarm versus time for (a) a case of QPSK transmitted over 4000 km SSMF and (b) a case of 16QAM transmitted over 2000 km SSMF.

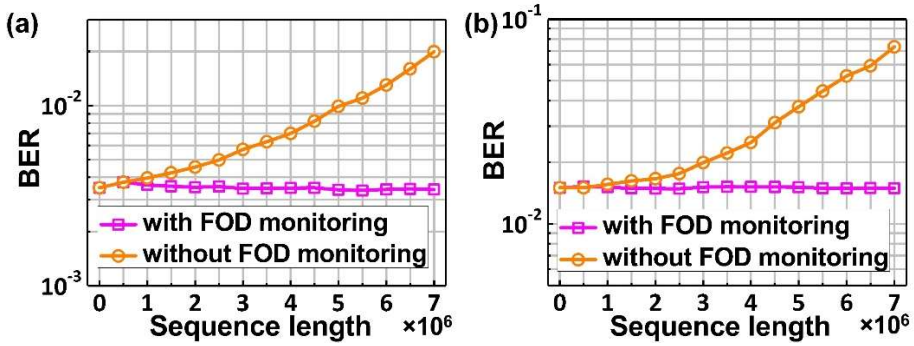

Fig. 2-39. BER versus sequence length with and without FOD monitoring for the signal in (a) Fig. 2-38(a) and (b) Fig. 2-38(b).

Next, BER with and without FOD monitoring is compared. Figures 2-38(a) and 2-38(b) depict FOD of cases of a QPSK and 16QAM signal after SSMF transmission. For these two cases, the whole FOD is more than 95 MHz and has a monotonous increasing or decreasing trend, through which it can be clearly observed the impact of FOD on system performance. Here, FOD monitoring is carried out every 10 μs. Figures 2-39(a) and 2-39(b) show BER with/without FOD monitoring of signals in Figs. 2-38(a) and 2-38(b), respectively. For the system without FOD monitoring, the overall

signal is only compensated by the FO value estimated from first the 4096 symbols. In contrast, the system with FOD monitoring estimates the FO every time an alarm occurs. Down-sampling is performed before FFT-FOE with q=64. If FOD monitoring is not included, the BER gradually deteriorates when the processed data sequence becomes longer, because the entire sequence is merely compensated by the once estimated FO and residual FO is large in the rest of the sequence. In contrast, with FOD monitoring, residual FO is controlled within a small range, avoiding BER degradation.

2.5 Complexity Analysis

2.5.1 Complexity Analysis of the S-FFT assisted MFI

Table 2-1. Complexity comparison of the proposed MFI

Step	Operation	Real multipliers	Real adders	Comparators
1	4^{th} power transform	4×512×8	4×512×2	0
	FFT	$4\times512\times\log_2512$	$4\times512\times\log_2512$	0
	Adding up spectrums	0	512×4	0
	Peak selection	0	0	512-1
	PAPR calculation	2	512-1	0
	Comparing with threshold	0	0	1
	FO compensation	4×512×4	4×512×2	0
2	Partition scheme I	2×512×4	512×4	6×512×4
	Aliasing	0	8×(16-1) ×256/16	0
	S-FFT	$8\times256/16\times\log_2(512/16)$	$8\times256/16\times\log_2(256/16)$	0
	Adding up spectrums	0	256/16×7	0
	PAPR calculation	2	256/16-1	0

	Comparing with threshold	0	0	1
3	Partition scheme II	0	0	2×512×4
	Aliasing	0	4×(16-1) ×512/16	0
	S-FFT	4×512/16× $\log_2$(512/16)	4×512/16× $\log_2$(512/16)	0
	Adding up spectrums	0	512/16×3	0
	PAPR calculation	2	512/16-1	0
	Comparing with threshold	0	0	1
Total	/	48262	35965	16897

For the practical realization of hitless flexible coherent transceiver, hardware efficiency is of great importance. As analyzed in Sections 2.1 and 2.2, the proposed MFI is based on the FFT-FOE. In a point-to-point fixed optical network, the FFT-FOE is operated in a periodic manner due to the relatively slow FO drifting. However, for flexible networks, the received signals can be transmitted from various locations with different FO. FFT-FOE should be operated for each signal block. Here, the complexity analysis of the proposed MFI is provided in Table 2-1. Conventional FFT-FOE requires 43008 real multipliers and 28160 real adders in step 1. For S-FFT-based step 2 and step 3, only 5254 additional real multipliers and 7805 additional real adders are required for the implementation of two partition schemes, S-FFT, and PAPR calculation. The proportions of additional real multipliers and adders required for the MFI are only 12.22% and 27.72% of that for compulsory FFT-FOE. Due to the use of S-FFT, the complexity of step 2 and step 3 is reduced significantly. The extra hardware cost is mainly from comparators, whose complexity is much lower than multipliers and adders. Therefore, the proposed MFI is very hardware-efficient without much additional complexity.

2.5.2 Complexity Analysis of the S-FFT assisted TO/FO synchronization

Table 2-2. Complexity analysis of the proposed synchronization scheme

Step	Real multipliers	Real adders	Comparators
Coarse timing/ frequency synchronization	44040192	40894464	1048575
Fine timing synchronization	4104	4088	7
Fine frequency synchronization	90	41	7

*Assuming the length of the received signal and training symbols is 32768 and 256, respectively. The number of FO sweeping operation is 256.

The computational complexity (CC) of DSP algorithm is critical for practical applications. The CC of our proposed timing/frequency synchronization scheme is analyzed. The CC analysis is divided into three parts. The timing synchronization which is the main source of the total CC is first considered. The FO sweeping and zero-padding process of the TSs can be completed and stored in advance, without the DSP resource occupation. Here, it is assumed that the length of the received signal and TSs are $n = 2^{15} = 32768$ and 256, respectively, while the number of FO sweeping is 256 times. For the realization of timing synchronization in the time domain, the correlation is calculated every time the window slides one symbol over the received signal. Therefore, it totally takes 256×32768×256×4+32768×256×2=8606711808 real multipliers to calculate the correlations and absolute values. Meanwhile, totally 256×32768×256×2+256×32768×(256-1)×2+32768×256×1=8581545984 real adders are also required, and 256×32768-1=8388607 comparators are necessary to identify the maximum value. If this process is realized in the frequency domain, it takes $3\times256\times32768\times\log_2 32768+32768\times256\times4+32768\times256\times2=427819008$ real multipliers, $3\times256\times32768\times\log_2 32768+32768\times256\times2+32768\times256\times1=402653184$ real adders, and

256×32768-1=8388607 comparators. It can be clearly observed that the frequency domain synchronization can substantially reduce the calculation complexity. Benefited from S-FFT with subsampling p of 8, the coarse synchronization takes $(8-1)\times 2\times 32768/8 = 57344$ real adders to alias the received signal. Then, the FFT, multiplication, IFFT, and absolution operation only require $3\times256\times(32768/8)\times\log_2(32768/8)+(32768/8)\times256\times4+(32768/8)\times256\times2=44040192$ real multipliers. Meanwhile, $3\times256\times(32768/8)\times\log_2(32768/8)+(32768/8)\times256\times2+(32768/8)\times256\times1=40894464$ adders and $256\times(32768/8)-1=1048575$ comparators are required. For the fine timing synchronization with optimized TSs structure, the complexity can be further reduced by half. Under such condition, only $(256/2)\times4\times8+8\times2=4104$ real multipliers, $(256/2)\times2\times8+(256/2-1)\times8+8=4088$ real adders, and 7 comparators are required. For the last fine frequency synchronization, the 4^{th} power transformation and FFT is operated with only 8 symbols after the down-sampling process. Here, the number of real multipliers, real adders, and comparators are $8\times8+8\times\log_2(8)+2=90$, $8\times2+8\times\log_2(8)+1=41$, and 7, respectively. The CCs of the proposed synchronization scheme are summarized in Table 2-2. A huge complexity reduction is achieved by the proposed scheme. Ignoring the part of fine frequency synchronization, the proportions of real multipliers and real adders required for the proposed scheme are only 44044296/8606711808 = 0.51%, and 40898552/8581545984 = 0.48% of that for the time domain realization, respectively. Therefore, our proposed sparse-FFT-assisted synchronization scheme can reduce the computation complexity by nearly 200 times, without the BER penalty in comparison with the conventional sliding window

correlation algorithm. For further comparison, Park's approach with the same TSs length takes 33619968 real multipliers and 33587200 real adders. However, please notice that the above results are calculated in the condition that the length of the received signal is only 32768, for ease of calculation. In practice, the received signal length for timing synchronization is far more than this value [63]. Then, the advantage of our proposed S-FFT-based scheme on complexity will be more obvious. Therefore, the proposed scheme is ideally desired for cost- and delay-sensitive optical communication systems with the real-time requirements.

2.5.3 Complexity Analysis of the S-FFT assisted FOD monitoring

The complexity of three FOE schemes for a duration of 100 is summarized in Table. 2-3. The first scheme operates FFT-FOE every 10 μs using 4096 symbols. The second scheme only operates FFT-FOE once without FO tracking. The proposed scheme monitors FOD every 10 μs . If an alarm occurs, down-sampling-based FFT-FOE is operated. Twice FOD alarms are assumed here. The number of required real multipliers of single FOD monitoring and down-sampling based FFT-FOE is 2051 and 896, respectively. With the FOD monitoring, it takes ultra-low additional complexity while the best system performance is guaranteed.

Table 2-3. Complexity analysis of the proposed FOD monitoring scheme

FOE scheme	Real multipliers	Real adders	Best BER?
Continuous FFT-FOE	901120	630784	Yes
One shot FFT-FOE	81920	57344	No
The proposed	104222	68588	Yes

2.6 Summary

In this Chapter, S-FFT-assisted multi-parameter monitoring schemes of modulation format, TO, FO, and FOD are proposed and demonstrated for next-generation optical transmission systems and networks. Specifically, a blind and efficient MFI scheme is first proposed for flexible coherent transceiver. Based on the 4^{th} power transform and partition of QPSK-like points, the proposed MFI shows high accuracy for QPSK and 16/32/64QAM. Moreover, the complexity is substantially reduced by S-FFT. A hitless flexible coherent transceiver based on the proposed MFI is experimentally verified with fast format switching between 64QAM-32QAM and 32QAM-16QAM. Then, an S-FFT-assisted efficient and low-complexity timing/frequency synchronization is proposed with the optimized TSs. For the coherently detected signal, not only the FO effect on the timing synchronization is eliminated, but the FO value is also simultaneously obtained for consequent FO compensation. Simulation results show that if the received signal is aliased with a proper subsampling rate, high accuracy of timing synchronization can be achieved even at the region of very low SNR, while the complexity is greatly reduced. Moreover, the complete FOE range of ±symbol rate/2 with a fine resolution is achieved. Experimental results further verified the robustness and feasibility of the proposed scheme for PDM-16/32QAM signals. The total complexity is reduced by nearly 200 times in comparison with the conventional realization of synchronization in the time domain. The proposed synchronization scheme is useful for future coherent fiber optical transmissions where resource-saving is necessary. In the end, an S-FFT-based FOD monitoring scheme is proposed, by which optimum performance and minimum hardware-cost of FOE are achieved

simultaneously. A down-sampling process is proposed to further reduce the complexity of subsequent FFT-FOE. FOD monitoring is ideally desired to be applied in cost-sensitive coherent transmission systems.

Chapter 3

Joint Linear and Nonlinear Noise Monitoring Techniques Based on Spectrum Analysis

In this Chapter, a modulation-format-transparent, accurate joint linear and nonlinear noise monitoring scheme based on the calculation of correlation between two spectral components at the upper and lower sideband of the signal spectrum is proposed. Different characteristics of flat linear noise spectrum and non-flat nonlinear noise spectrum are used to distinguish the influences on the correlation value from both noise sources. Simulation results show that the proposed scheme can accurately monitor SNR_{linear} and $SNR_{nonlinear}$ within a wide launch power range from -5 dBm to 5 dBm per channel for multi-channel WDM systems with a 915-km SSMF link. The performance of the proposed scheme is further experimentally verified in up-to-7 channel WDM systems over a 915 km SMF link.

3.1 Introduction

In next-generation flexible and dynamic optical networks, reliable network planning, operation, and reconfiguration highly rely on the quality of optical path link [69, 70]. Therefore, robust and efficient OPM becomes ever more important in order to extract the impairment information from the received signal [5]. The operators are able to evaluate the QoT, obtain link failure warning, identify the reasons for underperformance, and take possible countermeasures according to monitored OSNR value. So far, there have been various OSNR monitoring techniques proposed for different development stages of optical transmission systems. Early OSNR monitoring was mainly realized in the optical domain. However, the most classic out-of-band interpolation method [22] can not be employed for dense WDM systems with small channel spacing, while the polarization nulling method [24] can not be used for the PDM system. Meanwhile, the robustness and reconfigurability of OSNR monitoring techniques based on traditional optical components are relatively unsatisfactory [71].

Thanks to the development of coherent detection and DSP techniques, one can make full use of optical field information to perform analysis in the electrical domain [4]. The calculation of electrical SNR can be realized by powerful and flexible DSP algorithms, which provides great convenience for engineers. A number of DSP-based OSNR monitoring methods have been proposed, e.g. the ESNR can be calculated based on EVM [25], Stokes-vector [72], cyclostationary property, [27] and statistical moments [26], or aided by training symbols [73]. However, these methods do not take nonlinear noise into account. As analyzed and verified extensively in previous works [28, 74], in a long-haul transmission link with sufficient accumulated CD and fiber

nonlinearity, the nonlinear noise can be approximately modeled as additive Gaussian noise in the time domain. Therefore, it is difficult to distinguish ASE noise induced by EDFA and nonlinear noise. The presence of nonlinear noise not only leads to an underestimation of OSNR but also makes it difficult to accurately evaluate the link condition [5]. To address this problem, a number of schemes have been proposed to eliminate the OSNR estimation error induced by nonlinearity. For example, nonlinearity can be measured using inserted pilot signals [37, 38]. However, the SE and system flexibility are sacrificed. In [29], the EVM-based method is employed with the NLI fitting using amplitude noise correlation between neighboring symbols after CPR, while in [30], the statistical moments-based SNR estimation method is used in combination with amplitude correlation functions (ACFs) between two symbols of the signal to fit estimate the impact of NLI. It should be noticed that such kind methods should be conducted with the aid of several DSP demodulation steps (after CPR [29] or after adaptive equalization [30]). From the perspective of the practical system, they not only exhibit relatively high power-consumption and unavoidable DSP-induced noise (e.g. the taps of adaptive equalizers do not converge perfectly) [4, 39] but also are not transparent to modulation formats and hence unsuitable for flexible optical networks where multiple possible formats can be employed for data transmission [75]. On the other hand, it remains highly desirable to distinguish and monitor the linear and nonlinear noise simultaneously (not only OSNR monitoring), enabling comprehensive system analysis for operators. ML-based methods have shown some potential, but it remains challenging to acquire a huge amount of high-quality training datasets. A

simpler and effective method to monitor both linear and nonlinear noise is still worthy of studying.

In this Chapter, a modulation-format-transparent, accurate joint linear and nonlinear noise monitoring scheme is proposed based on correlation calculation between two spectral components at the upper and lower sideband of the signal spectrum after CD compensation (CDC). Inspired by different characteristics of flat linear noise spectrum and non-flat nonlinear noise spectrum, a semi-analytical investigation on their influences on the correlation value is carried out. Linear and nonlinear noise are found to have different contributions to SNR calculation and the decline rate of the correlation value with FO. The joint monitoring is successfully realized by building a system of bivariate first-order equations using both noises as variables. Simulation results show that the proposed scheme can accurately monitor SNR_{linear} and $SNR_{nonlinear}$ simultaneously, with a wide launch power range from -5 dBm to 5 dBm per channel for 1-, 3-, 5-, 7-channel WDM systems in a 915-km SSMF link. The performance of the proposed scheme is further experimentally verified in up-to-7 channel 16-QAM WDM systems with a 915 km SMF link consisting of 12 spans with different lengths, supporting launch power ranging from -3 dBm to 3 dBm per channel. The experimental estimation errors of SNR_{linear} and $SNR_{nonlinear}$ are lower than 0.3 dB and 2.4 dB, respectively.

3.2 Theoretical Foundations

3.2.1 SNR Monitoring Using Signal Spectral Correlation

The proposed scheme operates on the basis of a classical cyclostationary property-based SNR estimation method [76]. Cyclostationary property of digitally modulated

signal has been comprehensively investigated in [77, 78]. Here, a brief introduction of the basic principle as well as the derivation of the expression of SNR estimation is provided. For commonly used digital modulation formats, such as amplitude-shift keying (ASK), binary phase-shift keying (BPSK), QPSK, and QAM, their pseudo-random amplitude and phase variations may be difficult to distinguish from random amplitude and phase variations of additive Gaussian noise generated after transmission through the optical amplified link. However, since the modulated symbol durations are predetermined and time-invariant, the statistical property of the signal should be distinguishable from that of Gaussian noise. The 1st and 2nd order statistical properties (i.e. the mean value and autocorrelation function) are defined as:

$$\bar{\mu}_x = E[x(t)] \tag{3.1}$$

$$\bar{R}_x(\tau) = E[x(t+\frac{\tau}{2}) \cdot x^*(t-\frac{\tau}{2})] \tag{3.2}$$

where $x(t)$ is the signal, while $\bar{x}$ and x^* represent the estimated value and the complex conjugate of x, respectively, and E is the expectation operator (averaging in the time domain). Although the mean values of signal and additive Gaussian noise are both zero, the autocorrelation function of digitally modulated signals is periodic in time (at a periodic interval of symbol duration T_s) [77], as long as τ is less than T_s, while that of additive Gaussian noise does not exhibit such periodicity. Therefore, in [78], the digital modulated signal is identified as a wide-sense cyclostationary process while additive Gaussian noise is wide-sense stationary. The periodicity of the autocorrelation function of digitally modulated signals is manifested in the signal's optical frequency spectrum, which exhibits strong correlations between time-varying amplitude and

phase sequences of certain pairs of spaced apart spectral components, whereas such correlations do not exist in the optical spectrum of additive Gaussian noise. Correlations between various spectral components of a digitally modulated signal can be described by a spectral correlation density function (SCDF), $S_x^{\alpha}(f)$, which is defined as the Fourier transform of the cyclic autocorrelation function [76], $R_x^{\alpha}(\tau)$, of the time-varying signal sequence $x(t)$, as

$$R_x^{\alpha}(\tau) \equiv E[x(t+\tau/2)\cdot x^*(t-\tau/2)\cdot \exp(-j2\pi\alpha\tau)] \tag{3.3}$$

and then $S_x^{\alpha}(f)$ is

$$S_x^{\alpha}(f) \equiv \int_{-\infty}^{\infty} R_x^{\alpha}(\tau)\cdot \exp(-j2\pi f\tau)d\tau \tag{3.4}$$

Equivalently, the SCDF may be expressed as a correlation function of the time-varying amplitudes of the spectral components of the modulated signal, as

$$S_x^{\alpha}(f) \equiv E[X_T(t, f+\alpha/2)\cdot X_T^*(t, f-\alpha/2)] \tag{3.5}$$

where

$$X_T(t,v) = \int_{t-T/2}^{t+T/2} x(u)\cdot \exp(-j2\pi vu)du \tag{3.6}$$

and T is integration time much larger than T_s. Then, we normalize the SCDF to limit its range within [-1, 1], as

$$\hat{S}_x^{\alpha}(f) \equiv \frac{E[X_T(t, f+\alpha/2)\cdot X_T{}^*(t, f-\alpha/2)]}{\sqrt{E[\left|X_T(t, f+\alpha/2)\right|^2]}\sqrt{E[\left|X_T(t, f-\alpha/2)\right|^2]}} \tag{3.7}$$

It is known that for noiseless signals modulated with previously mentioned formats, QAM et.al., $\hat{S}_x^{\alpha}(f)$=1 when $\alpha=\alpha_0=1/T_s$ and for all f within [$-\alpha/2$, $\alpha/2$]. Here, it should be noticed that in digital optical transmission, the bandwidth of a signal

is shaped by both electrical and optical filters (e.g. raise-cosine filter, anti-aliasing filter, limited bandwidth of electronic or optics devices) to limit the occupied bandwidth. Therefore, at the receiver side, $\hat{S}_x^{\alpha}(f)=1$ holds under a slightly more stringent condition: Two frequencies $f-\alpha_0/2$ and $f+\alpha_0/2$ should be within the bandwidth of the modulated signal. In contrast to modulated signals, ASE noise is a random Gaussian process and does not exhibit any significant correlation between its spectral components. Therefore, when additive Gaussian noise is added to a modulated signal, the normalized SCDF is always smaller than unity, i.e. $\hat{S}_x^{\alpha}(f)<1$. Letting n denote time sequence of additive Gaussian noise and the relation between $N_T(t,v)$ and n be defined as Eq. (3.6), we have the following Fourier transform relation:

$$\tilde{X}_T(t,v)=\int_{t-T/2}^{t+T/2}(x(u)+n(u))\cdot\exp(-j2\pi vu)du=X_T(t,v)+N_T(t,v) \tag{3.8}$$

Then, the normalized SCDF can be expressed as

$$\hat{S}_x^{\alpha_0}(f)=\frac{E[X_T(t,f+\alpha/2)\cdot X_T^*(t,f-\alpha/2)]}{\sqrt{E[|X_T(t,f+\alpha/2)|^2+|N_T(t,f+\alpha/2)|^2]}\cdot\sqrt{E[|X_T(t,f-\alpha/2)|^2+|N_T(t,f-\alpha/2)|^2]}} \tag{3.9}$$

Noted that for the numerator, $E[X_T(t,f+\alpha/2)\cdot N_T^*(t,f-\alpha/2)]$, $E[N_T(t,f+\alpha/2)\cdot X_T^*(t,f-\alpha/2)]$, $E[N_T(t,f+\alpha/2)\cdot N_T(t,f-\alpha/2)]$ are obviously all zero for all $\alpha>0$. Considering the condition of $f=f_c$, where f_c is the carrier center frequency (after coherent detection without FO, f_c is 0 in the electrical spectrum), since the power spectra of aforementioned modulation formats are symmetric about f_c, then

$$E[|X_T(t, f_c+\alpha/2)|^2]=E[|X_T(t, f_c-\alpha/2)|^2]=E[P_S(f_c\pm\alpha/2)] \tag{3.10}$$

Meanwhile, the spectrum of additive Gaussian noise is flat over all frequency,

$$E[|N_T(t, f_c+\alpha/2)|^2]=E[|N_T(t, f_c-\alpha/2)|^2]=E[P_N(f_c\pm\alpha/2)] \tag{3.11}$$

where P_S and P_N are the power of signal and noise, respectively. The normalized SCDF with $\alpha=\alpha_0=1/T_S$ becomes

$$\hat{S}_x^{\alpha_0}(f_c)=\frac{E[P_S(t, f_c\pm\alpha_0/2)]}{E[P_S(t, f_c\pm\alpha_0/2)]+E[P_N(t, f_c\pm\alpha_0/2)]} \tag{3.12}$$

Then, the SNR of the two spectral components at $f_c\pm\alpha_0/2$ can be expressed as

$$SNR(f_c,\ \alpha_0)=\frac{E[P_S(t, f_c\pm\alpha_0/2)]}{E[P_N(t, f_c\pm\alpha_0/2)]}=\frac{\hat{S}_x^{\alpha_0}(f_c)}{1-\hat{S}_x^{\alpha_0}(f_c)} \tag{3.13}$$

Considering the SNR calculation of the whole signal, it needs to include whole signal power and noise power within the whole measurement bandwidth B_{meas}, as

$$SNR=\frac{\sum_{f_i\in B_{meas}}E[P_S(t, f_i)]}{E[P_N(t)]\cdot B_{meas}}=\frac{\sum_{f_i\in B_{meas}}E[P_S(t, f_i)+P_N(t)]}{E[P_N(t)]\cdot B_{meas}}-1 \tag{3.14}$$

where f in $P_N(t)$ is omitted due to the spectral flatness of Gaussian noise. In Eq. (3.14), $E[P_N(t)]$ can be calculated according to Eq. (3.13), as

$$E[P_N(t)]=E[P_S(t,\ f_c\pm\alpha_0/2)+P_N(t)]\cdot[1-\hat{S}_x^{\alpha_0}(f_c)] \tag{3.15}$$

Replacing Eq. (3.15) into Eq. (3.14), we can obtain

$$SNR=\frac{\sum_{f_i\in B_{meas}}E[P_S(t, f_i)+P_N(t)]}{E[P_S(t, f_c\pm\alpha_0/2)+P_N(t)]\cdot B_{meas}}\cdot\frac{1}{[1-\hat{S}_x^{\alpha_0}(f_c)]}-1 \tag{3.16}$$

According to Eq. (3.16), the SNR estimation can be efficiently realized by a few simple steps:

(1) Measure the power of the whole received signal within B_{meas} , i.e. $\sum_{f_i \in B_{meas}} E[P_S(t, f_i) + P_N(t)]$.

(2) Use a pair of narrowband filters with center frequency at f_c-$\alpha_0 / 2$ and f_c+$\alpha_0 / 2$ to filter out two spectral components, as illustrated in Fig. 3-1(a). Measure the power of these two spectral components and scale it according to the relative size of B_{meas} and the bandwidth of narrowband filters. Then we obtain $E[P_S(t, f_c \pm \alpha_0 / 2) + P_N(t)] \cdot B_{meas}$.

(3) Calculated $\hat{S}_x^{\alpha_0}(f_c)$ using two spectral components obtained in step (2). Actually, the calculation of $\hat{S}_x^{\alpha_0}(f_c)$ is very straightforward. In step 2, from the perspective of the time domain, after filtering, we obtain two time-varying sequences whose FFT transforms are two spectral components located at f-$\alpha_0 / 2$ and f+$\alpha_0 / 2$ in frequency domain. Therefore, complicated steps from Eq. (3.5) to Eq. (3.7) which includes FFT and time averaging can be simplified by direct time-domain correlation calculation between the above-mentioned two filtered time-varying sequences, as long as the sequence length is long enough.

The normalized SCDF and the SNR estimated from the normalized SCDF versus reference in-band SNR is plotted in Fig. 3-1(b), showing highly reliable and accurate SNR estimation performance. The bandwidth of the narrowband filters is fixed at 100 MHz [76].

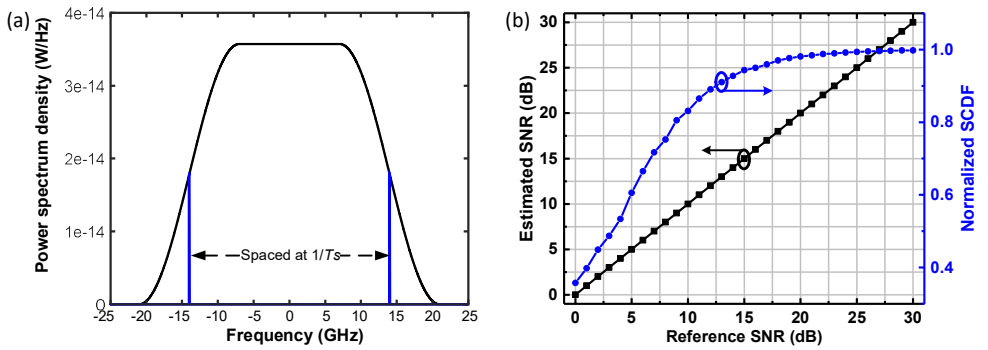

Fig. 3-1. (a) A power spectrum of 28 GBaud16-QAM signal and spectral components used for measuring the correlation value spaced at 28G. Signal power is 0 dBm and the roll-off factor (ROF) is 0.5. (b) The normalized SCDF calculated using two spectral components in (a), and the estimated SNR from the SCDF versus reference actual SNR.

The correlation calculation-based SNR technique has the following advantages:

(1) It is modulation format transparent because only spectrum information is used without the need for demodulation by complicated DSP, i.e. Format-dependent adaptive equalization, CPE, and de-mapping. The only necessary pre-process is CDC, which does not depend on the format. It should be noticed that CDC is essential to avoid correlation degradation since a time delay between the spectral components at the upper and lower sideband will be induced by CD.

(2) Benefiting from the "quasi-DSP free" feature, DSP-induced noise and the impact of residual phase noise are avoided, while conventional DSP-based OSNR monitoring techniques (e.g. EVM calculation) depend significantly on the DSP performance.

(3) The performance is insensitive to random rotation in the polarization state and PMD in the PDM systems since the impact of PMD exists in both the spectral components at the upper and lower sideband of the signal spectrum, which are mixtures of X- and Y-tributaries before polarization demultiplexing. Meanwhile, it is robust to FO, as explained after Eq. (3.7), although not insensitive.

3.2.2 Impact of Nonlinearity on SNR Monitoring

Like most OSNR monitoring techniques, strong fiber nonlinearity will affect the above SNR estimation method. Plenty of previous research works have modeled the nonlinear noise as a Gaussian-like noise in the time domain. It means that nonlinear noise can simply be added to ASE noise and its impact on system performance could be assessed through a modified SNR considering both noise sources. Therefore, the SNR calculated based on EVM actually reflects the "true (or effective)" SNR contributed by both linear and nonlinear noise. To be fair, this "true" SNR can be used to evaluate the QoT of the channel of interest (COI), since fiber nonlinearity compensation algorithms such as digital backpropagation (DBP) [79] are still too complex to be realistic at present. However, for the above signal spectral correlation-based-SNR estimation method, different from methods like EVM calculation, etc., the impact of fiber nonlinearity is more complex. Although acting as a Gaussian-like noise, nonlinear noise is a data-dependent noise generated by the signal itself. Some of the nonlinearity-insensitive OSNR methods have employed amplitude noise correlation calculation between adjacent symbols in the time domain to calibrate the estimated OSNR value [29, 37]. Therefore, it is foreseeable that the nonlinear noise at the upper and lower sideband of the signal spectrum will also show correlation to a certain extent, unlike the ASE noise. In addition, the correlation between nonlinear noise is unlikely to be as strong as that of the modulated signal. Here, simulations are conducted to study the cyclostationarity-induced correlation characteristic of nonlinear noise for up-to-7 channel 16-QAM signal. The simulation setup is a 915-km link consisting of 12 equal SMF spans without ASE noise loading. Different from the clear cyclostationary property of the signal and

additive Gaussian noise, cyclostationarity-induced correlation characteristic of nonlinear noise is much more complicated since the NLI is not only generated by the COI itself but also induced by other channels. Therefore, the number of WDM channels will certainly affect the overall correlation characteristic of NLI. Figure 3-2(a) shows the relationship between the reference and estimated $SNR_{nonlinear}$ using spectral correlation-based SNR estimation method. There are two noteworthy points in Fig. 3-2(a). Firstly, different from ASE noise, nonlinear noise components at the upper and lower sideband of the signal spectrum will also show correlation to a certain extent, resulting in the overestimation of $SNR_{nonlinear}$. Secondly, it is found that the gap between the estimated and reference $SNR_{nonlinear}$ decreases with the number of WDM channels. Such a phenomenon can be explained by the strength of NLI induced correlation. The NLI generated by self-channel interference (SCI) is expected to have the strongest correlation within the spectrum of the COI, while the cross-channel interference (XCI) and multi-channel interference (MCI) induced NLI is of less correlation [28]. Overall, the correlation of the two spectral components and the $SNR_{nonlinear}$ overestimation decreases with the number of WDM channels. Such characteristics bring great trouble to our measurement: Our final measurement value is not the SNR solely caused by ASE, nor "combined" SNR caused by the combination of linear and nonlinear noise, but an intermediate value, as shown in Fig. 3-2(b), where the single-channel 16-QAM signal is simulated and the simulation setup is the same as that in Fig. 3-2(a) with the noise figure of EDFAs set to 6 dB. The amount of nonlinear noise can be calculated by both simulation and analytical GN models [28]. It is clearly observed that the estimated SNR is always higher than combined SNR while lower than ASE-induced noise.

Therefore, when there is a strong NLI, the measurement result will become meaningless since it cannot reflect any useful information of link condition to guide operators' action.

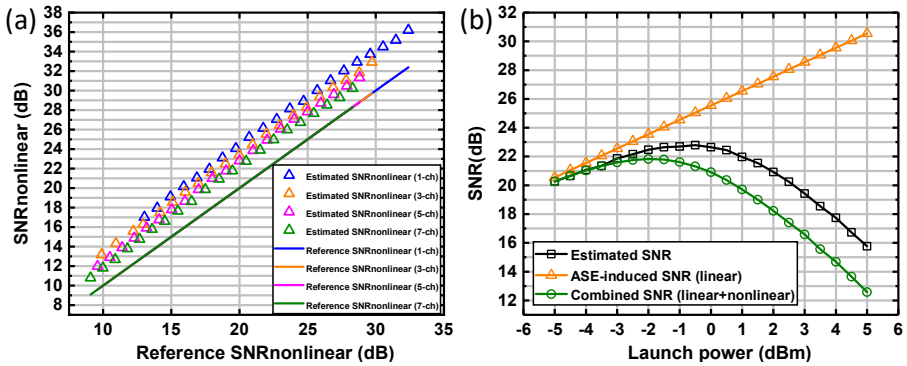

Fig. 3-2. (a) The relationship between the reference and estimated $SNR_{nonlinear}$ using spectral correlation-based SNR estimation for up-to-7-channel WDM systems. (b) Combined SNR, ASE-induced SNR, and the estimated SNR of a single-channel 16-QAM signal.

3.2.3 Different Characteristics of Linear and Nonlinear Noise in the Frequency Domain

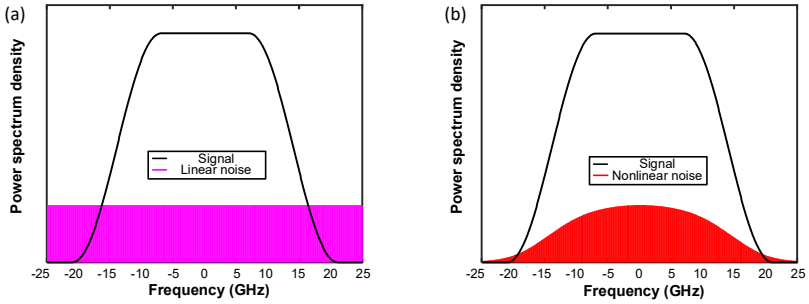

Fig. 3-3. (a) Signal spectrum of 28 GHz 16QAM signal and pure linear noise spectrum; (b) Signal spectrum of 28 GHz 16QAM signal and pure nonlinear noise spectrum. ROF=0.5

In the time domain, the nonlinear noise acts like Gaussian noise, making it difficult to be distinguished from ASE noise. However, the spectrum shapes of linear and nonlinear noise present different characteristics in the frequency domain, i.e., linear noise is flat in the frequency domain, while the nonlinear noise spectrum is non-flat. Figure 3-3(a) plots power spectrum density (PSD) of the signal and pure linear noise, while Fig. 3-3(b) plots PSD of signal spectrum and pure nonlinear noise spectrum,

where the nonlinear noise spectrum is calculated using the GN model [28]. The setup is the same as the point in Fig. 3-2 with the launch power of 0 dBm. The noise part has been exaggerated to facilitate viewing, so the ordinate is omitted.

Then, let's consider the scenario in the presence of FO and its impact on spectral correlation calculation. In the correlation measurement step described previously, for a 28 Gbaud signal, if FO is absent, the ideal situation is to filter out two spectral components at the lower and upper sideband at a frequency of ± 14 GHz which show a central symmetry with the zero frequency. If FO is present, the positions of the two upper and lower sideband signals at the interval of 28 GHz are no longer symmetrical about the center frequency, as shown in Fig. 3-4. In Fig. 3-4, the FO is set to be 3 GHz. Here, the effect of FO is equivalently manifested in the position moving of the two narrowband filters instead of that of signal spectrum for convenience. It is worth noting that the power of two spectral components is no longer the same.

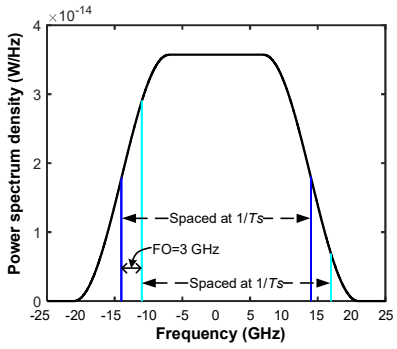

Fig. 3-4. Position moving process of the two spectral components at the upper and lower sideband with induced-FO of 3 GHz. The signal parameter is same as that in Fig. 3-1(b).

Next, let's analyze the impact of FO on the calculation of correlation $\hat{S}_x^{\alpha_0}(f)$. For a noiseless signal, the $\hat{S}_x^{\alpha_0}(f_c)$ remain theoretically 1 as $\hat{S}_x^{\alpha_0}(f_c)$, as stated in Section 2.1. It is easy to understand because this process is equivalent to the scenario where there are two identical signals, and one of them is amplified and the other is attenuated.

Obviously, $\hat{S}_x^{\alpha_0}(f_c)$ is still 1 when there is not any noise. But for a signal with flat ASE noise PSD as in Fig. 3-3(a), the situation is quite different. Although the PSD of the signal has changed due to its position moving in the spectrum, the PSD of noise is constant across all frequencies. It means that, in the process shown in Fig. 3-4, the PSD of the spectral component at the upper sideband (in the right part of Fig. 3-4) decreases significantly, and the proportion of noise increases. Although for the lower sideband signal (in the left part of Fig. 3-4) the condition is the opposite , it should be noticed that for the correlation calculation, the result is much more dependent on the noisier component, i.e. the spectral component in the upper sideband in Fig. 3-4, which causes the drop of $\hat{S}_x^{\alpha_0}(f_c)$. Therefore, $\hat{S}_x^{\alpha_0}(f_c)$ will decrease with FO. On the other hand, for the nonlinear noise spectrum as shown in Fig. 3-3(b), it can be found that the PSD of the nonlinear noise is not flat, but it becomes smaller at the edge of the spectrum. According to the above analysis, it can be known that in the nonlinear case, when there is a certain amount of FO, $\hat{S}_x^{\alpha_0}(f_c)$ will drop, but not as fast as in the scenario of pure linear noise. This is because as the PSD of the signal spectral component at the upper sideband decreases, the PSD of nonlinear noise also drops, keeping its proportion relatively low. From the above analysis, it can be concluded that the presence of linear and nonlinear noise can both cause a decrease of $\hat{S}_x^{\alpha_0}(f_c)$ with FO. However, the contribution of linear noise is more significant than that of nonlinear noise. Then, it is possible to find a way to distinguish between them.

3.3 Joint Linear and Nonlinear Noise Monitoring Scheme Design

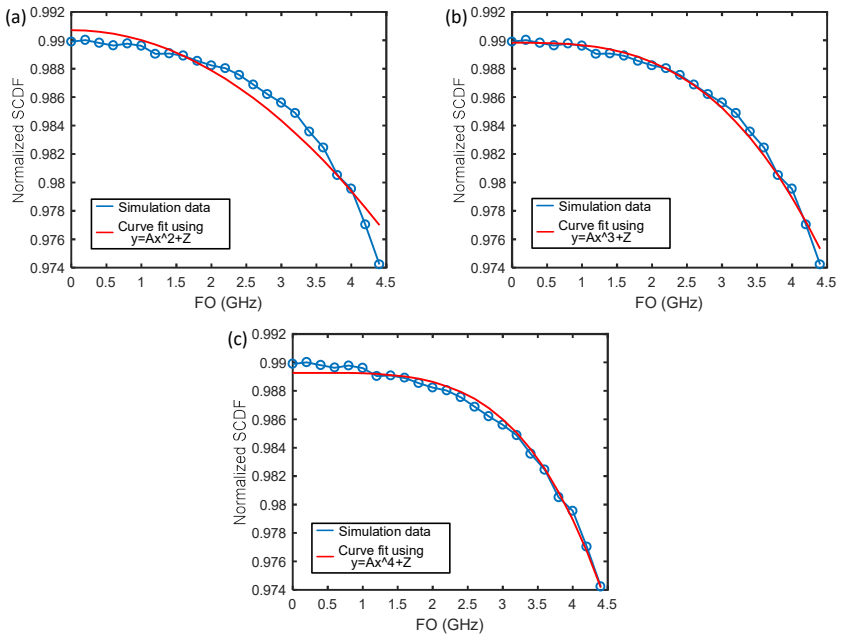

Fig. 3-5. Fitting $\hat{S}_x^{\alpha_0}(f)$ as a function of FO using (a) $y = Ax^2 + Z$, (b) $y = Ax^3 + Z$, and (c) $y = Ax^4 + Z$.

It is needed to study the relation between $\hat{S}_x^{\alpha_0}(f)$ and FO through numerical simulation. Figures 3-5(a)-3-5(c) show the simulation result where $\hat{S}_x^{\alpha_0}(f)$ decreased with FO from 0 GHz to 4.5 GHz when launch power is 0 dBm, and the red lines in Figs. 3-5(a)-3-5(c) represent fitting curves using $y = Ax^2 + Z$, $y = Ax^3 + Z$, $y = Ax^4 + Z$. It can be clearly observed that the cubic function fits better than the quadratic function. On the other hand, it seems that the cubic function fits also better than the quartic function, at least the cubic function can respond well to the decreasing tendency of $\hat{S}_x^{\alpha_0}(f)$ with FO. According to principle of the Occam's Razor [80], in polynomial fitting, it is better to choose the simplest form of the lowest order on the premise of performance guarantee [81]. Meanwhile, in simulation, better monitoring performance is achieved with the A fitted by $y = Ax^3 + Z$ than that by the quadratic and quartic functions.

Therefore, for the detected signal, the frequency sweep method is used to obtain a series of $\hat{S}_x^{\alpha_0}(f)$ values with various FO, and the cubic function $y = Ax^3 + Z$ is chosen to carry out curve fitting and obtain A, which reflects the rate of decline of $\hat{S}_x^{\alpha_0}(f)$ with FO. Figure 3-6 shows the relation between A and launch power. Values of A are obtained using the above-described curve fitting process and the system setup is the same as that in Fig. 3-2. It can be seen that the absolute value of A shows a trend of falling first and then rising with launch power, which reflects a comprehensive effect of linear and nonlinear noise, as predicted.

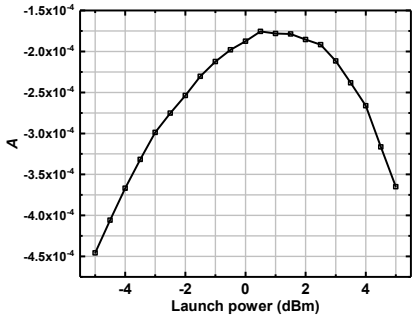

Fig. 3-6. Relation between coefficient A obtained by cubic curve fitting and launch power.

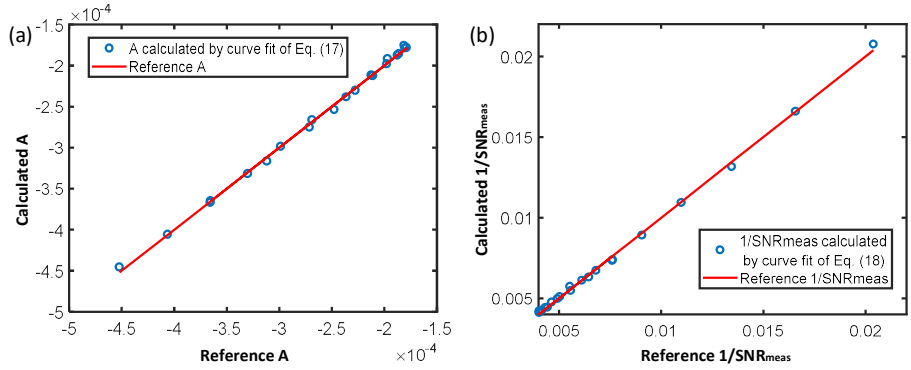

Fig. 3-7. Curve fitting result of (a) Eq. (3.17) and (b) Eq. (3.18) using 21 pairs of (SNR_{linear}, $SNR_{nonlinear}$), with the launch power swept from -5 dBm to 5 dBm at a stepsize of 0.5 dBm. SNR_{meas} is measured using the spectral correlation-based SNR estimation method.

Based on the analysis in Section 2.3. It is known that the contribution of linear noise and nonlinear noise to A is different. Here a simple relationship is proposed

$$A = A_1 * \frac{1}{SNR_{linear}} + A_2 * \frac{1}{SNR_{nonlinear}} + A_3 \tag{3.17}$$

where A_1 and A_2 represent the contribution factor of linear and nonlinear noise to A, respectively, and A_3 represents the bias introduced by other inherent factors. Whether such a simple relationship is correct or not requires investigation through numerical simulation. In the simulation, a series of (SNR_{linear}, $SNR_{nonlinear}$) pairs of signals are collected after 915km fiber link by adjusting the launch power from -5 dBm to 5 dBm at a step size of 0.5 dBm. SNR_{linear} is calculated according to the traditional ASE noise accumulation model [70], and $SNR_{nonlinear}$ is calculated by the GN-model. Figure 3-7(a) shows the fitting result for Eq. (3.17) when the ROF is equal to 0.5 and the FO is swept from 0 GHz to 4.5 GHz. The FO sweeping range should be optimized according to different ROF, which determines the signal bandwidth. The objective of the optimization is to minimize the estimation error, and it will not be explained in detail here. The results show that the assumption of Eq. (3.17) is quite accurate. In addition, in the fitting process of Fig. 3-6, it is found that A_1=-0.04866 and A_2=-0.00608, which confirms the previous inference that "linear noise contributes more to A than nonlinear noise".

Now it is found that there are two unknowns, i.e. SNR_{linear} and $SNR_{nonlinear}$, but there is only one bivariate first-order equation, i.e. Eq. (3.17). Obviously, it is needed to find an additional equation to build a system of bivariate first-order equations. Careful readers may have already found out that the second equation has appeared already in Fig. 3-2(b). In the previous analysis, it has been concluded that the nonlinear noise existing in the spectral components at the upper and lower sideband are not as

uncorrelated as the ASE noise, and also, they are unlikely to have a very strong correlation as the signal itself. Therefore, when using the spectral correlation-based method to estimate SNR, nonlinear noise has also some contribution to the noise part, although less than linear noise. Therefore, the second bivariate first-order equation can be established:

$$\frac{1}{SNR_{meas}} = B_1 * \frac{1}{SNR_{linear}} + B_2 * \frac{1}{SNR_{nonlinear}} + B_3 \tag{3.18}$$

where B_1 and B_2 represent the contribution factors of linear and nonlinear noise to the estimated noise using the spectral correlation-based SNR estimation method. Figure 3-7(b) shows the curve fitting result for Eq. (3.18), again with high accuracy.

Now, because there are two unknowns and a system of bivariate first-order equations, the problem becomes solvable. In the implementation of the scheme, we can firstly sweep launch power to get a series of (SNR_{linear}, $SNR_{nonlinear}$) pairs and build a system of bivariate first-order equations by curve fitting. Then, given a signal sequence, we can calculate the linear noise and the nonlinear noise simultaneously. Although this scheme is based on the dataset for curve fitting, the required quantity is much less than that for ML models since, in our scheme, the curve fitting steps are very simple and straightforward, while for ML models the training and optimization process is much more complicated and depends highly on huge amounts of the high-quality training dataset.

3.4 Simulation Study and Results

The simulation setup is a PDM WDM transmission system with a 915 km link consisting of 12 equal SSMF spans and EDFAs based on the split-step Fourier method

(SSFM) [32]. Single-channel and 3-, 5-, and 7-channel conditions are considered and monitor the center channel. The modulation formats used are QPSK, 16QAM, and 64QAM. SNR_{linear} and $SNR_{nonlinear}$ are changed mainly by adjusting the launch power from -5 dBm to 5 dBm at a step size of 0.5 dBm. Meanwhile, results with different NF of EDFAs i.e. 4 dB, 5 dB, and 6 dB are also provided. Conditions of 6-span and 9-span are also simulated. Therefore, the adjustment of SNR is more flexible. Results with ROF of 0.5, 0.6, 0.7 are presented.

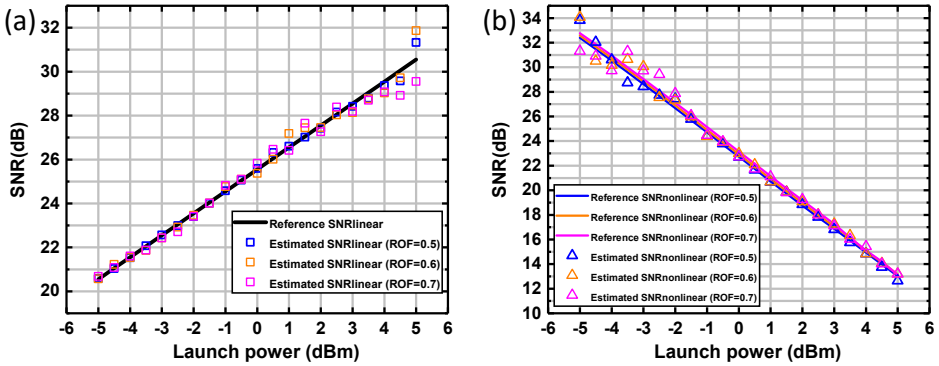

Fig. 3-8. (a) SNR_{linear} monitoring and (b) $SNR_{nonlinear}$ monitoring for single channel 16QAM signal with ROF of 0.5, 0.6, and 0.7. The link is 915 km consisting of 12 equal SMF spans and EDFAs with NF of 6 dB.

Figure 3-8(a) shows the monitoring performance of SNR_{linear} while Fig. 3-8(b) shows the monitoring performance of $SNR_{nonlinear}$ for single-channel 16QAM signal with ROF of 0.5, 0.6, 0.7, respectively. Here, matched filtering is used so that the reference SNR_{linear} for the signal with different ROF are basically the same (as confirmed by simulation). $SNR_{nonlinear}$ is calculated using incoherent GN-model with integration form. As the ROF changes, the corresponding nonlinearity spectrum shows a slight difference so does the value of reference $SNR_{nonlinear}$, as shown in Fig. 3-8(b). The proposed joint SNR_{linear} and $SNR_{nonlinear}$ monitoring scheme can accurately estimate SNR from both noise sources. The estimation error curve of SNR_{linear} and $SNR_{nonlinear}$

are plotted in Figure 3-9(a) and 3-9(b), respectively. It can be seen for both SNR_{linear} and $SNR_{nonlinear}$, the estimation error is smaller than 1.5 dB within an ultrawide launch power range from -5 dBm to 5 dBm. Noted that for estimation of SNR_{linear}, the estimation error is no more than 0.7 dB with the launch power equal to or lower than 4 dBm, which corresponding to the SNR value of 29.55 dB. For a 28 GBaud signal, the SNR value of 29.55 dB is equivalent to the OSNR value of about 33.05 dB with the 0.1 nm noise reference bandwidth [82]. Therefore, the estimation range of our proposed scheme is sufficiently wide to practical application. On the other hand, it can be observed that the estimation error of SNR_{linear} increases with launch power, in opposite to $SNR_{nonlinear}$. This phenomenon is due to that the proportion of linear noise is lower when the launch power is high, while $SNR_{nonlinear}$ decreases by 2 dB with 1 dB increment of launch power. Higher noise proportion is beneficial to estimation accuracy.

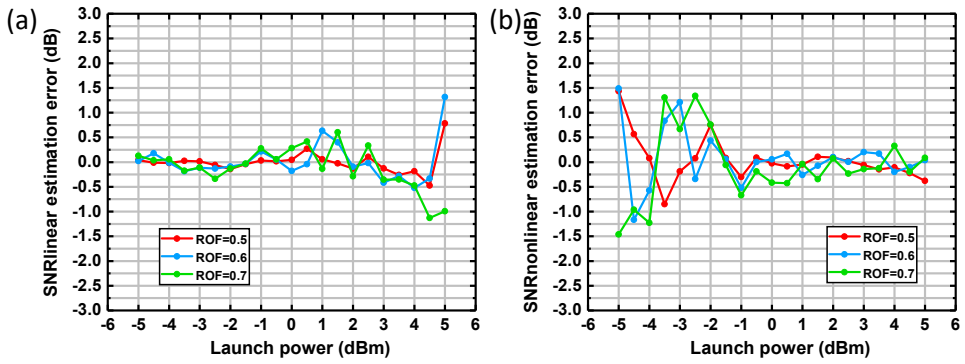

Fig. 3-9. (a) SNR_{linear} estimation error curve and (b) $SNR_{nonlinear}$ estimation error curve of the results in Fig. 3-8.

The performance of the proposed scheme for the conditions with low ROFs is also studied. Since a FO sweeping process of the narrowband filters is operated to filter out the two spectral components, it is necessary to reserve some spectral margins for FO sweeping. After raised cosine shaping, the bandwidth of the signal can be calculated as

$B_{signal} = \text{Symbol rate} \times (1 + \text{ROF})$. The residual spectral margin is $B_{signal}/2\text{-Symbol rate}/2 = \text{Symbol rate} \times \text{ROF}/2$. For a 28 Gbaud signal, the residual spectral margin is 7 GHz with the ROF of 0.5, while it is only 1.4 GHz with the ROF of 0.1. For the signals with low ROFs, e.g. 0.2 and 0.1, the monitoring performance may degrade due to the limited FO sweeping range. Here, linear and nonlinear noise monitoring results are provided for the single-channel 16-QAM signal with ROF of 0.1 and 0.2. As shown in Fig. 3-10, for the signal with ROF of 0.2, the monitoring performance is still acceptable with the estimation errors of SNR_{linear} and $SNR_{nonlinear}$ smaller than 1.1 dB and 1.5 dB, respectively. However, the estimation errors of SNR_{linear} and $SNR_{nonlinear}$ are both exceed 2.2 dB with the ROF of 0.1. Moreover, there is a large fluctuation of the monitoring performance over the launch powers. The results indicate that, the performance of our proposed method is limited for the condition of ultra-low ROFs, where it is difficult to make full use of the unflatness of nonlinear noise over the signal spectrum.

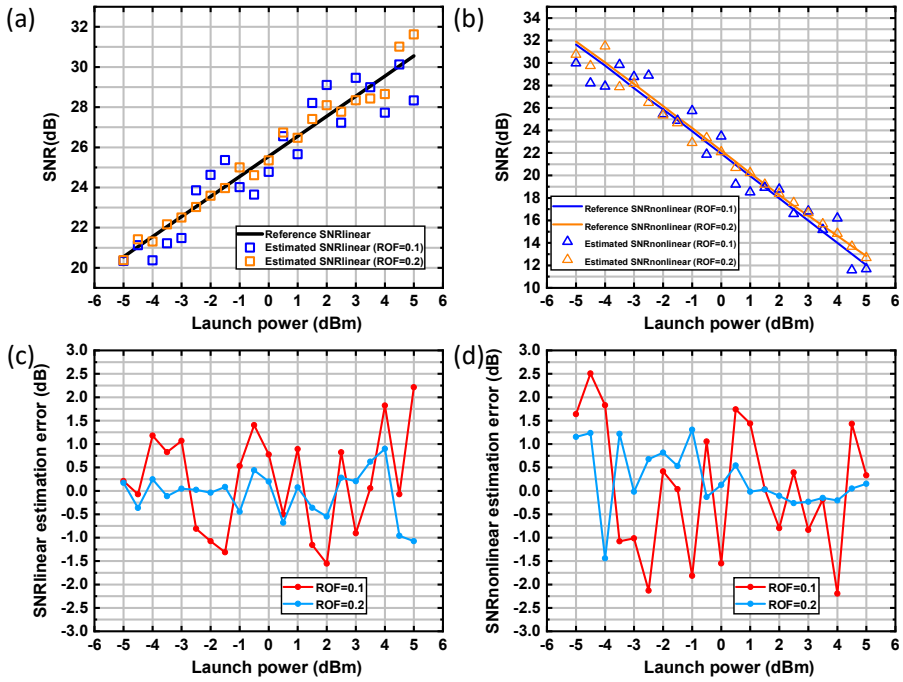

Fig. 3-10. (a) SNR_{linear} monitoring and (b) $SNR_{nonlinear}$ monitoring for single-channel 16QAM signal with ROF of 0.1 and 0.2. (c) SNR_{linear} estimation error curve and (d) $SNR_{nonlinear}$ estimation error curve of the results in Fig. 3-10(a) and 3-10(b), respectively.

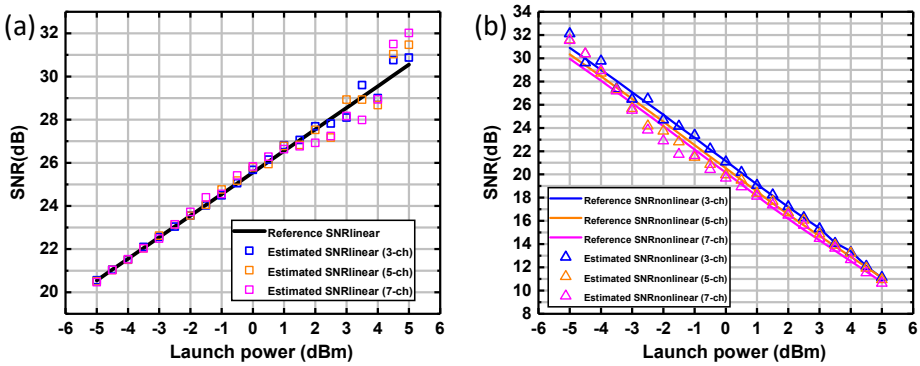

Fig. 3-11. (a) SNR_{linear} monitoring and (b) $SNR_{nonlinear}$ monitoring for multi-channel 16-QAM signal. The simulation setup is the same as that in Fig. 3-8.

Next, multi-channel WDM conditions with the channel number of 3, 5, and 7 are studied. The estimation performance is shown in Fig. 3-11. The results show that the proposed scheme functions well for linear and nonlinear noise monitoring for WDM systems because the nonlinearity spectrum in multi-channel systems also shows the characteristic of non-flatness, as can be observed in Fig. 3 in [28]. The estimation error of SNR_{linear} is smaller than 1.1 dB when the launch power equal to or lower than 4 dBm.

For $SNR_{nonlinear,}$ the estimation error is always lower than 1.6 dB. Here, it is noted that if the numbers of channels on both sides of the COI are different or it is even, the nonlinearity spectrum becomes asymmetric. However, the principle of curve fitting can still be used by FO sweeping at upper and lower sideband separately. Then the nonlinear effect from both the left and right sides of the COI can be fitted. This issue is left for future study.

As analyzed in Section 3.2.2, the number of WDM channels will affect the correlation characteristic of nonlinear noise. Therefore, B_1 and B_2 in Eq. (3.18) vary with the number of WDM channels. Figure 3-12 shows the variation trend of the values of contribution factors in Eq. (3.17) and Eq. (3.18) versus the number of WDM channels. Specifically, when the WDM system scale becomes larger, the correlation of the two spectral components spaced at one symbol rate within the bandwidth of the COI decreases. Therefore, B_2 increases with the number of WDM channels, while B_1 decreases. Meanwhile, the unflatness of the nonlinear noise spectrum is weakened when there are more WDM channels. Therefore, the absolute value of the contribution factor A_2 of the nonlinear noise to A increases while the absolute value of A_1 decreases with the number of WDM channels.

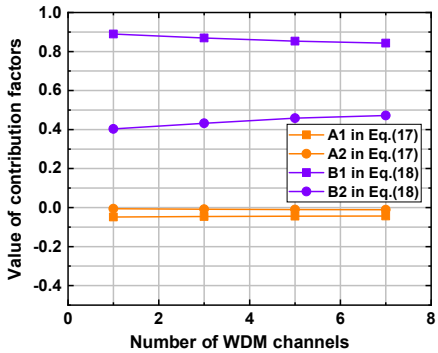

Fig. 3-12. The values of contribution factors in Eq. (3.17) and Eq. (3.18) versus the number of WDM channels.

Figure 3-13 shows the monitoring results for QPSK and 64-QAM signals. The linear and nonlinear estimation error for QPSK is lower than 0.8 dB and 1.5 dB while that for 64-QAM is lower than 1.4 dB and 1.8 dB, respectively. Benefited from the feature of format-dependent DSP-free processing, the proposed scheme is suitable for different commonly used modulation formats and is desired to be employed in flexible optical networks.

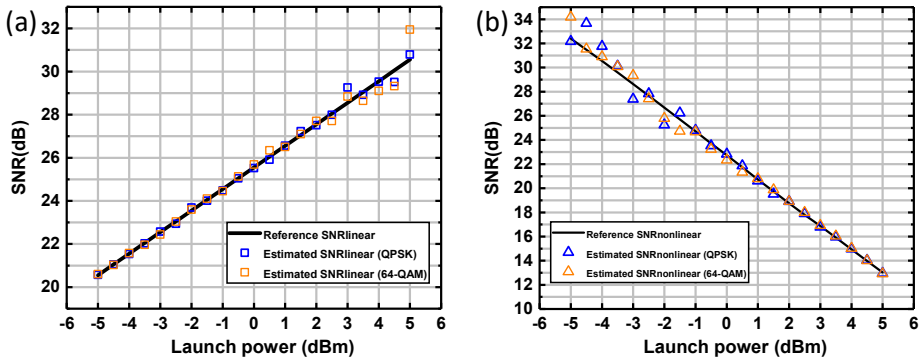

Fig. 3-13. (a) SNR_{linear} monitoring and (b) $SNR_{nonlinear}$ monitoring for single channel QPSK and 64QAM signal. The simulation setup is the same as that in Fig. 3-8.

Essentially, the importance of OSNR monitoring mainly lies in monitoring the link parameter variation. In practice, the NF of inline EDFAs may be time-varying due to temperature, aging, etc. Meanwhile, the number of optical spans through which the signal has been transmitted can be different depending on network structure and transmission requirements in flexible optical networks. The above kinds of parameter variations can be reflected in the OSNR information and are required to be monitored. Therefore, verification is conducted using datasets with different settings of the number of spans and NFs. 6-, 9-, and 12-span conditions are considered with possible NF values of 4 dB, 5 dB, and 6 dB. The dataset consisting of (SNR_{linear}, $SNR_{nonlinear}$) pairs generated in different transmission conditions is used to do curve fitting and test. The

monitoring results are shown in Fig. 3-14. The SNR_{linear} and $SNR_{nonlinear}$ estimation error are lower than 1.7 dB and 1.8 dB, respectively. It indicates that the proposed scheme can deal with a practical time-varying environment and provides reliable optical performance tracking.

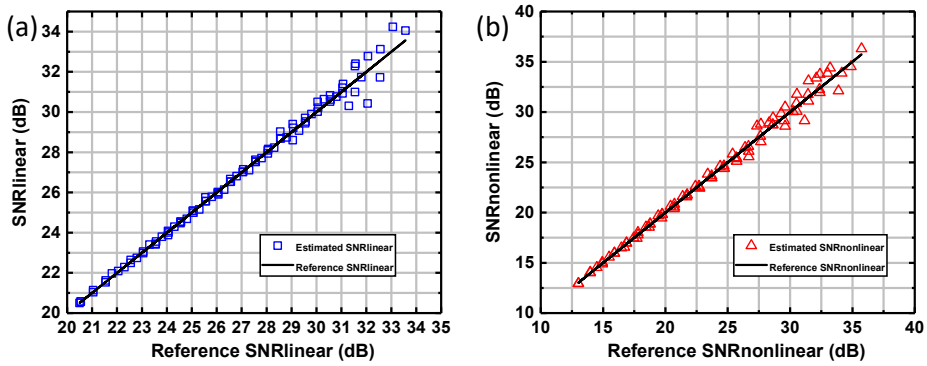

Fig. 3-14. (a) SNR_{linear} monitoring and (b) $SNR_{nonlinear}$ monitoring performance for mixed conditions with span number of 6, 9, and 12, and NF values of 4 dB, 5 dB and 6 dB.

It is necessary to study the impact of the narrow filtering effect of cascaded reconfigurable optical add and drop multiplexers (ROADMs) in meshed optical networks on the monitoring performance and the sensitivity of fitting parameters. Here, Results of the monitoring performance are provided with up-to-12 ROADMs distributed in the transmission link. The filter transfer function $S(f)$ of commercial ROADMs can be modeled as in [83, 84]

$$S(f)=\frac{1}{2}\sigma\sqrt{2\pi}[erf(\frac{B_0/2-f}{\sqrt{2}\sigma})-erf(\frac{-B_0/2-f}{\sqrt{2}\sigma})],\quad \sigma=\frac{B_{OTF}}{2\sqrt{2\ln 2}} \tag{3.19}$$

where B_0 denotes the 6-dB bandwidth, and B_{OTF} represents the steepness of the filter edge. In the simulation, the B_0 and B_{OTF} are set to 45.34 GHz and 8.8 GHz, which is close to the specification of current commercial ROADMs for 50 GHz grid [83]. Figure 3-15(a) depicts the evolution of the normalized power frequency response as the number of cascaded ROADMs. The dependence of estimation errors of SNR_{linear}

and $SNR_{nonlinear}$ on the number of cascaded ROADMs with the LPs of -3 dBm, 0 dBm, and +3 dBm is shown in Fig. 3-15(b). It can be found that the proposed scheme is robust to the filtering effect of cascaded ROADMs. As the number of cascaded ROADMs increases, FO sweeping margin is reduced. In Fig. 3-15(c), it is shown that the optimum upper limit of FO sweeping decreases with the number of cascaded ROADMs. The relationship between values of (A_1, A_2, B_1, B_2) and the number of cascaded ROADMs is also studied. As shown in Fig. 3-15(d), the absolute values of A_1 and A_2 increase with the number of cascaded ROADMs. This phenomenon is due to the steepness of the signal spectrum edge increases with narrow filtering, resulting in a higher A in the left part of Eq. (3.17). On the contrary, B_1 and B_2 decreases with the number of cascaded ROADMs because, after narrow filtering, the noise distributed at the signal spectrum edge is suppressed while the central part of the signal spectrum where the signal power is much larger than noise power, suffers less impact. Therefore, SNR_{meas} increases and thus a lower $1/SNR_{meas}$ is resulted in in the left part of Eq. (3.18). Overall, in order to adapt to more heterogeneous conditions and meshed optical links with the various number of WDM channels and cascaded ROADMs, the parameters in the proposed method need refitting to maintain the monitoring performance. The generalizability of the proposed scheme should be further improved which is left for future study.

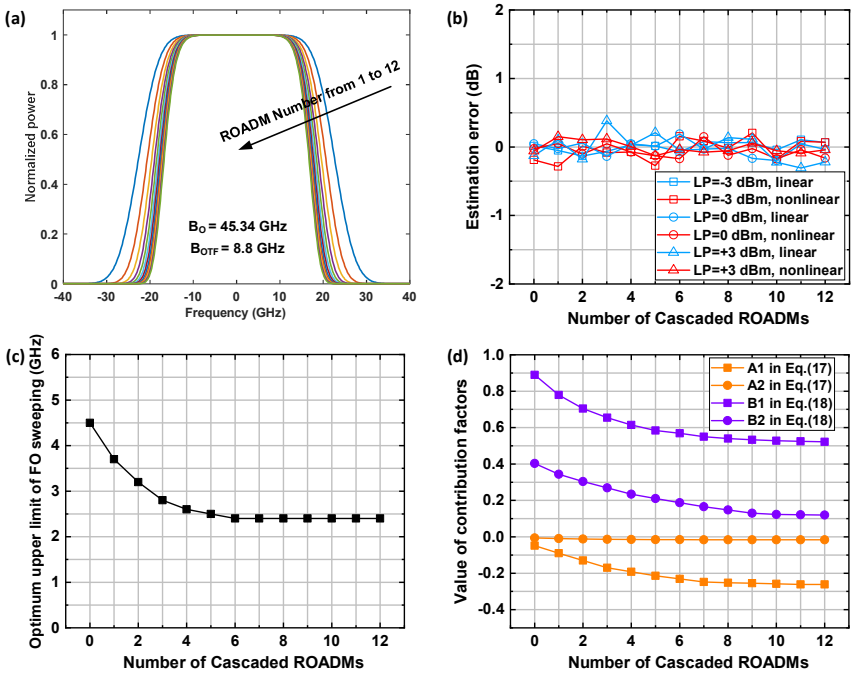

Fig. 3-15. (a) Normalized power frequency response with 1 to 12 cascaded ROADMs. (b) Estimation errors versus the number of cascaded ROADMs with the LPs of -3 dBm, 0 dBm, and +3 dBm. (c) The optimum upper limit of FO sweeping and (d) the values of contribution factors in Eq. (3.17) and Eq. (3.18) versus the number of cascaded ROADMs. Single-channel 16-QAM signal with the ROF of 0.5 is simulated.

3.5 Experimental Verifications

To further verify the performance of the proposed joint linear and nonlinear noise monitoring scheme, experiments are conducted for a 28 GBaud PDM-16-QAM WDM transmission system with a 915 km real link consisting of 12 SMF spans with different lengths and EDFAs, as shown in Fig. 3-16. Different from loop-based structure, such setup is very close to practical heterogeneous optical transmission link. The automated control system of the experiment setup is established with the abilities to set and monitor the system parameters, i.e. input/output (I/O) power at transceiver sides and each EDFA node fast and accurately. By such automated operations, the input power launched into each span of fiber can be accurately controlled. Meanwhile, EDFA's gains and attenuations are accurately adjusted to compensate for the fiber loss. At the

Tx, up-to-7 channels are divided into odd and even channels. 2 independent 28 GBaud 16-QAM digital waveforms shaped by raised cosine filter with ROF of 0.5 are generated offline and loaded into 84 GSa/s AWG. The generated waveforms from the 4 output ports of the AWG then drive the odd and even channels separately. The launch power is adjusted from -3 dBm to 3 dBm per channel by the EDFA used as the pre-amplifier. The 2 modulated tributaries are then interleaved and go into a PDM emulator before launching into the 915 km fiber link. Each span is followed by a 4 nm optical filter to filter out-band ASE noise.

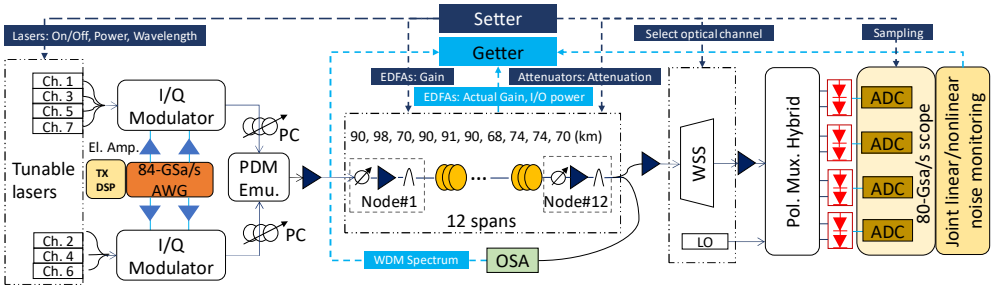

Fig. 3-16. Experimental setup of PDM 28 GBaud 16-QAM WDM system. WSS: wavelength selective switch; LO: local oscillator; PDM Emu: polarization-division multiplexing emulator.

At the receiver-side (Rx), after coherent detection, the linear and nonlinear noise estimation is operated in offline DSP. To correctly evaluate the performance of our proposed monitoring scheme, there are three steps that need to be carefully followed: (1) Reference linear noise is consisting of EDFAs-induced ASE noise and transceiver-induced electrical noise [70]. Therefore, optical B2B transmission is firstly conducted to obtain the reference background electrical SNR. For received signal in B2B condition, "quasi-perfect" DSP is performed, i.e. training symbol-assisted equalization and CPR to avoid DSP-induced noise as much as possible. For 915-km link transmission, at the Rx, EDFAs-induced SNR is calculated by conventional out-of-band measurement in the spectrum from OSA. Different from OSNR measurement

criteria, the reference noise bandwidth should be equal to that of the signal spectrum rather than 0.1 nm [70]. Reference SNR_{linear} can then be calculated according to the above two SNR measurements.

(2) Reference nonlinear noise should be calculated using the GN model in integration-form rather than closed-form ones, because the spectrum of the signal is not rectangular, and the lengths of spans are non-uniform. The incoherent GN model in [28] is used to calculate reference $SNR_{nonlinear}$.

(3) In the experiment, the FO is unavoidable due to the wavelength mismatch between LO and the transmitter laser. Since our proposed scheme is based on FO sweeping within the spectrum, a coarse FO compensation (FOC) is required. Fortunately, after CDC, FFT-based FOE scheme can be used to estimate FO accurately for the most commonly used formats is adopted in our scheme. Actually, based on the proposed FO sweeping principle, the FOE can also be realized by fitting the central axis according to the relation between $\hat{S}_x^{\alpha_0}(f)$ and FO, which can be efficiently integrated into our scheme and is left for future study.

Figures 3-17(a)-3-17(b) show SNR_{linear} and $SNR_{nonlinear}$ monitoring results compared with reference SNR curves, indicating that the feasibility of the proposed scheme is verified well by experiments. The estimation error curves are also provided in Fig. 3-18. Due to the gain budgets of EDFAs in experiments, the adjustable launch power range is limited within -3 dBm to 3 dBm where the estimation errors of SNR_{linear} are all less than 0.3 dB, which are quite accurate. On the other hand, the estimation errors of $SNR_{nonlinear}$ can be as large as 2.4 dB under the launch power of -3 dBm. It is attributed to inaccurate parameter information of the whole 12 optical fibers. Some of the used

fibers are old and there may exist some parameter uncertainties, e.g. CD and nonlinear coefficients, which may cause the inaccurate calculation of reference $SNR_{nonlinear}$ using GN model [61]. Overall, the estimation performance is satisfying for most conditions. It is noted that with accurate SNR_{linear} estimation, the equivalent OSNR monitoring with the same accuracy can be realized [85].

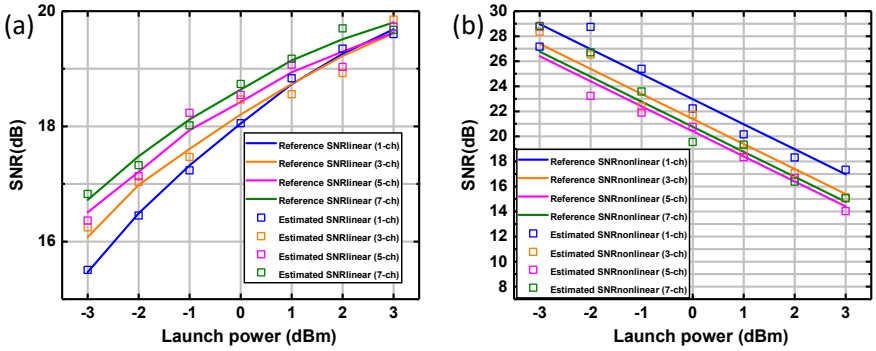

Fig. 3-17. Experimental (a) SNR_{linear} monitoring and (b) $SNR_{nonlinear}$ monitoring performance for 1-, 3-, 5-, and 7-ch conditions.

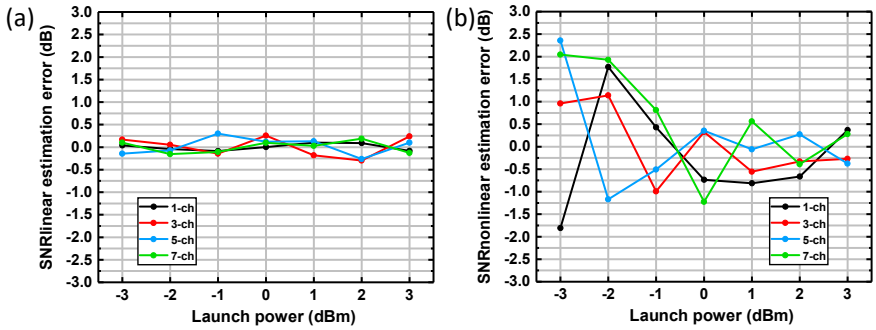

Fig. 3-18. Experimental (a) SNR_{linear} monitoring and (b) $SNR_{nonlinear}$ monitoring estimation error for 1-, 3-, 5-, and 7-ch conditions.

3.6 Summary

A joint linear and nonlinear noise estimation scheme is proposed based on spectrum analysis. The proposed scheme is modulation format-transparent and without DSP-induced noise. High estimation accuracy over a wide launch power range for single-channel and WDM transmission systems with various parameter settings are verified by both simulations and experiments over a real long-reach optical path link.

Chapter 4

QoT Estimation Based on Machine Learning and Analytical Models and Their Performance Comparisons

In this Chapter, a comprehensive comparative study of QoT estimation for WDM systems using ANN-based ML models and GN model-based analytical models is carried out. To obtain the best performance for comparison, all the system parameters for GN-based models are optimized in a brute-force manner. For ML models, the number of neurons, activation function, and number of layers are optimized. In simulation settings with perfect knowledge of system parameters and communication channels, GN-based analytical models generally outperform ANN models even though GN models are less accurate on the side channels due to the local white noise assumption. In experimental settings, however, inaccurate knowledge of various link parameters degrades GN-based models and ML generally estimates the QoT with better accuracies. However, ML models are temporally less stable and less generalizable to different link configurations. Potential network capacity gains are also briefly studied resulting from improved QoT estimators and reduced operating margins.

4.1 Introduction

Next-generation optical networks are expected to be highly flexible elastic optical networks (EONs) and have the ability to make full use of physical-layer and time resources to maximize network transmission capacity. A key enabler to EONs is dynamic lightpath provisioning, baud rate, modulation format, and shaping factor adaptation based on QoT where the SNR of each channel is estimated. Current optical networks incorporate large operating margins including unallocated, system, and design margins [31] in order to ensure that the planned demand capacity is met as well as to guarantee service level agreements (SLAs). However, the drawback of such a conservative approach is that it results in network over-dimensioning for both green-field and brown-field scenarios [31]. In this context, low-margin optical networking has gained a lot of attention recently in which a key enabler is accurate QoT estimation [86]. However, in WDM and heterogenous dynamic link environments, the parameter uncertainties and fiber nonlinear distortions render QoT estimations a non-trivial task: the SNR estimation of one channel actually depends not only on the linear accumulation of ASE noise from inline EDFAs but also on the signal power and light path of all channels in a complicated manner and all the parameters are subject to a certain level of uncertainty.

Over the past few years, several classes of approaches for QoT estimation in optical networks have been proposed where the estimation of linear as well as nonlinear impairments are incorporated. These approaches can be broadly classified into three main types [87]: (1) Full fiber propagation simulation models using split-step Fourier method (SSFM) [32] to obtain accurate QoT estimations. These approaches typically involve high computational complexity (and hence require more computation time) and thus are undesirable for real-time deployment in large and dynamic optical networks; (2) Analytical formulas such as GN models

[28, 33] in which the accuracy increases with model complexity, and are much more scalable and computationally simpler than SSFM models; (3) ML-based approaches [34-35, 88] that learn the relationships between monitored field data and the SNR of already deployed lightpaths to predict the QoT of unestablished lightpaths.

GN models have been intensely investigated and generally offer an acceptable, although not as accurate as full simulation models, estimation performance with moderate computational complexity [28, 33]. The GN model is based on numerical integration to obtain nonlinear interference (NLI) and has been the most commonly used [28]. It typically requires a computation time of a few minutes per WDM channel [28, 33], accumulating to a few hours for full WDM systems consisting of several hundreds of channels. Incoherent GN (IGN) and local white noise (LWN) assumptions of the NLI are common approximations to reduce the computation efforts with a reasonable accuracy penalty. However, such time frames may still be too long for real-time network applications and closed-form approximations that can complete QoT estimations essentially in real-time are required [36]. Although some of the closed-form approximations offer comparable accuracy with numerical integration under some limitations, estimation accuracy for heterogenous links and WDM channels with non-rectangular spectral shape and Nyquist-WDM configurations still needs to be improved [36]. Another shortcoming of analytical model-based performance prediction is that the uncertainties of link parameters, e.g., inaccurate measurement of optical power, span length, loss and CD parameters, and particularly NF of each EDFA and electrical non-idealities at the transmitter and receiver might lead to further degradations in QoT estimation [60-61, 70].

In a parallel development, ML-based QoT estimation has gained significant attention recently since it can effectively learn and discover hidden relations in large amounts of data

from large dynamic optical networks [89]. Several ML-based QoT estimation techniques have been proposed in the literature, such as ANN [90], support vector machine (SVM) [90], K-nearest neighbors (KNN) [90], random forest [9], etc. These works mainly predict whether the QoT of the lightpath under investigation is above or below a certain threshold. However, for realizing low-margin network operations, ML-based QoT estimation techniques that can accurately quantify the QoT of lightpaths in terms of actual SNR, *Q*-factor, bit error ratio (BER), etc. are more desirable. This can enable the network operators to get accurate information about the residual margin and thus avoid network over-dimensioning. While both analytical model-based and ML-based QoT estimation tools are increasingly being considered in optical networks, there are a number of issues yet to be addressed: (a) The uncertainties of link parameters are common in deployed links and greatly affect the accuracy of analytical models. Simple and effective methods to mitigate such effects need to be developed; (b) It is not clear how the QoT estimation accuracy of ML-based methods compares with that of traditional well-established analytical model-based approach. To maximize the transmission capacity of optical networks, the reduction of operating margins is important and it partially depends on the accuracy of the QoT estimation tool; (c) In principle, any ML-based QoT estimator is tailored for the link configuration where data is obtained and is not guaranteed to perform well in other links of a network, thus requiring time-consuming re-training and/or data re-collection. Therefore, it remains to be seen how the ML models can flexibly adapt themselves to estimate QoT in practical heterogeneous networks with different transmission link scenarios with minimal efforts; (d) As QoT estimation needs to be constantly performed in practical optical networks, the stability of ML-based QoT estimation approach over long periods of time needs to be studied and compared with that of GN-model based approaches.

Recently, some hybrid schemes which combine analytical model and ML method together were studied. In [59-60, 91], ANN models are adopted to better estimate the input parameters of the analytical models. However, in some scenarios where the amount of available dataset is limited, it may be more difficult to use those hybrid strategies since ML models perform well only when sufficient dataset is available and simpler methods are desirable. Therefore, different choices of analytical and ML techniques and hybrid approaches may be needed for various application scenarios.

In this Chapter, a more detailed simulation and experimental comparison study between optimized GN model-based analytical models and the ANN-based ML models for QoT estimation in WDM systems in the presence of nonlinear distortions is conducted. The analytical and ANN models are separately optimized in the following ways: for analytical models, different realizations of the IGN model are studied ranging from the simplest closed-form approximation to the most complex numerical integration with the high frequency resolution and no LWN assumption. To obtain optimal performance for analytical models, a brute-force multi-dimensional sweep of key system parameters is performed. By comparing GN models with various complexity, it is shown how simpler and more practical GN-based analytical models will produce more nonlinear interference estimation errors at the side channels and how it affects the accuracy of QoT estimation. For ANN models, 1-, 2-, and 3-hidden layers are studied where the number of hidden neurons and activation functions are all optimized in an exhaustive fashion. In simulation environments with perfect knowledge of parameter values, our results show that analytical models generally outperform ANN models in terms of the standard deviation (std) of QoT estimation errors. Larger-scale experiments with a larger dataset are conducted and signal power control and stability are improved for

training the ML models and optimizing the analytical model parameters. Experimental results show that ML models generally provide better estimation performance than analytical models. On the other hand, analytical models can easily adapt to different transmission scenarios while more data for re-training and fine-tuning are required for applying pre-trained ML models to a wider set of link configurations. Furthermore, ML models are also found to be less stable with time and the temporal changes in experimental settings which generally have an adverse impact on model estimation accuracy. Finally, potential network capacity gains are briefly studied for links that can switch to a higher modulation format to capitalize on a reduced margin enabled by more accurate QoT estimators.

4.2 Analytical and Machine Learning Models Based QoT Estimators Designs and Optimizations

In this Section, the analytical models and ML models used in our QoT estimation will be discussed in detail. To ensure a fair comparison between different models, the same simulations are conducted, and the same experimental dataset is used. The data is also processed with the same set of DSP to obtain the same SNR estimates. The minimization of QoT estimation error for analytical and ML models is performed for each channel independently. In both simulations and experiments, hundreds of independent random signal sequences with more than 10000 symbols are transmitted over the fiber link. For each received sequence, an SNR estimate is calculated using EVM and a corresponding estimation error when compared to the output from the ML or analytical models. In this way, hundreds of independent estimation errors are

obtained from which the standard deviation σ_{QoT} of the QoT estimation errors for a particular channel is calculated.

4.2.1 Parameter Calibration Assisted Analytical Models Design

For analytical QoT estimation models, the overall noise and hence SNR of a channel is considered to be contributed by ASE noise and NLI so that the SNR of the optical channel is given by $P_S/(\sigma^2_{NLI}+\sigma^2_{ASE})$ where P_S denotes signal power. To calculate the NLI power $\sigma^2_{NLI}=\int G_{IGN}(f)df$, the IGN model [28] is used to calculate the power spectral density (PSD) $G_{IGN}(f)$ of the NLI, which is obtained from summing up the NLI PSD incurred from each span.

$$G_{IGN}(f)=\sum_{n=1}^{N_S} G_{NLI,n}(f) \tag{4.1}$$

where N_s is the total number of spans and $G_{NLI,n}(f)$ is the NLI PSD of the n^{th} span

$$\begin{aligned} G_{NLI,n}(f)==&\frac{16}{27}\gamma^2\int_{-\infty}^{\infty}\int_{-\infty}^{\infty}G(f_1)G(f_2)G(f_1+f_2-f) \\ &\times\left|\frac{1-\exp(-2\alpha L_n)\cdot\exp(j4\pi^2\beta_2 L_n(f_1-f)(f_2-f))}{2\alpha-j4\pi^2\beta_2(f_1-f)(f_2-f)}\right|df_1df_2 \end{aligned} \tag{4.2}$$

where $G(f)$ is the signal spectrum, L_n, α, β_2, and γ are length, attenuation, dispersion, and nonlinear coefficients of the n^{th} span, respectively. The IGN model is known to closely approximate the GN model for practical systems with many WDM channels and the estimation performance is relatively accurate [28]. A further approximation is the LWN assumption in which the NLI spectrum is assumed to be flat across the signal bandwidth, i.e., $G_{NLI,n}(f)\approx G_{NLI,n}(0)$. Although among the integral-form GN models, the IGN model is not as accurate as the enhanced GN (EGN) model [33], it is still the most popular model so far

taking both good estimation accuracy and moderate computational complexity into account. A closed-form expression of the GN model [36] is also studied to calculate σ_{NLI}^2, which is flexible and can account for arbitrary launch power distributions and heterogeneous fiber spans. The ASE noise power induced by EDFAs is calculated as $\sigma_{ASE}^2 = \sum_{n=1}^{N_S} NF_n(G_n - 1)h\nu B_{signal}$, where NF_n and G_n are the noise figure and gain of the n^{th} EDFA, h is Planck's constant, ν is the center frequency of the channel and B_{signal} is the signal bandwidth [11]. The transponder is assumed to be ideal in our simulation. In experimental settings, however, additional transceiver noise with variance σ_{TRx}^2 is present. Since the ML models can be trained using dataset without perfect knowledge of optical parameters and their interactions, to guarantee a fair comparison, the key issue of system parameters uncertainties is needed to be addressed when applying analytical models for QoT estimation (e.g., uncertainties in L_n, α, β_2, and γ, NF_n and G_n etc. In this connection, 10% of the received data is randomly selected out and performed a multi-dimensional brute-force sweep of the parameter values to minimize the std of the QoT estimation error σ_{QoT} across the whole dataset. The sweeping process is divided into two steps: (1) the NF is swept from 70% to 130% of its true value to minimize σ_{QoT} (2) a 4-dimensional sweep of attenuation, dispersion, nonlinear coefficients, and lengths of fibers (also from 70% to 130% of their true values). After parameter optimization, the mean error is also estimated and subtracted from the rest of the data so that the estimated SNR is unbiased with zero mean error. In addition to addressing parameter uncertainties, it is also shown that the parameter optimization process also serves to partially compensate the NLI estimation error resulting from imperfect GN models. In particular, when there are NLI estimation errors, the NFs in the sweeping process will be adjusted away from their true values

to offset such errors and achieve a better QoT estimation performance over the whole dataset. Finally, one should note that since the GN model is perturbative approach, which is a first-order NLI model, the validity range of the proposed analytical models is restricted to the low-nonlinearity regime, which is the most relevant in practice.

4.2.2 ANN Based ML Models Design

In this work, feed-forward ANNs are selected among various classes of supervised ML models proposed in the literature for comparison with analytical models. This is mainly because (i) ANNs are the most common ML models used in QoT estimations; (ii) ANNs are extremely powerful architectures with great expressive power and it is known (through the universal approximation theorem [90]) that even a single hidden layer ANN with proper nonlinearities, adequate number of neurons and appropriate training can approximate any continuous function in principle. Moreover, once adequately trained, ANNs with more hidden layers can generally yield even better performance and thus can be considered as a good benchmark for performance limits of common ML models.

In simulations, separate ANN models are used to estimate the QoT (in terms of SNR) of individual WDM channels. ANNs with 1-, 2-, and 3- hidden layers are studied where the set of input parameters $\boldsymbol{\theta}$ consists of signal launched powers (LPs), amplifiers' gains and NFs, and input power at each span while the SNRs of various WDM channels after signal recovery by various DSP blocks are the ANN targets. The ANNs' output layer contains only one neuron and the mean square error (MSE) is used as the loss function. A multi-dimensional grid search-based approach is used for optimizing the number of neurons in each layer of the ANN. For 1-hidden-layer ANN, it is optimized over a

range from 1 to 80 hidden neurons to minimize the MSE. For 2- and 3-hidden-layers ANNs, a 2- and 3-dimensional sweep are conducted from 1 to 40 neurons in each hidden layer to determine the optimal ANN configuration that minimizes the MSE. It is also chosen between ReLU or sigmoid activation function for the hidden layer neurons to optimize the MSE. A linear activation function is chosen for the output layer.

The training and testing datasets are obtained by randomly choosing 75% and 25% of the overall dataset (from simulations or experiments) respectively. During the training phase, 20% of the training data is used as validation dataset in order to prevent over-training of the ANNs and thus improve their generalization ability. Note that the random partitioning of overall learning data into training (80%) and validation (20%) data is used. During the course of ANN training, the validation data test is used to constantly examine ANN's error performance and enforce an early termination of the training process if the validation dataset gives large errors [92, 93]. Such a regularization approach ensures that the ANN models are not over-trained. During testing, the vectors of link parameters $\boldsymbol{\theta}$ are the input to the ANN, and the corresponding output SNR estimates for different WDM channels are compared with the true SNR values and the std of the estimation errors are then computed.

4.3 Simulation Study and Comparisons

28 GBaud PDM 16-QAM with 7-, 11- and 15-WDM channels are studied through simulations. The system length is 800 km with 8 combinations of SSMF span and EDFA. The SSFM is used to emulate the fiber model. The EDFA gains are set to fully compensate the fiber span loss. Raised cosine pulse with 0.1 roll-off factor is used and an ideal rectangular low-pass filter with bandwidth (1+0.1)×28 GHz is used at the receiver to filter out the out-of-band noise

(It has also been studied root raised cosine pulse shaping at the transmitter and matched filtering at the receiver and nearly identical SNR values are obtained). The channel spacing is 50 GHz. Signal LPs are the same across different channels and together they vary from -3 dBm to 3 dBm. The NF of each EDFA is randomly set to 5 dB or 6 dB. LP is an important parameter that directly determines the SNR imposed by ASE noise and by nonlinear noise. Meanwhile, since the EDFA gain is set to fully compensate the span loss, the gain value of one EDFA is indicative of the length of the previous fiber span. Therefore, the EDFA gain should be one of the input parameters to the ML model. Also, NF depends, in principle, on other factors such as spontaneous emission factor, amplifier length, and pump power of the EDFA. Due to the reasons above, channel LPs, EDFA gains, and NFs are the most relevant input parameters to ML models. In total, 7000 data points are collected corresponding to different combinations of channel LPs and NFs for each individual channel of the three scenarios considered in our simulations. After propagation over the 800-km fiber link, the accumulative CD is sufficient for the Gaussian assumptions for both signal and nonlinear noise to hold [28, 33], thus validate the applicability of the GN models to estimate NLI power. In our SSFM simulation, as there are no additional impairments (e.g. transceiver noise, IQ imbalance, frequency offset, phase noise, etc.) other than fiber propagation effects induced nonlinear interference and ASE noise, the DSP flow used consists of CD compensation and 2x2 multi-input-multi-output (MIMO) filter for polarization demultiplexing and PMD compensation. These algorithms are not expected to induce SNR penalties. Therefore, the overall noise from simulations consists of the ASE noise and NLI only. In addition, even though there are no parameter uncertainty issues in simulation studies, the multi-dimensional parameter optimization process aforementioned is conducted so as to partially offset the NLI estimation error by GN models.

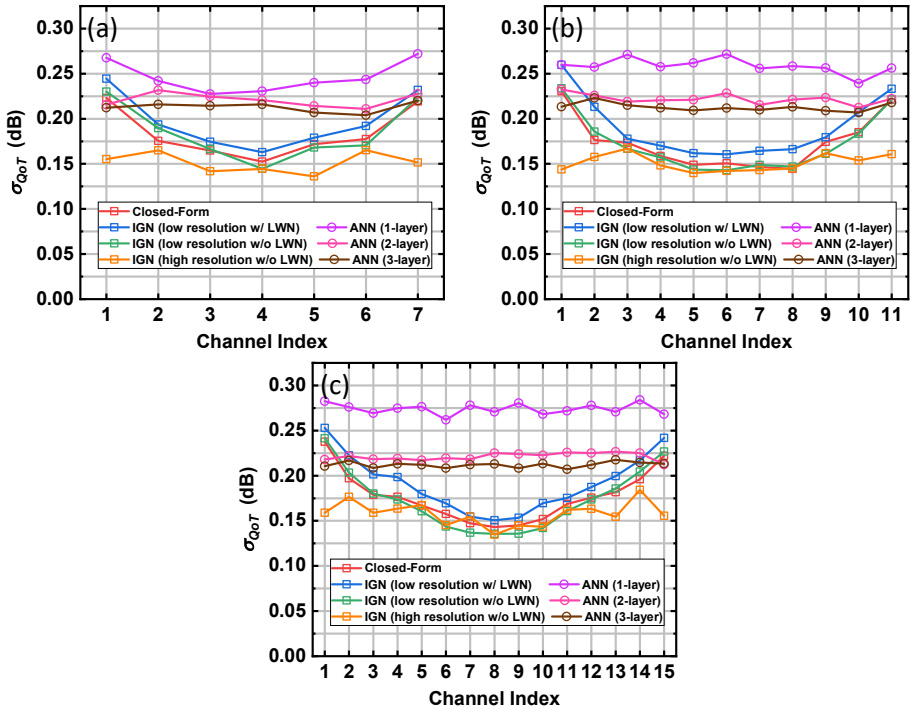

Fig. 4-1. Standard deviation of QoT estimation error σ_{QoT} using various versions of ANN models and GN-based analytical models for a (a) 7-channel (b) 11-channel and (c) 15-channel WDM system.

Fig. 4-1 shows the std of QoT (characterized by SNR) estimation error σ_{QoT} for all channels using various versions of GN models and ANNs with the different number of hidden layers. IGN models with different degrees of accuracy and approximations are studied. For the high-resolution IGN model, 500 frequency bins are used to numerically calculate σ_{NLI}^2 over the channel spacing of 50 GHz while low resolution uses 50 frequency bins. For the low-resolution version IGN model, the LWN assumption is further made to decrease the computational complexity. The closed-form GN model is also studied for comparison. It can be seen that the σ_{QoT} for all channels are lower than 0.3 dB for all the methods considered, and the analytical models generally outperform ANN models. For ANN models, σ_{QoT} decreases with more hidden layers but the improvements from 2-layer to 3-layer ANN are

quite limited. This indicates that optimal ANN performance has been reached and there is little value to further increase the number of hidden layers or number of neurons.

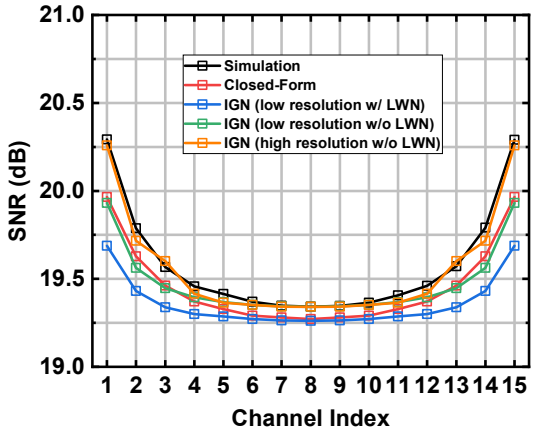

Fig. 4-2. Estimated SNR using various GN-based analytical models for a 15-channel WDM system with LPs of 0 dBm.

Generally, high-resolution characterization of the input signal spectrum to the IGN model provides better NLI estimates than low-resolution characterization. However, it is observed in Fig. 4-1 that the IGN model with low resolution outperforms high resolution for a few cases. This phenomenon is attributed to the fact that the IGN model itself not a perfectly accurate models nor a lower/upper bound for NLI estimation. Therefore, the high resolution does not automatically imply high accuracy. In some cases, the low-resolution characterization may partially "correct" the inaccuracy of the IGN model itself when the two errors are opposite in sign. Nevertheless, in most cases, the IGN model with high resolution and without LWN assumption provides the most accurate estimation performance. For other GN models studied, σ_{QoT} is lower at center channels compared to the side channels. To understand this phenomenon, Fig. 4-2 compares the estimated and true SNRs for all channels for a 15-channel WDM system with the signal LP of 0 dBm. It can be seen that the IGN model with high resolution and without LWN assumption produces the most accurate SNR estimation across all channels and among all the GN models studied. For the IGN model with low resolution and

LWN assumption, the SNR value will be underestimated, especially for side channels. The closed-form GN model performs similarly for the side channels but under-estimates the SNR at the center channel. This phenomenon is attributed to the fact that both the IGN model with LWN assumption and closed-form GN model assume a flat NLI PSD, e.g. LWN assumption, within the signal bandwidth. As pointed out in [36], the LWN assumption will over-estimate the nonlinear distortions, especially for outermost channels. An over-estimation of NLI thus leads to under-estimation of overall SNR.

If the GN model can estimate NLI perfectly, there is no need to optimize NF or other parameters. Unfortunately, due to the over-estimation of NLI, when sweeping for the best NF to minimize σ_{QoT} over the whole dataset, the optimal NF will be lower than the true value in order to offset the NLI over-estimation and bring the estimated SNR closer to the true SNR. For received signals with different channel LPs, there should also exist different optimum NFs since the proportions of σ_{NLI}^2 and σ_{ASE}^2 is related to channel LPs. However, although a part of received data with various LPs is used for the optimization process described above, finally only one optimized NF is obtained. Consequently, it in turn increases the overall spread of SNR estimation errors over the whole dataset and that is why σ_{QoT} increases with NLI over-estimation.

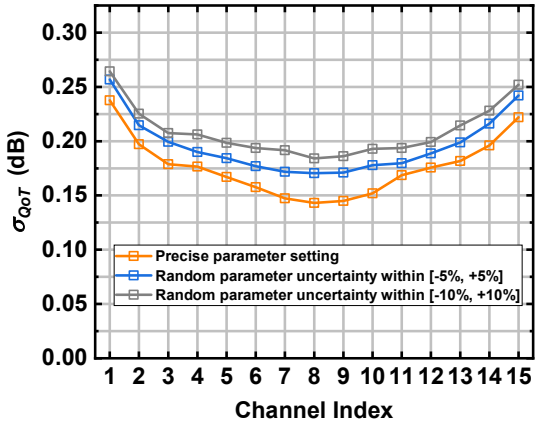

Fig. 4-3. Standard deviation of QoT estimation using GN-based analytical models with different levels of parameter uncertainties.

The effects of parameter uncertainty on σ_{QoT} for GN models are also studied. Specifically, the parameters L_n, α, β_2, and γ, and NF of each EDFA in the analytical models are made to randomly deviate within $\pm 5\%$ and $\pm 10\%$ from their true values and the corresponding σ_{QoT} are shown in Fig. 4-3. It can be seen that σ_{QoT} at the center channels are most sensitive to parameter uncertainty. In our proposed scheme, the parameter sweeping process addresses the uncertainty issue and is necessary to achieve good QoT estimation accuracy using analytical models in practice.

Finally, it should be noted that while present network dynamics do not change at a speed that requires second-by-second real-time QoT estimation, one should still be aware of the estimation time required for different implementations of the GN model. In our 15-channel simulation, IGN with high resolution without LWN assumption takes 15 hours to compute on a PC with intel CORE i7-8550U CPU. For low-resolution IGN without LWN assumption, it takes 2.5 minutes while only 5 seconds are needed for low-resolution IGN with LWN assumption. For the closed-form GN and ANN models, the processing practically takes no time and they can meet potential real-time requirements which may arise in the future. Note

that we only count the testing time and not the training time of ANN models in the discussions above as the ANN models are assumed to be trained offline.

4.4 Experimental Study and Comparisons

The experimental 7-channel WDM setup is shown in Fig. 4-4. An automated system is built to monitor various parameters including the signal powers, attenuations and gain at transmitters/receivers, and each EDFA node as shown in Fig. 4-4(a). At the Tx, 2 independent 28 GBaud 16-QAM digital waveforms shaped by raised cosine filter with 0.1 roll-off factor are generated offline by Mersenne Twister generator to produce pseudo-random sequence with the length of 65536 symbols and loaded into a 112 GSa/s AWG. The 4 generated independent waveforms then drive the odd and even channels separately with up to 7 ECLs with 100 kHz linewidth. The power of each laser is independently varied in the range from -8 dBm to +4 dBm and the empirical distribution of signal LPs for each channel is shown in Fig. 4-4(b). For a specific channel, the sensitivity of QoT to power variations of each adjacent channel will be reduced when the number of channels increases but the SNR of the channel of interest depends on the combined nonlinear interference from other channels, self-phase modulation, and accumulated ASE noise. The nonlinear interference is related to power levels across all the channels and therefore the signal powers across all channels are important parameters that significantly influence the amount of linear and nonlinear impairments and the overall SNR of the channel of interest. The 2 modulated tributaries are then interleaved and go into a polarization division multiplexing emulator with a delay of 140 ns before launching into a straight-line fiber link of length 915 km, which consists of up to 12 spans of SSMF with different lengths as shown. Each span is

followed by an EDFA-tunable attenuator-4nm optical filter triplet to balance the launched power between each span.

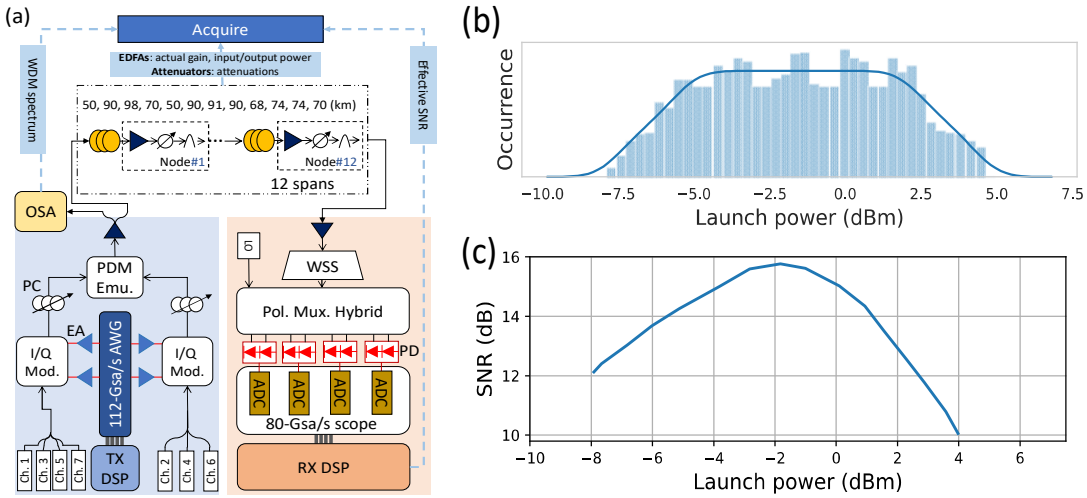

Fig. 4-4. (a) Experimental setup for comparing ML and analytical models for QoT estimation in WDM systems; WSS: wavelength selective switch; LO: local oscillator; PDM Emu: polarization division multiplexing emulator; (b) The empirical distribution of signal LP per channel in our study; (c) A case of SNR versus signal LP in our study.

At the Rx, data from channels 1, 3, 4, 5, and 7 are sequentially obtained by coherent detection using another ECL with 100 kHz linewidth as the LO. Each channel is first filtered by a WSS and sampled by an 80 GSa/s oscilloscope. The sampled signals go through standard DSP blocks including CD compensation, constant modulus algorithm (CMA)+radius-directed equalization (RDE) for polarization demultiplexing, 4th power algorithm for frequency offset estimation, extended Kalman filter for carrier phase estimation followed by effective SNR calculation. The mappings between effective SNR and system parameters $\boldsymbol{\theta}$ consisting of LPs, amplifiers' gains, and NFs, and total signal powers of each span are collected. Fig. 4-4(c) depicts a case of the estimated SNR vs. signal LP for channel 4, indicating that the data points obtained cover the linear and nonlinear regimes. In experimental settings, distortions originate from ASE noise, nonlinear impairments as well as certain transceiver impairments that cannot be

analytically accounted for. The collective noise power of these transceiver impairments can be experimentally measured in a B2B configuration [11, 94]. In this connection, B2B measurements are conducted to estimate the noise power of the collective transceiver impairments. This will be subtracted from the total estimated link noise so that only the linear and nonlinear noise remain for analytical and ML model fitting. In our experiments, data comprising a total of 11,520 data points (i.e., 2304 for each of the five channels considered) is collected. 75% of that data (i.e., 1728 data points for each channel) is used for the training of each ANN model while the remaining 25% (i.e., 576 test cases) is used for testing. During training, 20% of the training data (i.e. 346 test cases) is used as validation dataset to prevent over-fitting. For GN models, the experimental data are used to optimize the parameters through the multi-dimensional brute-force sweeping procedure described in Section 2B.

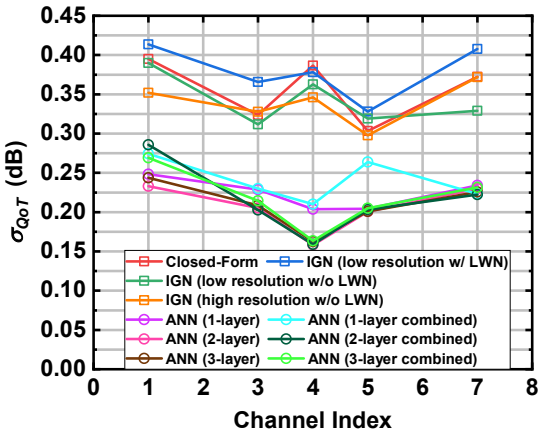

Fig. 4-5. Standard deviation of QoT estimation error σ_{QoT} using various ANN and GN-based models.

Transmission of 7-WDM channels is studied and the SNRs of channels 1,3,4,5 and 7 are monitored so that the center channel, side channel, and middle channel conditions are covered. Stability tests of our experimental setup are first conducted in which 50 sets of data for the same launch power configuration are obtained every 100 seconds.

The std of these 50 QoT estimates is around 0.1 dB, indicating good system stability. The QoT estimation performances of various channels using ML and analytical models are shown in Fig. 4-5. From the results, it can be concluded that ANN models generally outperform analytical models. Specifically, the σ_{QoT} using ML model are all smaller than 0.25 dB, while σ_{QoT} for analytical models generally exceeds 0.3 dB even though a sweeping process has been utilized to obtain the best possible parameter values. The worse performance of analytical models is attributed to larger parameter uncertainties and other unaccounted signal distortions in experimental settings. It should also be noted that for various versions of the GN model, σ_{QoT} results do not differ much and this is in contrast with simulation results where the high-resolution IGN model generally outperforms other lower-complexity models. This is also a consequence of parameter uncertainties and other unaccounted signal distortions. Therefore, the advantage of high complexity and high estimation accuracy models is weakened in experimental settings. Such phenomenon also occurs for ML models where the improvement of using deeper 3-hidden-layer ANN architectures is negligible in experiments which is in contrast with corresponding simulation studies. This can also be contributed by the following factors: Firstly, as compared to a shallow ANN, a deeper ANN architecture in general requires much larger training data [95], which is often lacking in optical transmission experiments. Secondly, since the acquisition of experimental data takes a few days in our case, slight changes in link operating conditions (such as lasers' output power fluctuations, EDFAs' gain variations, temperature, etc.) over such a long period may also degrade ANN models' accuracies.

In addition to using separate ANNs to estimate the QoT of individual WDM channels, the case where a single ANN is trained by the combined data of all 5 WDM channels under consideration is also investigated to jointly estimate the QoT of all these channels. The results in Fig. 4-5 for such combined 1-, 2- and 3-hidden layers ANN show that the estimation error of a few channels (e.g., channel 1 in case of 2- and 3-hidden layers ANN or channel 5 in case of 1 hidden layer ANN) increases considerably as compared to separate ANN models for each channel. This is expected since it is more difficult for a single ANN to jointly optimize the estimation performance of all 5 channels simultaneously compared to the use of separate ANNs for each individual WDM channel.

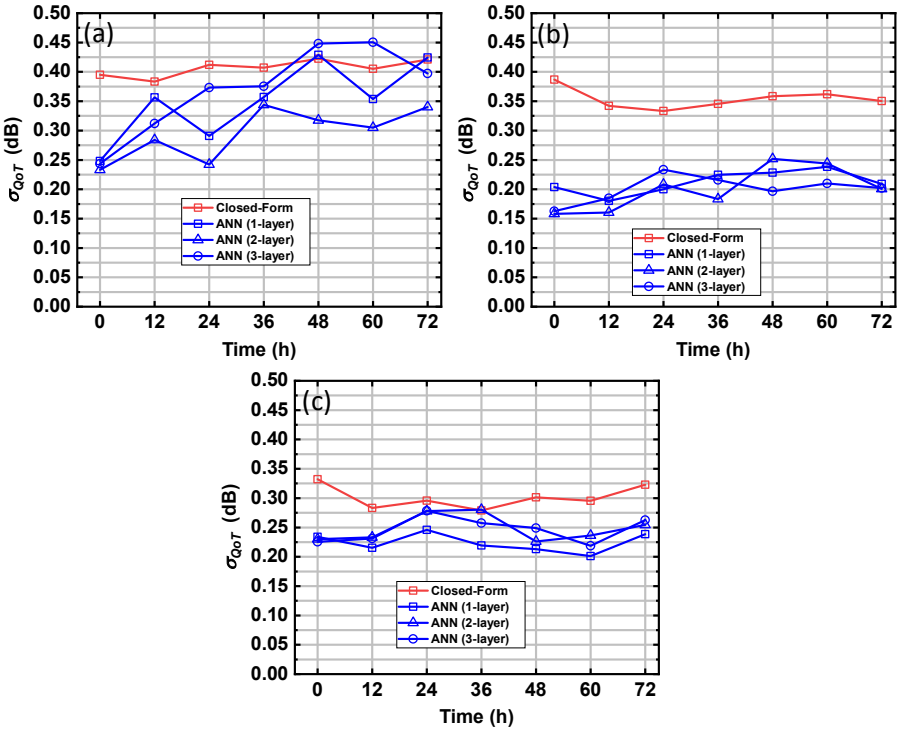

Fig. 4-6. Temporal stability of ANN models and closed-form GN model for (a) channel 1, (b) channel 4, and (c) channel 7.

To investigate the temporal stability of ML and GN-based analytical models, 7 identical datasets which are taken 12 hours apart from each other are obtained. The first

set is used to train the ML models and optimize analytical models which are then tested on the other sets. Here, since the closed-form GN model-based analytical model shows similar performance as other GN models studied, only the closed-form model is compared with ML models. The σ_{QoT} over time for channel 1, channel 4, and channel 7 are shown in Fig. 4-6(a)-4-6(c), respectively. It can be seen that ML models outperform analytical models most of the time as they have a performance gap to begin with. Nonetheless, for channel 1, the performance of ML models degrades considerably with time and eventually approaches closed-form GN models after 72 hours, indicating ML models' sensitivity to temperature variations and other environmental factors. ML models are at most as stable as and generally less stable than analytical models.

To further study the generalizability of different models to different link configurations, data for slightly varied link configurations by shortening the transmission link by 1, 2, or 3 spans is also obtained. The additional training datasets required for the trained ANN and analytical models to adapt to the new configurations are investigated and σ_{QoT} results for channel 4 are shown in Fig. 4-7. Closed-form based analytical model takes less than 15 data points from the new configurations to adapt. For ANN models, a reduction in the number of spans directly changes the size of the input parameter set $\boldsymbol{\theta}$ of the original ANN model and renders it unsuitable for the new link configuration and thus performs poorly without re-training. To address this issue, a transfer-learning-based approach is adopted as shown in Fig. 4-8, where the weights/biases of the originally trained ML models are tuned/adjusted using a small amount of new data from the reduced link configuration. Also, an input feature is set to 0 if it physically does not exist in the transferred domain. After using around 25 data

points from the new link configuration, ANN models can catch up with analytical models and outperform them after 50 data points. Similar conclusions can be drawn for 2- and 3-layer ANNs. Apart from the scenario discussed above, there are a number of other practical scenarios where transfer learning can be helpful. For example, in [61], the use of transfer learning is demonstrated in situations where the locations of a few EDFAs in a multi-span link are swapped. Similarly, in [88], the use of transfer learning is demonstrated to accurately predict QoT in target domain systems with different data rates, modulation formats, and fiber types from the source domain in which the ML model is trained initially.

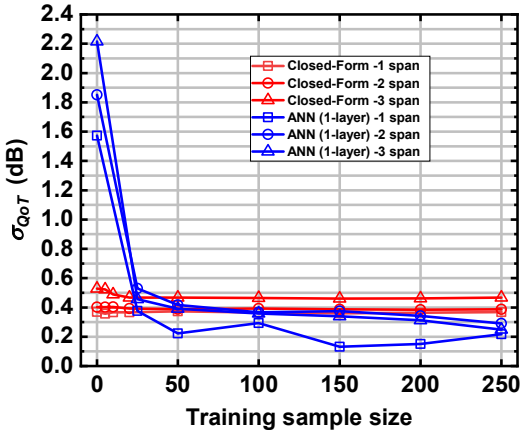

Fig. 4-7. Adaptation performance of 1-layer ANN and closed-form GN models to slightly different link configurations for channel 4.

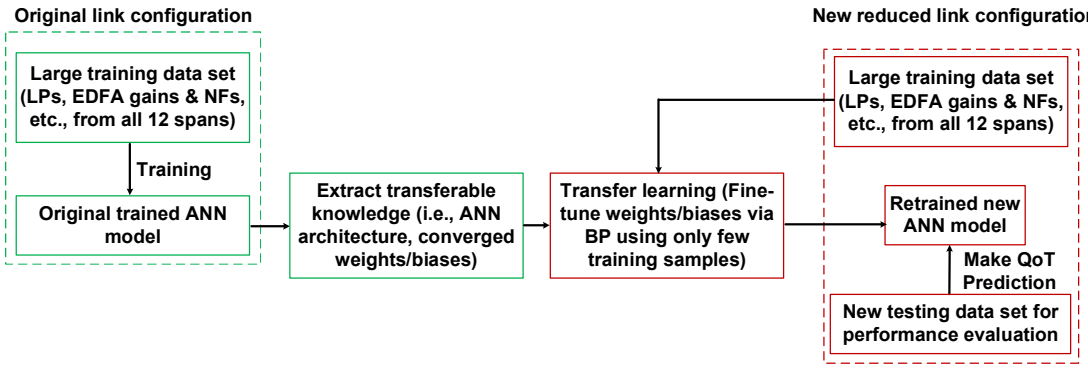

Fig. 4-8. Flow chart of ANN model adaptation using transfer learning approach.

4.5 Analysis on Margin Reduction and Capacity Improvements

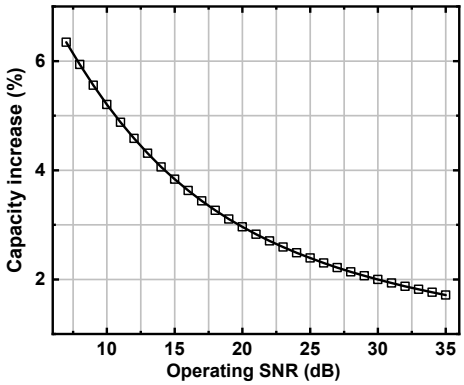

Fig. 4-9. Capacity increase by margin reduction of 0.6 dB assuming optimal constellation and shaping factor is chosen for each operating SNR to approach Shannon limit.

When designing optical networks, margins are allocated to cater for inaccurate QoT estimation among other factors during network planning and operation [96]. It has been analyzed [97] that a larger margin produces a larger performance penalty in optical networks of various scales. Margin reduction is especially important for large-scale and complex optical networks to avoid the large proportional reduction in throughput. Therefore, better QoT estimation methods can help reduce system margins and improve transmission capacities of optical networks. One way to quantify the amount of margin allocation due to imperfect QoT estimation is based on the std of the QoT estimation error σ_{QoT}. Specifically, it is assumed that the margin allocated to imperfect QoT estimation is 3 σ_{QoT} so that the true SNR of the channel is above the allocated margin for 99.85% (i.e., 3σ) of the time. If the center channel of our experimental QoT estimation results is taken, the difference between the best ML model and the best GN model is about 0.35-0.15 = 0.2 dB. Hence, a margin reduction of 3×0.2=0.6 dB can be achieved by replacing the analytical model by the ML model for a better QoT estimation accuracy. Assuming network operation predominantly in the linear and quasi-linear region, a margin reduction of 0.6 dB directly enables an increase of signal launched power and operating SNR

by 0.6 dB, which in turn approximately translates into an information-theoretic capacity increase of $\log_2(1+SNR\times 10^{\frac{0.6}{10}})-\log_2(1+SNR)\approx 0.2$ bits for SNR > 10 dB. In principle, one can use optimized modulation formats and constellation shapes for each SNR value to maximize the achievable information rate towards information-theoretic capacity [98]. Figure 4-9 shows the corresponding capacity increment as a function of the SNR in which the system operates. In practical network settings, the average capacity improvements further depend on 1) the statistical distribution of operating SNRs in the network, which can depend on, among other factors, the distribution of link lengths of the network concerned; 2) Current flexible-rate transceivers use a discrete set of modulation formats so that information-theoretic capacity cannot be achieved for all SNR values. Figure 4-10 shows the adopted modulation formats for SNR ranging from 7 dB to 32 dB with various allocated margins. A BER of 2E-2 is taken as the threshold for the case of 'no margin'. Note that when the SNR is within the ranges $R_1, R_2 \cdots R_7$ as shown, the reduced margin will trigger transmission of a higher-order modulation format, thus increasing capacity. The average capacity increase is given by $\sum_{n=1}^{7} P(R_n)\cdot(\frac{n+1}{n}-1)$ where $P(R_n)$ denotes the probability of link SNR falling in the range R_n. Therefore, the SNR distribution of all paths in the optical network plays a role in the average capacity increase enabled by better QoT estimation techniques. As an illustrative example, if a uniform SNR distribution from 10 dB to 30 dB is assumed and conventional unshaped QAM with 1, 2, 3…8 bits per symbol, the averaging capacity increase rate is 7.78% assuming a 0.6 dB margin reduction due to a more accurate QoT estimator. It should be noticed that, for our experimental results, a margin reduction of 0.6 dB can be achieved for the center channel, while for other channels the margin reduction will be different. The wavelength-

dependent nature of QoT estimators and margin reduction should be taken into account when designing low-margin networks.

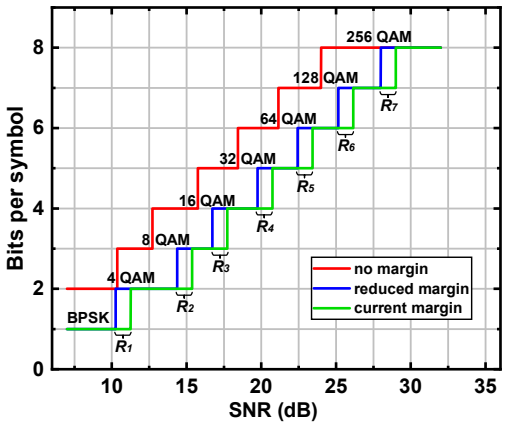

Fig. 4-10. Supported modulation formats vs SNR with different amount of margin conditions for a BER threshold of 2E-2.

Finally, it should be noted that while the capacity improvement shown is modest, direct link capacity improvement enabled by the reduced margin is one of many envisioned benefits of accurate QoT estimation in future network operations. Accurate QoT estimation also helps accurate link power engineering, improve link margin reliability, and enable optical path restoration in future ROADM-based mesh optical networks.

4.6 Summary

A comparative study of QoT estimations for WDM systems using ANN-based ML models and GN-based analytical models is conducted through simulations and experiments. In simulation settings, where all the parameters are known, analytical models generally outperform ANN models while for experimental settings, inaccurate knowledge of various link parameters degrades analytical models and ML generally estimates the QoT with better accuracy. However, ML models are temporally less stable and less generalizable to different link configurations and additional re-training

and adaption are required to ensure their performance in heterogeneous and dynamic network settings. However, since transfer learning is still a very new area of interest in ML applications in optical networks, it is expected that there are a lot of opportunities to further improve transfer learning performance so that ML will be a good solution for QoT estimation in heterogeneous network configurations. The overall network capacity gains enabled by more accurate QoT estimators and reduced operating margins are also studied.

Chapter 5
Conclusions and Future Perspectives

In this Chapter, conclusions have been drawn from the research work carried out in this thesis and future directions of related research work are discussed.

5.1 Conclusions

In this thesis, advanced OPM and QoT estimation techniques for next-generation optical transmission systems and networks are studied. Firstly, S-FFT-assisted high-accuracy and low-complexity multi-parameter monitoring techniques are proposed to monitor modulation format, TO, FO, and FOD. Then, a joint linear and nonlinear noise monitoring scheme based on spectrum analysis is proposed to monitor SNR_{linear} and $SNR_{nonlinear}$ simultaneously. Finally, practical implementation of analytical model-based and ML model-based QoT estimators is discussed and a comprehensive comparison between them is provided.

5.1.1 High-Accuracy and Low-Complexity Multi-Parameter Monitoring Techniques for Flexible Optical Networks

Assisted by sparse fast Fourier transform (S-FFT), high-accuracy and low-complexity multi-parameter monitoring techniques for flexible optical networks are proposed to monitor modulation format, TO, FO and FOD. The monitoring principles of each parameter are explained in detail. Through simulation, the optimization processes of

these monitoring schemes are shown and discussed. Experimental study is further conducted to verify the performance of the proposed scheme. The results show high monitoring performance and low complexity, making the proposed techniques very attractive to be employed in next-generation optical communication systems and networks.

5.1.2 Joint Linear and Nonlinear Noise Monitoring Techniques Based on Spectrum Analysis

A modulation-format-transparent, accurate joint linear and nonlinear noise monitoring scheme based on the calculation of correlation between two spectral components at the upper and lower sideband of the signal spectrum is proposed. Different characteristics of flat linear noise spectrum and non-flat nonlinear noise spectrum are used to distinguish the influences on the correlation value from both noise sources. Simulation results show that the proposed scheme can accurately monitor SNR_{linear} and $SNR_{nonlinear}$ within a wide launch power range from -5 dBm to 5 dBm per channel for multi-channel WDM systems with a 915-km SSMF link. The performance of the proposed scheme is further experimentally verified in up-to-7 channel WDM systems over a 915 km SMF link.

5.1.3 QoT Estimation Based on Machine Learning and Analytical Models and Their Performance Comparisons

A comprehensive comparative study of QoT estimation for WDM systems using ANN-based ML models and GN model-based analytical models is discussed. In simulation settings with perfect knowledge of system parameters and communication channels, GN-based analytical models generally outperform ANN models while in experimental

settings, however, inaccurate knowledge of various link parameters degrades GN-based models and ML generally estimates the QoT with better accuracies. However, ML models are temporally less stable and less generalizable to different link configurations. Considerable network capacity gains can be achieved by accurate QoT estimators with reduced operating margins.

5.2 Future Perspectives

For multi-parameter monitoring techniques, although fast monitoring of optical parameters can be realized by the proposed schemes, it is still not clear how often parameter monitoring should be operated. Constant monitoring leads to high complexity, while sparse monitoring may result in performance degradation. Such a trade-off needs to be discussed further.

For linear and nonlinear noise monitoring, although the proposed scheme shows high accuracy and large monitoring range, the parameter fitting process can not be avoided, which limits the practical application of it. A more direct scheme which can monitor the NLI without any fitting is desirable and will be an interesting topic for further research.

For QoT estimation, although both the analytical model and the ML model show their potentials, the practical operations of them need to be further discussed to improve accuracy and reduce the difficulty of implementation. For example, in brown-field implementation, current transmission data can be used to optimize the model for the QoT estimation after capacity upgradation. Therefore, it is possible to realize accurate QoT estimation in a more efficient way.

Appendix

In appendix, we provide detailed derivation of the property of the Sparse-FFT used in our research. The principle of discrete Fourier transform can be written as

$$X(k) = \sum_{n=0}^{N-1} x(n) e^{-j\frac{2\pi}{N}kn}, \qquad k = 0,1,2...,N-1 \tag{1}$$

where $X(k)$ is the frequency domain spectrum of the time domain signal $x(n)$. It is observed that, the zero-frequency component $X(0)$ is the numerical sum of all symbols in the signal with *k* of 0. Assuming *N* is even, After FFT-shift operation which aims to move the zero-frequency component to the central location of the spectrum to facilitate observation, the index of $X(0)$ is *N*/2+1. For the signal length of 2^n, the index of the zero-frequency component is $2^{n-1}+1$. The principle of our used sparse-FFT is based on time domain aliasing. As analyzed above, the value of the zero-frequency component is always the sum of all symbols in the signal. Therefore, the aliasing process will not influence the zero-frequency component value of the spectrum of an aliased signal using FFT.

Based on the above analysis, it can be concluded that for the signal length of 2^n, the frequency component whose index is $2^{n-1}+1$ will never lose no matter how many times aliasing and subsampling are performed. Such property is adopted to assist our proposed multi-parameter monitoring scheme.

Bibliography

1. G. Forecast, ‘‘Cisco visual networking index: Global mobile data traffic forecast update, 2017–2022,’’ Update, vol. 2017, p. 2022, Feb. 2019.
2. K. Roberts, Q. Zhuge, I. Monga, S. Gareau, and C. Laperle, “Beyond 100 Gb/s: Capacity, flexibility, and network optimization,” J. Opt. Commun. Netw. **9**(4), C12–C24 (2017).
3. E. Ip, A. P. T. Lau, J. M. Kahn. Coherent detection in optical fiber systems. J. Lightwave Technol. 16(2), 753-791 (2008).
4. S. J. Savory, “Digital filters for coherent optical receivers,” Opt. Express **16**(2), 804–817 (2008).
5. Z. Dong, F. N. Khan, Q. Sui, K. Zhong, C. Lu, and A. P. T. Lau, “Optical performance monitoring: A preview of current and future technologies,” J. Lightwave Technol. 34(2), 525–543 (2016).
6. T. Xia, S. Gringeri, M. Tomizawa. “High-capacity optical transport networks,” IEEE Communications Magazine, **50**(11), 170-178 (2012).
7. P. J. Winzer, “High-spectral-efficiency optical modulation formats,” J. Lightwave Technol. **30**(8), 3824–3835 (2012).
8. H. Khodakarami, B. Pillai, B. Sedighi, and W. Shieh, “Flexible optical networks: an energy efficiency perspective,” J. Lightwave Technol. **32**(21), 3958 (2014).
9. R. M. Morais and J. Pedro, “Machine learning models for estimating quality of transmission in DWDM networks,” J. Opt. Commun. Netw. **10**, D84–D99 (2018).
10. K. Nagayam, M. Kakui, M. Matsui, I. Saitoh, and Y. Chigusa, “Ultra-Low-Loss (0.1484 dB/km) Pure Silica Core Fibre and Extension of Transmission Distance,” Electron. Lett. **38**(20), 1168–1169 (2002).
11. E. Torrengo, R. Cigliutti, G. Bosco, A. Carena, V. Curri, P. Poggiolini, A. Nespola, D. Zeolla, and F. Forghieri, “Experimental validation of an analytical

model for nonlinear propagation in uncompensated optical links," Opt. Express **19**(26), B790–B798 (2011).

12. R. Soriano, F. Hauske, N. Gonzalez, et al. "Chromatic dispersion estimation in digital coherent receivers, " Journal of Lightwave Technology, **29**(11), 1627-1637 (2011).
13. G. P. Agrawal, "Nonlinear fiber optics," in Nonlinear Science at the Dawn of the 21st Century. Springer: Berlin, Germany, 2000.
14. J. Lu, X. Li, S. Fu, M. Luo, M. Xiang, H. Zhou, M. Tang, and D. Liu, "Joint carrier phase and frequency-offset estimation with parallel implementation for dual-polarization coherent receiver," Opt. Express **25**(5), 5217–5231 (2017).
15. I. Fatadin, S. J. Savory, and D. Ives, "Compensation of quadrature imbalance in an optical QPSK coherent receiver," IEEE Photonics Technol. Lett. **20**(20), 1733–1735 (2008).
16. M. Oerder and H. Mery, "Digital Filter and Square Timing Recovery," IEEE Trans. Commun. **34**(10), 605–612 (1988).
17. T. M. Schmidl and D. C. Cox, "Robust frequency and timing synchronization for OFDM," IEEE Trans. Commun. **45**(12), 1613–1621 (1997).
18. M. Selmi, Y. Jaouën, P. Ciblat, and B. Lankl, "Accurate digital frequency offset estimator for coherent PolMux QAM transmission systems," in Proc. ECOC'09 (2009), paper P3.08.
19. A. J. Viterbi and A. M. Viterbi, "Nonlinear estimation of PSK-modulated carrier phase with application to burst digital transmission," IEEE Trans. Inf. Theory **29**(4), 543–551 (1983).
20. T. Pfau, S. Hoffmann, and R. Noé, "Hardware-efficient coherent digital receiver concept with feedforward carrier recovery for M-QAM constellations," J. Lightwave Technol. **27**(8), 989–999 (2009).
21. K. Roberts and C. Laperle, "Flexible transceivers," in European Conference on Optical Communication 2014 (ECOC), paper We.3.A.3.
22. D. C. Kilper, S. Chandrasekhar, L. Buhl, A. Agarwal, and D. Maywar, "Spectral monitoring of OSNR in high speed networks," in European

Conference and Exhibition on Optical Communication (ECOC), 2002, paper 7.4.4.

23. C. Pulikkaseril, L. A. Stewart, M. A. Roelens, G. W. Baxter, S. Poole, and S. Frisken, "Spectral modeling of channel band shapes in wavelength selective switches," Opt. Express **19**(9), 8458–8470 (2011).
24. J. H. Lee, D. K. Jung, C. H. Kim, and Y. C. Chung, "OSNR monitoring technique using polarization nulling method," IEEE Photonics Technol. Lett. **13**(1), 88–90 (2001).
25. R. Schmogrow, B. Nebendahl, M.Winter, A. Josten, D. Hillerkuss, S. Koenig, J. Meyer, M. Dreschmann, M. Huebner, C. Koos, J. Becker, W. Freude, and J. Leuthold, "Error vector magnitude as a performance measure for advanced modulation formats," IEEE Photonics Technol. Lett. **24**(1), 61–63 (2012).
26. C. Zhu, A. Tran, S. Chen, L. Du, C. Do, T. Anderson, A. J. Lowery, and E. Skafidas, "Statistical moments-based OSNR monitoring for coherent optical systems," Opt. Express **20**(16), 17711–17721 (2012).
27. M. Ionescu, M. Sato, and B. Thomsen, "Cyclostationarity-based joint monitoring of symbol-rate, frequency offset, CD and OSNR for Nyquist WDM superchannels," Opt. Express **23**(20), 25762–25772 (2015).
28. P. Poggiolini, G. Bosco, A. Carena, V. Curri, Y. Jiang, and F. Forghieri, "The GN-model of fiber non-linear propagation and its applications," J. Lightwave Technol. **32**(4), 694–721 (2014).
29. Z. Dong, A. P. T. Lau, and C. Lu, "OSNR monitoring for QPSK and 16-QAM systems in presence of fiber nonlinearities for digital coherent receivers," Opt. Express **20**(17), 19520–19534 (2012).
30. H. G. Choi, J. H. Chang, Hoon Kim, and Y. C. Chung, "Nonlinearity-Tolerant OSNR Estimation Technique for Coherent Optical Systems," in Optical Fiber Communication Conference (Optical Society of America, 2015), paper W4D.2.
31. Y. Pointurier, "Design of low-margin optical networks," J. Opt. Commun. Netw. **9**, A9–A17 (2017).

32. J. Shao, X. Liang, and S. Kumar, "Comparison of split-step Fourier schemes for simulating fiber optic communication systems," IEEE Photon. J. **6**, 7200515 (2014).
33. A. Carena, G. Bosco, V. Curri, Y. Jiang, P. Poggiolini, and F. Forghieri, "EGN model of non-linear fiber propagation," Opt. Express **22**, 16335–16362 (2014).
34. C. Rottondi, L. Barletta, A. Giusti, and M. Tornatore, "Machine learning method for quality of transmission prediction of unestablished lightpaths," J. Opt. Commun. Netw. 10, A286–A297 (2018).
35. I. Sartzetakis, K. Christodoulopoulos, and E. Varvarigos, "Formulating QoT estimation with machine learning," European Conference on Optical Communication (ECOC), Rome, Italy (2018), paper We1D.3.
36. D. Semrau, R. I. Killey, and P. Bayvel, "A closed-form approximation of the Gaussian noise model in the presence of inter-channel stimulated Raman scattering," J. Lightwave Technol. 37, 1924–1936 (2019).
37. L. Dou, T Yamauchi, X. Su, Z. Tao, S. Oda, Y. Aoki, T. Hoshida, and J. Rasmussen, "An accurate nonlinear noise insensitive OSNR monitor," in The Optical Fiber Communication Conference and Exhibition 2016 (OFC), paper W3A.5. pp. 1–3.
38. W. Wang, A. Yang, P. Guo, Y. Lu, and Y. Qiao, "Joint OSNR and Interchannel Nonlinearity Estimation Method Based on Fractional Fourier Transform," J. Lightwave Technol. **35**(20), 4497–4506 (2017).
39. A. P. T. Lau, T. S. Shen, W. Shieh, and K. Ho, "Equalization-enhanced phase noise for 100Gb/s transmission and beyond with coherent detection," Opt. Express **18**(16), 17239–17251 (2010).
40. R. Borkowski, D. Zibar, A. Caballero, V. Arlunno, and I. T. Monroy, "Stokes space-based optical modulation format recognition for digital coherent receivers," IEEE Photonics Technol. Lett. 25(21), 2129–2132 (2013).
41. J. Lu, Q. Wu, H. Jiang, S. Fu, M. Tang, and C. Lu, "Efficient Timing/Frequency Synchronization Based on Sparse Fast Fourier Transform (S-FFT)," J. Lightw. Technol., **37**(20), 5299-5308 (2019).

42. A. Nag, M. Tornatore, and B. Mukherjee, “Optical network design with mixed line rates and multiple modulation formats,” J. Lightwave Technol. **28**(4), 466–475 (2010).
43. V. N. Rozental and D. A. Mello, “Hitless rate switching for dynamically reconfigurable optical systems,” IEEE Photonics J. **7**(2), 1–9 (2015).
44. R. Boada, R. Borkowski, and I. T. Monroy, “Clustering algorithms for Stokes space modulation format recognition,” Opt. Express **23**(12), 15521–15531 (2015).
45. T. Bo, J. Tang, and C. C. K. Chan, “Modulation format recognition for optical signals using connected component analysis,” IEEE Photonics Technol. Lett. **29**(1), 11–14 (2017).
46. J. Liu, K. Zhong, Z. Dong, C. Guo, A. P. T. Lau, C. Lu, and Y. Lu, “Signal power distribution based modulation format identification for coherent optical receivers,” Opt. Fiber Technol. **36**, 75–81 (2017).
47. M. Xiang, Q. Zhuge, M. Qiu, X. Zhou, F. Zhang, M. Tang, D. Liu, S. Fu, and D. V. Plant, “Modulation format identification aided hitless flexible coherent transceiver,” Opt. Express **24**(14), 15642–15655 (2016).
48. M. Xiang, Q. Zhuge, M. Qiu, X. Zhou, M. Tang, D. Liu, S. Fu, and D. V. Plant, “RF-pilot aided modulation format identification for hitless coherent transceiver,” Opt. Express **25**(1), 463–471 (2017).
49. H. Minn, M. Zeng, and V. K. Bhargava, “On timing offset estimation for OFDM systems,” IEEE Commun. Lett., **4**(7), 242–244 (2000).
50. B. Park, H. Cheon, C. Kang, and D. Hong, “A novel timing estimation method for OFDM systems,” IEEE Commun. Lett., **7**(5), 239–241 (2003).
51. Y. Huang, X. Zhang, and L. Xi, “Modified synchronization scheme for coherent optical OFDM systems,” J. Opt. Commun. Netw., **5**(6), 584–592 (2013).
52. X. Du, J. Zhang, Y. Li, C. Yu, and P.-Y. Kam, “Efficient joint timing and frequency synchronization algorithm for coherent optical OFDM systems,” Opt. Express, **24**(17), 19969–19977 (2016).

53. Q. Zhuge, M.Morsy-Osman, X. Xu, M. Chagnon, M. Qiu, and D. V. Plant, "Spectral efficiency-adaptive optical transmission using time domain hybrid QAM for agile optical networks," J. Lightw. Technol., **31**(15), 2621–2628 (2013).
54. F. Xiao et al., "Feed-forward frequency offset estimation for 32-QAM optical coherent detection," Opt. Express, **25**(8), 8828–8839 (2017).
55. F. Buchali,W. Idler, L. Schmalen, G. Bocherer, P. Schulte, and F. Steiner, "Probabilistically shaped QAM for independent reach, spectral efficiency and Bit-rate adaptation," in Proc. Eur. Conf. Opt. Commun., Dusseldorf, Germany, 2016, pp. 1–3..
56. M. Qiu, Q. Zhuge, X. Xu, M. Chagnon, M. Morsy-Osman, and D. V. Plant, "Simple and efficient frequency offset tracking and carrier phase recovery algorithms in single carrier transmission systems," Opt. Express, **21**(7), 8157–8165 (2013).
57. J. Lu and C. Lu, "Frequency offset drift monitoring: enabling simultaneously optimum performance and minimum cost of frequency offset estimation," Opt. Lett. **44**, 3753–3756 (2019).
58. J. Ke, K. P. Zhong, Y. Gao, A. Bakshali, and J. C. Cartledge, in Optical Fiber Communication Conference and Exposition and the National Fiber Optic Engineers Conference (OFC/NFOEC) (2013), paper OTu3I.5.
59. Q. Zhuge, X. Zeng, H. Lun, M. Cai, X. Liu, L. Yi, and W. Hu, "Application of machine learning in fiber nonlinearity modeling and monitoring for elastic optical networks," J. Lightwave Technol. **37**, 3055–3063 (2019).
60. J. Pesic, M. Lonardi, N. Rossi, T. Zami, E. Seve, and Y. Pointurier, "How uncertainty on the fiber span lengths influences QoT estimation using machine learning in WDM networks," in Optical Fiber Communication Conference (OFC), OSA Technical Digest (Optical Society of America, 2020), paper Th3D.5.
61. Q. Fan, J. Lu, G. Zhou, D. Zeng, C. Guo, L. Lu, J. Li, C. Xie, C. Lu, F. N. Khan, and A. P. T. Lau, "Experimental comparisons between machine learning and analytical models for QoT estimations in WDM systems," in Optical Fiber

Communication Conference (OFC), OSA Technical Digest (2020), paper M2J.2.

62. H. Hassanieh, P. Indyk, D. Katabi, and E. Price, “Simple and Practical Algorithm for Sparse Fourier Transform,” ACM-SIAM Symposium on Discrete Algorithms (2012), p. 1183.
63. H. Hassanieh, F. Adib, D. Katabi, and P. Indyk, “Faster GPS via the Sparse Fourier Transform,” in Proceedings of the 18th Annual International Conference on Mobile Networking and Computing (2012), 6, p. 353.
64. J. Lu, Y. Tian, S. Fu, X. Li, M. Luo, M. Tang, and D. Liu, “Frequency offset estimation for 32-QAM based on constellation rotation,” IEEE Photonics Technol. Lett. **29**(23), 2115–2118 (2017).
65. Optical Internetworking Forum, “Integrable tunable transmitter assembly multi source agreement,” OIF-ITTA-MSA-01.0 (2008).
66. H. Zhou et al., “Joint timing/frequency offset estimation and correction based on FRFT encoded training symbols for PDM co-OFDM systems,” Opt. Express, **24**(25), 28256–28269 (2016).
67. I. Fatadin, D. Ives, and S. J. Savory, “Laser linewidth tolerance for 16-QAM coherent optical systems using QPSK partitioning,” IEEE Photonics Technol. Lett. 22(9), 631–633 (2010).
68. J. Lu, Z. Tan, A. P. T. Lau, S. Fu, M. Tang, and C. Lu, “Modulation format identification assisted by sparse-fastFourier-transform for hitless flexible coherent transceivers,” Opt. Express **27**(5), 7072–7086 (2019).
69. I. Tomkos, S. Azodolmolky, J. Sole-Pareta, D. Careglio, and E. Palkopoulou, “A tutorial on the flexible optical networking paradigm: state of the art, trends, and research challenges,” Proc. IEEE **102**(9), 1317–1337 (2014).
70. J. Lu, G. Zhou, Q. Fan, D. Zeng, C. Guo, L. Lu, J. Li, C. Xie, C. Lu, F. Khan, and A. Lau, "Performance comparisons between machine learning and analytical models for quality of transmission estimation in wavelength-division-multiplexed systems [Invited]," J. Opt. Commun. Netw. **13**, B35-B44 (2021).

71. F. N. Hauske, M. Kuschnerov, B. Spinnler, and B. Lankl, “Optical performance monitoring in digital coherent receivers,” J. Lightwave Technol. **27**(16), 3623–3631 (2009).
72. T. Saida, I. Ogawa, T. Mizuno, K. Sano, H. Fukuyama, Y. Muramoto, Y. Hashizume, H. Nosaka, S. Yamamoto, and K. Murata, “In-band OSNR monitor with high-speed integrated Stokes polarimeter for polarization division multiplexed signal,” Opt. Express **20**(26), B165–B170 (2012).
73. Q. Wu, L. Zhang, X. Li, M. Luo, Z. Feng, H. Zhou, M. Tang, S. Fu, and D. Liu, “Training Symbol Assisted in-Band OSNR Monitoring Technique for PDM-CO-OFDM System,” J. Lightwave Technol. **35**(9), 1551–1556 (2017).
74. A. Carena, G. Bosco, V. Curri, P. Poggiolini, M. Taiba, and F. Forghieri, “Statistical characterization of PM QPSK signals after propagation in uncompensated fiber links,” in European Conference and Exhibition on Optical Communication (ECOC), 2010, paper 4.07.
75. J. Lu, S. Fu, L. Deng, M. Tang, Z. Hu, D. Liu, and C. C. K. Chan, “Blind and Fast Modulation Format Identification by Frequency-offset Loading for Hitless Flexible Transceiver,” in The Optical Fiber Communication Conference and Exhibition 2018 (OFC), paper M2F.5. pp. 1–3.
76. F. L. Heismann, “Determining in-band optical signal-to-noise ratio in polarization-multiplexed optical signals using signal correlations”, U.S. Patent US 2018/0138974 Al, 2018.
77. M. Ionescu, “Digital Signal Processing for Sensing in Software Defined Optical Networks”, PhD’s thesis, the University College London, 2015.
78. W. A. Gardner, A. Napolitano, and L. Paura, “Cyclostationarity: Half a century of research,” Signal Process. **86**(4), 639–697 (2006).
79. E. Ip, “Nonlinear compensation using backpropagation for polarization-multiplexed transmission,” J. Lightwave Technol. **28**(6), 939–951 (2010).
80. A. Blumer, A. Ehrenfeucht, D. Haussler, and M. K. Warmuth, “Occam’s razor,” Inf. Process. Lett **24**(6), 377–380 (1987).
81. P. Domingos, “The role of Occam’s razor in knowledge discovery,” Data Min. Knowl. Discov. **3**(4), 409–425 (1999).

82. IEC TR 61282-12:2016, “Fibre optic communication system design guides - Part 12: In-band optical signal-to-noise ratio (OSNR),” 2016.
83. X. Zhou, Q. Zhuge, M. Qiu, M. Xiang, F. Zhang, B. Wu, K. Qiu, and D. V. Plant, “On the capacity improvement achieved by bandwidth-variable transceivers in meshed optical networks with cascaded ROADMs,” Opt. Express **25**(5), 4773–4782 (2017).
84. C. Pulikkaseril, L. A. Stewart, M. A. Roelens, G. W. Baxter, S. Poole, and S. Frisken, “Spectral modeling of channel band shapes in wavelength selective switches,” Opt. Express **19**(9), 8458–8470 (2011).
85. W. Shieh, R. S. Tucker, W. Chen, X. Yi, and G. Pendock, “Optical performance monitoring in coherent optical OFDM systems,” Opt. Express 15(2), 350–356 (2007).
86. A. Ferrari, M. Filer, K. Balasubramanian, Y. Yin, E. Le Rouzic, J. Kundrát, G. Grammel, G. Galimberti, and V. Curri, “GNPy: an open source application for physical layer aware open optical networks,” J. Opt. Commun. Netw. **12**, C31–C40 (2020).
87. F. N. Khan, Q. Fan, C. Lu, and A. P. T. Lau, “Machine learning methods for optical communication systems and networks,” in Optical Fiber Telecommunications VII, A. E. Willner, ed. (Academic, 2020), Chap. 21, pp. 921–978.
88. J. Yu, W. Mo, Y.-K. Huang, E. Ip, and D. C. Kilper, “Model transfer of QoT prediction in optical networks based on artificial neural networks,” J. Opt. Commun. Netw. **11**, C48–C57 (2019).
89. F. N. Khan, Q. Fan, C. Lu, and A. P. T. Lau, “An optical communication's perspective on machine learning and its applications,” J. Lightwave Technol. **37**, 493-516 (2019).
90. C. M. Bishop, Pattern Recognition and Machine Learning (Springer-Verlag, 2006).
91. E. Seve, J. Pesic, C. Delezoide, and Y. Pointurier, “Learning process for reducing uncertainties on network parameters and design margins,” in Optical

Fiber Communication Conference, OSA Technical Digest (online) (Optical Society of America, 2017), paper W4F.6.

92. F. N. Khan, C. H. Teow, S. G. Kiu, M. C. Tan, Y. Zhou, W. H. Al-Arashi, A. P. T. Lau, and C. Lu, “Automatic modulation format/bitrate classification and signal-to-noise ratio estimation using asynchronous delay-tap sampling,” Comput. Electron. Eng. **47**, 126–133 (2015).
93. F. N. Khan and M. C. Tan, “Duty-cycle detection for noisy arbitrary waveforms using artificial neural networks,” IET Electron. Lett. **53**, 68–70 (2017).
94. L. Yu, X. Wei, J. Xu, J. Xu, W. K. Hau, K. K. Tsia, and K. K. Y. Wong, "Amplified optical time-stretch optical coherence tomography for endoscopic imaging," in *Optics in the Life Sciences* (OSA, 2015), p. BM4A.5.
95. S. Marsland, Machine Learning: An Algorithmic Perspective, 2nd ed. (CRC Press, 2015).
96. S. Yan, F. N. Khan, A. Mavromatis, D. Gkounis, Q. Fan, F. Ntavou, and D. Simeonidou, “Field trial of machine learning-assisted and SDN-based optical network planning with network-scale monitoring database,” in European Conference on Optical Communication (ECOC), Gothenburg, Sweden, 2017, paper Th.PDP.B.4.
97. S. J. Savory, R. J. Vincent, and D. J. Ives, “Design considerations for low-margin elastic optical networks in the nonlinear regim [Invited],” J. Opt. Commun. Netw. **11**, C76–C85 (2020).
98. J. Cho and P. J. Winzer, “Probabilistic constellation shaping for optical fiber communications,” J. Lightwave Technol. **37**, 1590–1607 (2019).